KOBELCO TECHNOLOGY REVIEW

No. 37 Apr. 2019

Feature- Ⅰ : Excavators & Cranes
Feature- Ⅱ : Utilization of ICT

Contents

Feature- Ⅰ Excavators & Cranes

Feature- Ⅱ Utilization of ICT

Published by

Technical Development Group
Kobe Steel, Ltd.

5-5, Takatsukadai 1-chome,
Nishi-ku, Kobe, HYOGO 651-2271, JAPAN
http://www.kobelco.co.jp

Editorial Office: **Shinko Research Co., Ltd.**
2-4, Wakinohama-Kaigandori 2-chome,
Chuo-ku, Kobe, HYOGO 651-8585,
JAPAN
Fax: +81-78-261-7843
E-mail: rd-office@kobelco.com

Electric Motor HILS System Using Numerical Stabilization Technique for Simulating Nonlinear Coupled System

Kei MORITA*1

*1 Production Systems Research Laboratory, Technical Development Group

This paper introduces a stabilization technique of nonlinear coupled analysis for hydraulic excavators, in which a rigid body system and a hydraulic system are coupled. Also introduced is a "Hardware-In-the-Loop Simulation (HILS)" for electric motors, in which the above technique is exploited. The rigid body system consists of a rotating element and a linear motion element, and the stabilization technique converts the motion of the rotating element into linear motion, enabling the motion of both the systems to be described in an ordinary differential equation without introducing any constraint conditions for the rigid bodies. This enables a coupled analysis with one motion equation that shares the state quantities of both the systems, thus improving the stability of the numerical analysis. This technique has been used to simulate in real-time the actual load acting on the electric motor, which has been reproduced on a motor-load testing apparatus and has realized an electric motor HILS system.

Introduction

The requirements on greenhouse gas emission reduction have become more stringent to suppress global warming, and improvement in fuel economy is now an important issue also for hydraulic excavators. In an effort to improve the fuel economy, hybrid systems have been in development to drive upper slewing bodies by electric motors so as to utilize the energy of their deceleration effectively.[1), 2)] The development of hybrid systems requires fully understanding the characteristics of their electric motors and then optimizing their control systems. Hardware In the Loop Simulation (HILS)[note 1)] offers an effective means for improving development efficiency. A hydraulic excavator, however, calls for non-linear analysis, in which a "hydraulic system," showing strong non-linearity, and a "rigid body system," including link mechanisms such as booms, are coupled. This presents a challenge in ensuring the stability of the numerical analysis.

note 1) A technology for evaluating the performance and quality of hardware to be developed by connecting and running the hardware to be developed by simulating in real-time the entire system other than said hardware.

Meanwhile, HILS is used for the development of engines, transmissions, electronic control units (ECUs), etc., in the field of automobiles[3)] and for virtual testing on running stability, among other things, in the field of railroad equipment,[4)] thus contributing greatly to the improvement of development efficiency, performance, and quality. So far, however, almost no HILS system has been reported as established, in which real-time calculation is carried out using an analysis model in which a rigid body system and hydraulic system are coupled together, as in the case of hydraulic excavators.

This paper describes a technology for improving the numerical stability of "SINDYS," a simulation program for non-linear systems, including a hydraulic system coupled with a linkage mechanism on the basis of a modeling technique for converting the movement of a rigid body system from rotating element motion to linear element motion.[5)] As also introduced in this paper, this stabilization technology has been adapted for an HILS system for electric motors,[6)] in which the system calculates the load acting on an electric motor in real time during work and reproduces it on an apparatus for testing the load acting on the electric motor. The target is a hybrid system with an upper slewing body rotationally driven by an electric motor.

1. Coupled analysis theory for rigid body-hydraulic system

1.1 Analysis model for hydraulic excavators

Fig. 1 depicts the linkage model of a hydraulic excavator. The attachments on this hydraulic excavator consist of a boom, arm, and bucket, which are coupled with the upper slewing body. Each linkage of the boom, arm, and bucket is independently driven by the corresponding, elongating/contracting hydraulic cylinder. The upper slewing body is driven by an electric motor via a slewing bearing and reduction gears and makes a slewing movement involving the attachments. The above configuration is modeled using the formulation of a rigid body system which will be described later.

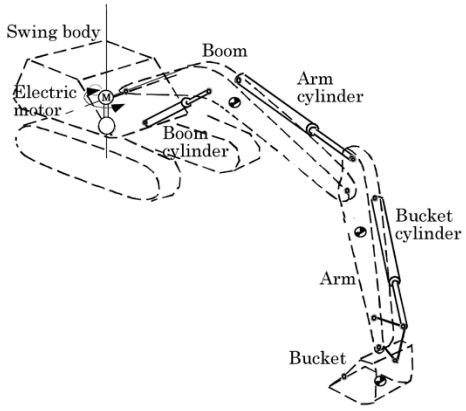

Fig. 1 Linkage model of hydraulic excavator

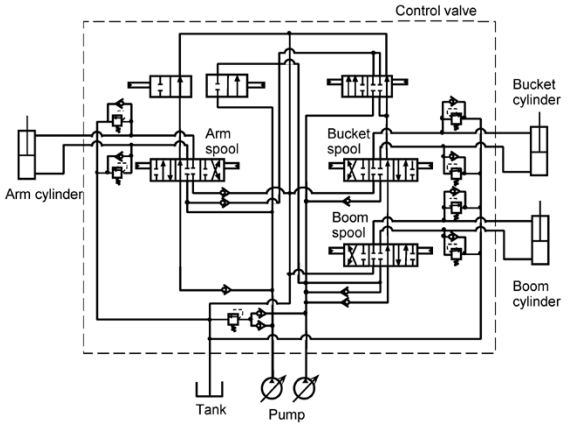

Fig. 2 Hydraulic system of hydraulic excavator

Fig. 2 shows the hydraulic system for driving the attachments. This system comprises two hydraulic pumps driven by the engine to supply hydraulic pressure, in which control valves are operated in accordance with the levers manipulated by an operator. This system thus changes the opening area to each branch piping and controls the flow rate of hydraulic oil supplied from the pump to the hydraulic cylinder.

1.2 Motion equation of coupled system[5)]

The coupled analysis of a rigid body system and hydraulic system involves the analysis of a non-linear motion equation (Equation (1)) consisting of the superimposition of MCK type motion equations in each system:

$$\mathbf{M}\ddot{\mathbf{q}}_{n+1} + \mathbf{C}\dot{\mathbf{q}}_{n+1} + \mathbf{K}\mathbf{q}_{n+1} = \mathbf{f}_{n+1} - \bar{\mathbf{f}}_n \cdots\cdots (1)$$

wherein $\mathbf{q}_{n+1}$ is a vector representing the state quantities such as the displacement and rotation angle at time t_{n+1} in a rigid body system, and such as the flow rate product (integral of volumetric flow rate) in a hydraulic system. **M**, **C**, and **K** represent the mass, attenuation, and stiffness matrices linearized at time t_n, respectively, and $\mathbf{f}_{n+1}$ is the external force at time t_{n+1}. The term $\bar{\mathbf{f}}_n$ is the external force corrected by linearizing the non-linear elemental force at each time step. As shown in **Fig. 3**, the stiffness element can be expressed as $\mathbf{K}\mathbf{q}_{n+1} = \mathbf{f}_{n+1} - \bar{\mathbf{f}}_n$ by introducing the corrected external force. Here, $\bar{\mathbf{f}}_n = \mathbf{f}_n - \mathbf{K}\mathbf{q}_n$. The same applies to the mass and attenuation elements. The time integration employs the Newmark β method ($\beta = 1/4$).

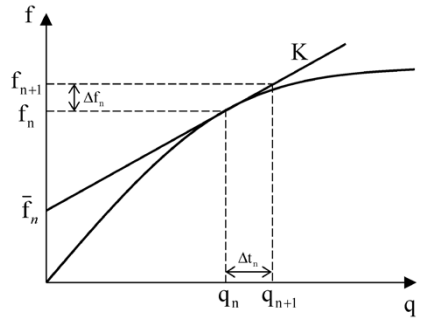

Fig. 3 Corrected external force by linearization

1.3 Formulation of rigid body system[5)]

As the model of the slewing body of a hydraulic excavator, a rigid body linkage model as shown in **Fig. 4** is considered. This model consists of four rigid bodies. Body 0 only rotates around the y-axis

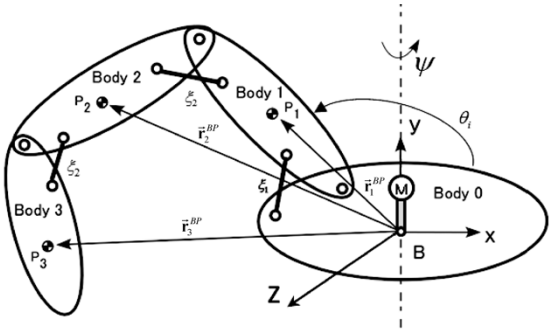

Fig. 4 Rigid body linkage model

(rotational angle, ψ) without moving translationally. Body 1 is constrained to body 0 by a pin joint, is driven translationally by the linear motion element between body 0 and body 1 (cylinder displacement, ξ_1), and rotates around the z-axis (rotational angle, θ_1). The same applies to body 2 and body 3. Bodies 1 to 3 move (rotation angle, ψ) together as a result of body 0 rotating around the y-axis. In this way, in the rigid body system, each rigid body's motion at the position of its center of gravity (P_i (i = 1 to 3)) can be expressed by the rotating motion and translational drive by linear motion elements.

On the other hand, in the hydraulic system described in Subsection 1.4, the motions of its linear elements such as a hydraulic cylinder are expressed by their translational displacements to express their motions in one dimensional state quantities.

Therefore, in the case of the coupled analysis of a rigid body system and hydraulic system, expressing the rotational motion of the rigid body system in terms of the motion of the linear motion element allows the motion of both the systems to be expressed by an ordinary differential equation without introducing any constraint conditions. This eliminates the need for modeling with separate pieces of software and calculating, while changing the state quantities for each time step, when the coupled analysis of each system is carried out. As a result, it has become possible to carry out a coupled analysis with only one piece of software, which improves stability in the numerical analyses.

Now, in order to convert the motion of a rigid body system as shown in Fig. 4 from the motion of the rotating element to the motion of the linear motion element, the position of the center of gravity of each body is described by the rotational angle around z-axis and, in addition, the rotation angle around the z-axis is described by the cylinder's displacement so as to express the motion of the linear motion element.

First, the motion equation for the point Pi and slewing axis is that for the rigid body system and is given by Equation (2):

$$\mathbf{M}_e\ddot{\mathbf{w}} = \mathbf{f}_e \quad \cdots\cdots (2)$$

wherein $\mathbf{M}_e$ is an inertia matrix consisting of the mass of point P_i and inertia moment around the y-axis of the body 0, and $\mathbf{f}_e$ is an external force vector. The term $\ddot{\mathbf{w}}$ represents an acceleration matrix, $\ddot{\mathbf{w}} = [\ddot{\mathbf{r}}_1^T\ \ddot{\mathbf{r}}_2^T\ \ddot{\mathbf{r}}_3^T\ \ddot{\psi}]^T$, $\ddot{\mathbf{r}}_i = [\ddot{x}_i\ \ddot{y}_i\ \ddot{z}_i]$, in which $\ddot{\mathbf{r}}_i$ is the acceleration of the point P_i seen from point B, and $\ddot{\psi}$ is the angular acceleration of slewing.

Next, assuming that the angle of bodies 1 to 3 around the z-axis of point B is θ_i, the acceleration matrix $\ddot{\mathbf{w}}$ is given by Equation (3) using the coordinates transformation matrices $\mathbf{G}_{11}$ and $\mathbf{G}_{12}$.

$$\ddot{\mathbf{w}} = \mathbf{G}_{11}\ddot{\mathbf{q}}_\theta + \mathbf{G}_{12}\dot{\mathbf{q}}_\theta \quad \cdots\cdots (3)$$

wherein $\ddot{\mathbf{q}}_\theta = [\ddot{\theta}_1\ \ddot{\theta}_2\ \ddot{\theta}_3\ \ddot{\psi}]^T$, $\dot{\mathbf{q}}_\theta = [\dot{\theta}_1\ \dot{\theta}_2\ \dot{\theta}_3\ \dot{\psi}]^T$.

In addition, using each cylinder displacement ξ_i instead of angle θ_i gives the relation of Equation (4).

$$\dot{\mathbf{q}}_\theta = \mathbf{G}_{23}\dot{\mathbf{q}}_\xi \quad \cdots\cdots (4)$$

wherein $\dot{\mathbf{q}}_\xi = [\dot{\xi}_1\ \dot{\xi}_2\ \dot{\xi}_3\ \dot{\psi}]^T$. Moreover, differentiating Equation (4) gives the relationship between $\ddot{\mathbf{q}}_\theta$ and $\dot{\mathbf{q}}_\xi$.

$$\ddot{\mathbf{q}}_\theta = \mathbf{G}_{23}\ddot{\mathbf{q}}_\xi + \mathbf{G}_{23}\dot{\mathbf{q}}_\xi \quad \cdots\cdots (5)$$

From the above, Equation (6) is obtained by substituting Equations (3), (4), and (5) for Equation (2).

$$\mathbf{M}_\xi\ddot{\mathbf{q}}_\xi + \mathbf{C}_\xi\dot{\mathbf{q}}_\xi = \mathbf{Q}_\xi \quad \cdots\cdots (6)$$

This allows the motion of each body to be described by the motion of a linear motion element.

1.4 Analysis theory of hydraulic system[7)]

The hydraulic system shown in Fig. 2 is modeled. The following explains an example of a piping element, which is the basic element. For a piping element, it is necessary to express the compressibility and branching of hydraulic fluid in piping, and in the case of a piping element with three ports, the element motion equation described in terms of the flow rate product q_i of each port is given by Equation (7).

$$\rho\begin{bmatrix} l_1/A_1 & 0 & 0 \\ 0 & l_2/A_2 & 0 \\ 0 & 0 & l_3/A_3 \end{bmatrix}\begin{bmatrix}\ddot{q}_1\\ \ddot{q}_2\\ \ddot{q}_3\end{bmatrix} + \frac{\kappa}{V_0}\begin{bmatrix} \lambda_1^2 & \lambda_1\lambda_2 & \lambda_1\lambda_3 \\ \lambda_1\lambda_2 & \lambda_2^2 & \lambda_2\lambda_3 \\ \lambda_1\lambda_3 & \lambda_2\lambda_3 & \lambda_3^2 \end{bmatrix}\begin{bmatrix}q_1\\ q_2\\ q_3\end{bmatrix} = \begin{bmatrix}0\\0\\0\end{bmatrix} \quad \cdots (7)$$

This coefficient matrix constitutes the element mass matrix $\mathbf{M}_e$ and element stiffness matrix $\mathbf{K}_e$, as expressed by Equation (8).

$$\mathbf{M}_e = \rho\begin{bmatrix} l_1/A_1 & 0 & 0 \\ 0 & l_2/A_2 & 0 \\ 0 & 0 & l_3/A_3 \end{bmatrix},\ \mathbf{K}_e = \frac{\kappa}{V_0}\begin{bmatrix} \lambda_1^2 & \lambda_1\lambda_2 & \lambda_1\lambda_3 \\ \lambda_1\lambda_2 & \lambda_2^2 & \lambda_2\lambda_3 \\ \lambda_1\lambda_3 & \lambda_2\lambda_3 & \lambda_3^2 \end{bmatrix} \quad \cdots\cdots (8)$$

wherein ρ, l, A are hydraulic oil density, piping length, and cross-section, respectively; and κ, V_0, λ are the bulk modulus, volume in the piping, and the coordinate transformation coefficient showing the inflow/outflow at each port of the hydraulic fluid, respectively.

For piping pressure loss, the relationship between the pressure difference Δp and volume flow $\dot{q}$ is defined by Equation (9).

$$\Delta p = c_1\dot{q}^{1.75} + c_2\dot{q}^2 \quad \cdots\cdots (9)$$

Here, the first term of the right-hand side shows the pressure loss characteristics of a straight pipe and the second term shows the pressure loss characteristics for cases with rapid expansion/contraction, vent, elbows, and so on.

The coefficient c_1 is determined from various parameters such as the length of the straight pipe and the pipe diameter; c_2 is a coefficient determined by factors such as rapid expansion/contraction, vent, and elbows. A corrected external force is introduced into Equation (9) for the linearization at time t_n.

In addition, for a check valve for direction control and relief valve for pressure control, the relationship between pressure difference Δp and flow rate $\dot{q}$ is defined as an attenuation element with piecewise-linear characteristics. Likewise, a corrected external force is introduced into each of these for the linearization at time t_n.

In this way, the motion of the hydraulic system

can be described by a motion equation (Equation (10)).

$$\mathbf{M}_e\ddot{\mathbf{q}}_{n+1} + \mathbf{C}\dot{\mathbf{q}}_{n+1} + \mathbf{K}_e\mathbf{q}_{n+1} = \mathbf{f}_{n+1} - \bar{\mathbf{f}}_n \quad \cdots\cdots\cdots\cdots (10)$$

2. Digging operation simulation of hydraulic excavator

The modeling technique described in Section 1 was used for the dynamic simulation of the attachment in the digging operation of the hydraulic excavator. This section shows the validity of this technique by comparing the simulation results with the actual measurement results. In addition, the numerical stability of this technique is shown by solving the motion equations of the rigid body system and hydraulic system independently as a conventional technique to make a comparison with the results calculated by co-simulation, in which the state quantities are replaced at every time step.

2.1 Results of dynamic simulation for digging operation

The hydraulic excavator's digging operation was analyzed for one cycle and compared with actual measurement results. The digging operation is roughly classified into four working modes, i.e., drilling, boom raising/slewing, dumping, and boom lowering/slewing, in which all the actuators except for the traveling actuator are working. In this analysis, the lever input employed actually measured the operation lever pattern (pilot pressure) of each actuator, and the slewing speed employed measured speed as the target value. The digging reaction force from the ground was defined as a concentrated load on the bucket node and was given by a function defining the direction and the size in accordance with the angle and locus of the bucket. **Fig. 5** compares the result of the measurement of the cylinder stroke with the analysis result. The calculation time steps of the analysis were 1 ms and 10 ms. The comparison shows that the analysis results respectively agree with the experimental results by ±4% or less, verifying the validity of this analysis technique.

2.2 Evaluating numerical stability of analysis technique

In order to ensure the simultaneity of the analysis to be applied to HILS, it is important to ensure its numerical stability even when the time step width is increased. The numerical stability of this analysis technique is shown in **Fig. 6**, in which the analysis

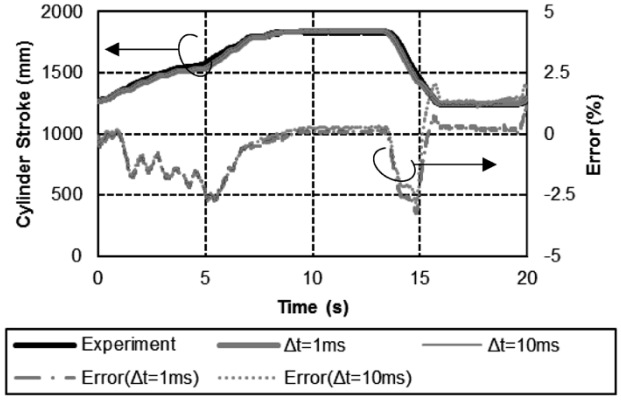

Fig. 5 Evaluation of numerical instability in digging operation (Δt = 1 ms, 10 ms)

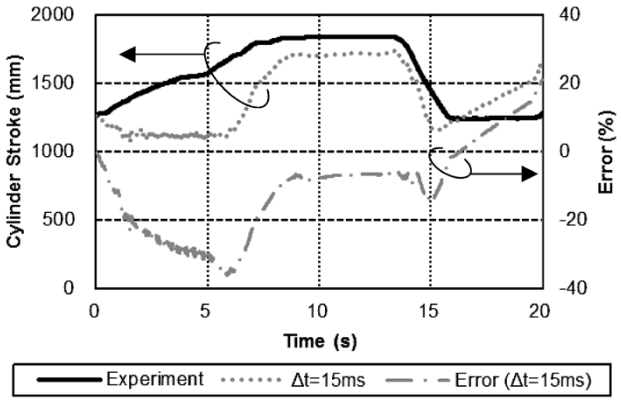

Fig. 6 Evaluation of numerical instability in digging operation (Δt =15 ms)

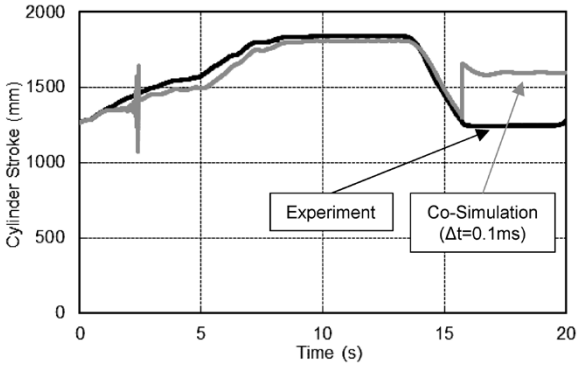

Fig. 7 Comparison of experimental and co-simulation technique results

was performed with a calculation time step of 15 ms. The fact that the time step of 15 ms results in a significant error deviating from the experimental results (approximately 35%) shows that an equivalent level of accuracy can be secured up to the time step of 10 ms.

On the other hand, in the conventional technique, the motion equations were solved for the rigid body system and the hydraulic system independently, and the state quantities are changed for each time step to carry out co-simulation. The results are shown in **Fig. 7**. It is shown that the accuracy is not sufficient

even when the time step is 0.1 ms.

As shown above, this stabilization technique improves the numerical stability of the coupled analysis of a rigid body system and hydraulic system, enabling the application of the coupled analysis to HILS.

3. HILS system for electric motors

The following describes an example of this stabilization technique used for a hybrid system where the upper slewing body is rotationally driven by an electric motor, and introduces an electric motor HILS system, in which the load acting on the electric motor during actual work is calculated in real time and reproduced on an electric-motor-load testing apparatus.

Fig. 8 shows the configuration of the electric-motor-load testing apparatus. This apparatus comprises an electric motor, dynamo, resolver, torque meter, control PC, and computation PC. In the computation PC, the digging operation of the hydraulic excavator is simulated on the basis of the coupled analysis model of a rigid body system and hydraulic system, described in the previous chapter, in which the slewing torque is derived from the operation input and is made to act on the electric motor by a dynamo as the load for the electric motor.

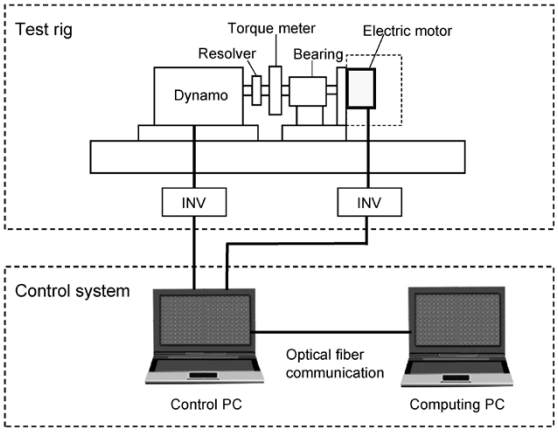

Fig. 8 Apparatus of load test for electric motor

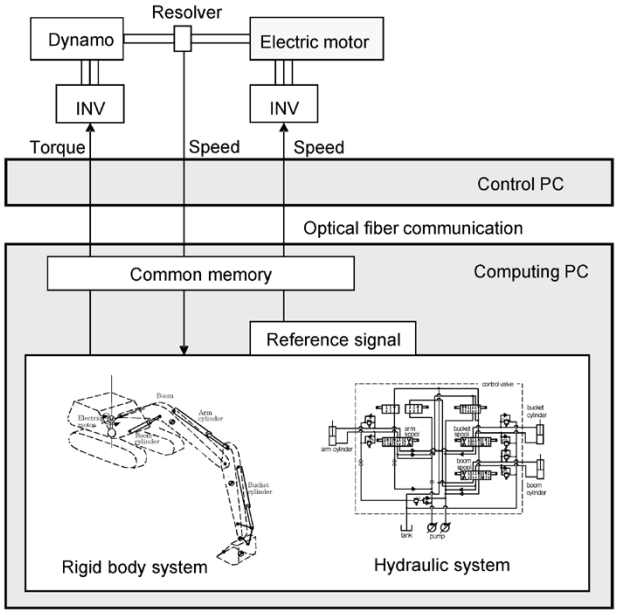

Fig. 9 Schematics of HILS system for electric motor

The mechanism of the electric-motor HILS system is explained on the basis of the signal flow among the components shown in **Fig. 9**. First, the target signal of an operation input for slewing speed is sent from the computation PC to the inverter of the electric motor via the control PC, and the rotation speed of the electric motor is controlled on the basis of the target signal. The actual RPM of the electric motor is detected by the resolver, and the load torque acting on the electric motor is calculated in the computation PC in real time in accordance with the RPM and is sent to the control PC.

The dynamo is torque-controlled by the control PC on the basis of the load torque.

4. Evaluation of dynamic simulation and electric motor HILS for hybrid system

The analysis model described in Section 2 is adapted for the electric motor HILS system to carry out the HILS evaluation of the electric motor during the digging operation of the hydraulic excavator. In this section, the analysis model of a hydraulic excavator with electric slewing function is prepared first to be compared with the actual work result to verify the validity of the analysis model. Next, HILS testing using the electric-motor-load testing apparatus is performed for comparison with the result of the analysis model so as to verify the validity of the electric motor HILS system.

4.1 Analysis model for electric motor[6)]

The electric motor is a permanent magnet type three-phase synchronous electric motor, and the equivalent circuit of the q-axis, among the equivalent direct current circuits represented by d-q coordinates (rotating coordinates rotating synchronously with rotating magnetic field), is modeled. The equivalent circuit of the q-axis in the electric motor model, taking into account the inverter loss, is shown in **Fig.10**. Assuming that the state quantities of the electric motor have 3 degrees of freedom, namely, the q-axis equivalent circuit current $\dot{q}_q$, q-axis equivalent iron loss current $\dot{q}_{cq}$, and electric motor RPM $\dot{\theta}_m$, the electric circuit equation[8)] and the motion equation are given by Equation (11).

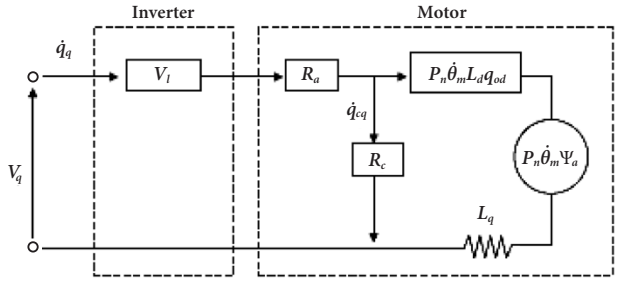

Fig.10 Equivalent circuit of q-axis in electric motor model

$$
\begin{aligned}
&L_q\ddot{q}_q - L_q\ddot{q}_{cq} + R_a\dot{q}_q + P_n\,\theta_m(L_d\dot{q}_{ad} + \Psi_a) = V_q - V_l \\
&L_q\ddot{q}_{cq} - L_q\ddot{q}_q + R_c\dot{q}_{cq} - P_n\,\dot{\theta}_m(L_d\dot{q}_{od} + \Psi_a) = 0 \quad \cdots\cdots (11) \\
&J_m\,\ddot{\theta}_m + C_m\,\dot{\theta}_m = T
\end{aligned}
$$

wherein L_d and L_q are the d-axis and q-axis inductance, respectively, of the electric motor, R_a is the electric motor winding resistance, R_c is the electric motor equivalent iron loss resistance, P_n is the number of the pole pairs, Ψ_a is the interlinkage magnetic flux, V_q is the equivalent circuit voltage of the q-axis, V_l is the inverter equivalent loss voltage drop, J_m is the electric motor inertia moment, C_m is the electric motor viscosity resistance, and T is the electric motor torque. It should be noted that the equivalent circuit current $\dot{q}_d$ of the d-axis is considered to be ideally controlled for its electric current phase, and Equation (12) is used.

$$\dot{q}_d = -\dot{q}_q \tan\beta \quad \cdots\cdots (12)$$

wherein β is the phase of the electric current vector.

On the basis of the above, Formula (11) as a matrix with $\dot{\mathbf{q}} = [\dot{q}_q \;\; \dot{q}_{cq} \;\; \dot{\theta}_m]$ can be described in the form of $\mathbf{M}\ddot{\mathbf{q}} + \mathbf{C}\dot{\mathbf{q}} + \mathbf{K}\mathbf{q} = \mathbf{f}$, which makes possible the superimposing of it upon the motion equations of the rigid body system and hydraulic system.

4.2 Validity evaluation of verification model

The verification analysis model consists of Equation (1), which is the motion equation of the rigid body system and hydraulic system, and Equation (11) which represents the electric circuit equation and motion equation of the electric motor. In order to verify the validity of this analysis model, one cycle of the digging operation of the excavator was analyzed and compared with the actual measurement results, in the same manner as in Section 2. In this analysis, the lever input employed was the actual measurement of the operation lever pattern (pilot pressure) of each actuator, and for the slewing speed, the measured speed was employed as the target. As an example, **Fig.11** compares the actual measurement results of the cylinder stroke with the analysis results. They agree with an error of ±2.5% or less, confirming the validity of the verification analysis model.

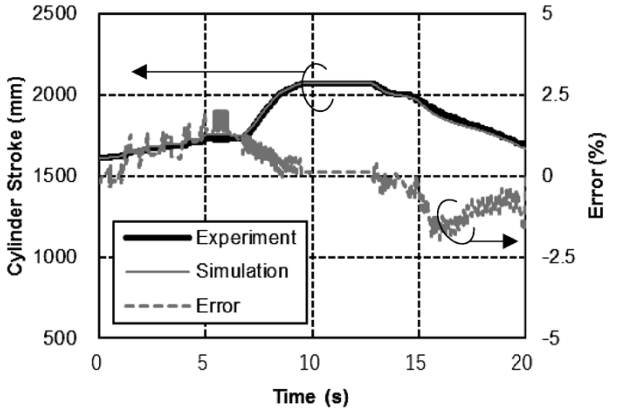

Fig.11 Comparison of experimental and analytical results in digging operation

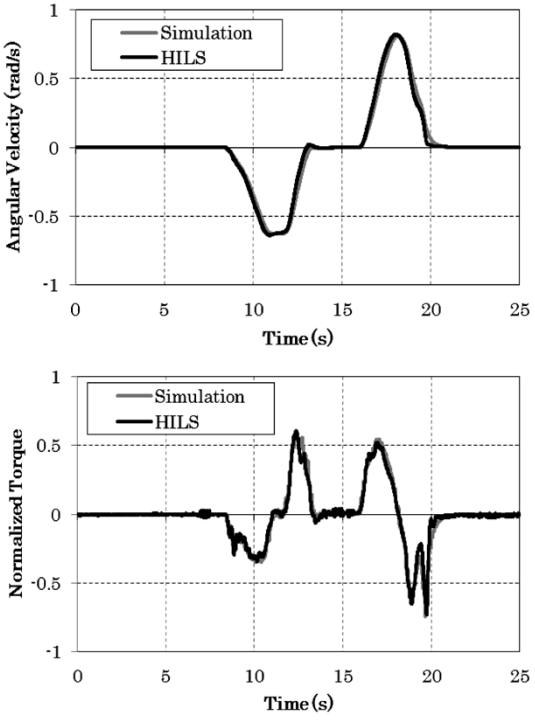

Fig.12 Comparison of responses of HILS system and those of simulation

4.3 HILS evaluation of electric motor during digging operation of hydraulic excavator

The HILS testing for one cycle of the digging operation of the hydraulic excavator was carried out by the electric-motor-load testing apparatus shown in Fig. 8 and Fig. 9 to verify the validity of the electric motor HILS system by comparison with the analysis results of the verification model shown in Subsection 4.2.

Fig.12 shows the slewing angular velocity and

normalized torque obtained by the analysis of the verification model and the HILS testing using the electric-motor-load testing apparatus. These figures confirm that the electric motor HILS system can reproduce the digging operation behaviors with a practically sufficient accuracy.

The following shows that the HILS system developed this time is effective for testing the digging of real machines. First, in the newly developed system, parameters such as the weight of the attachment and the position of the center of gravity of the hydraulic excavator are taken into account in the rigid body system model. In addition, characteristic values such as those of the hydraulic pump and valves are taken into account in the hydraulic system model. As a result, each design parameter can be changed easily in accordance with the change of the evaluation object. Moreover, it is possible to evaluate power that is difficult to measure with actual machines. For example, the evaluation of power loss generated in an electric motor and inverter requires the measurement of the input power and output power for each. Torque meter and power meters are difficult to install on actual equipment; however, they can easily be installed on the HILS system. This enables the detailed evaluation of losses and the designing of energy-saving systems.

Conclusions

This paper has introduced a modeling technique involving the transformation of the motion of a rigid body system from the motion of a rotating element to the motion of a linear motion element. It has also been shown that a numerical stability more excellent than that of the conventional method is obtained by using this technique in the coupled analysis of a rigid body system and hydraulic system.

In addition, this paper has introduced an electric motor HILS system for the hybrid system, in which both systems are driven by an electric motor, to calculate the load acting on the slewing electric motor in real time, and the results have been reproduced on an electric-motor-load testing apparatus. This system employs an analysis model that can be used for actual design development and is considered to be sufficiently useful as an evaluation tool for hybrid systems.

References

1) M. Kagoshima. *R&D Kobe Steel Engineering Reports.* 2012, Vol.62, No.1, pp.14-18.
2) Y. Nishida el al. *Komatsu technical report.* 2013, Vol.59, No.166, pp.2-8.
3) K. Hagiwara el al. *Transactions of the Society of Automotive Engineers of Japan, Inc..* 2002, Vol.33, No.3, pp.109-114.
4) T. Yamaguchi el al. *Transactions of the Japan Society of Mechanical Engineers*, 2013, Vol.79, No.806, pp.3420-3431.
5) K. Morita el al. *Transactions of the Japan Society of Mechanical Engineers*, 2014, Vol.80, No.813, p.DR0122.
6) K. Morita el al. *Transactions of the Japan Society of Mechanical Engineers*, 2017, Vol.83, No.845, p.16-00234.
7) E. Imanishi el al. *Transactions of the Japan Society of Mechanical Engineers*, 1987. Vol.53, No.492, pp.1711-1919.
8) Y. Takeda el al. *Umekomi jishaku dōki mōta no sekkei to seigyo*. Ohmsha, Ltd. 2010, pp.16-18.

Duct Shape Design Technology Based on Evolutionary Algorithm Considering Noise Attenuation Performance and Air Permeability

Satoshi TABUCHI*1

*1 AI Promotion Project Department, Technical Development Group

This paper relates to a technique for designing the engine room of a hydraulic excavator equipped with an Integrated Noise & Dust Reduction (iNDr) cooling system. In order to improve the noise attenuation performance, changes in cross-sectional area and bends have been introduced into the muffler duct of the iNDr structure. On the other hand, changes in cross-sectional area and bending will deteriorate the air permeability and decrease the cooling capacity. Thus, in a muffler duct, the air permeability of the cooling air and noise attenuation performance are in a trade-off relationship. Against this backdrop, an optimum design technology has been developed using a multi-objective genetic algorithm (MOGA) to achieve both air permeability and noise attenuation performance in the intake duct of the iNDr structure of the engine room. This technology has enabled the design of an engine-room shape taking both the air permeability and noise attenuation performance into account.

Introduction

Construction in urban areas and during nighttime is increasing, and there is an increasing demand for reducing the noise of construction machinery, considering the environment around work sites and improving the working environment for operators. Kobelco Construction Machinery Co., Ltd. developed an Integrated Noise & Dust Reduction Cooling System (iNDr) to reduce the noise level (**Fig. 1**).[1] The iNDr has improved the soundproofing performance by closing gaps in the engine room and employing an offset duct structure, in which the inlet and outlet openings for cooling air are disposed only on the upper surface of the machine body. As a result, the hearing ability of workers in the vicinity is secured, thus improving their safety, and noise in work site neighborhoods has been improved.

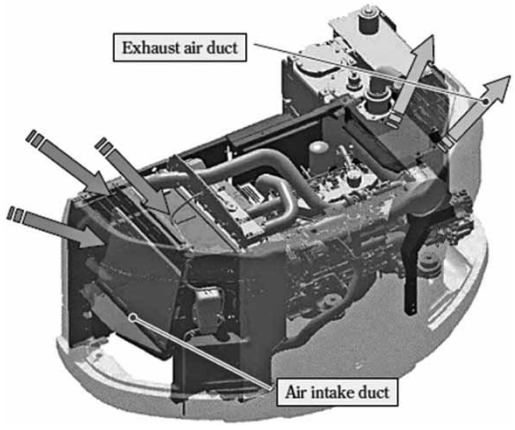

Fig. 1 Structure of iNDr[1]

In the meantime, the strengthening of emissions regulations in recent years has been causing changes in the design of cooling systems to cope with the increasing amount of heat generated in engines, as well as changes in the layout of the machine bodies due to the addition of exhaust purification devices.

In the case of the iNDr, any change in the layout of the machine body requires its duct shape to be determined so as to minimize the leakage of sound from the opening of its offset duct and, at the same time, to secure the amount of cooling air necessary for establishing the heat balance; it is difficult to solve these issues simultaneously. So far, the structure of the iNDr duct has been determined by repeated examinations with numerical analysis and bench testing, posing a challenge to shortening the development period.

It was against this backdrop that a technique using an evolutionary algorithm (hereinafter referred to as "EA")[2] was developed to design a duct taking both the ventilation resistance and noise attenuation performance into account. This paper introduces an example applied to the designing of the iNDr intake duct.

1. Optimization of duct shape using evolutionary algorithm

1.1 Optimization technique

The design of an intake duct must take both the ventilation resistance and noise attenuation into account, posing a problem of two-objective optimization with the objective functions of ventilation resistance and noise attenuation. In this paper, a multi-objective optimization technique is used to pursue the right duct shape for achieving both low resistance and low noise. The duct shape has been optimized by the genetic algorithm (hereinafter referred to as "GA") that is considered to be the most common among the EAs for multi-

objective optimization.

1.2 Genetic algorithm

A GA is an optimization technique inspired by the evolutionary process of living organisms and has the capability of being adapted for complicated objective functions. It is often used when there are many design variables. This is owing to the global solution searching capability of GAs even for multimodal objective functions.

Fig. 2 shows the solution procedure using a genetic algorithm. The GA consists of the process steps of Initialization generating multiple individuals, followed by Selection, Crossover, Mutation, and Evaluation of the individuals.

In Initialization, a range of possible values for each design parameter is preset, and a plurality of design solution candidates composed of a combination of a plurality of design parameters is generated using random numbers. In Evaluation, the performance of each design solution candidate generated is digitalized and evaluated, and excellent design solutions with high evaluation values are chosen in Selection.

In Crossover, two design solutions are selected from the plurality of design solutions generated, and one with a combination of design parameters similar to those two design solutions is newly generated. Mutation is an operation that changes, at a certain probability, some parts of the parameters of the design solution with random numbers so as to create new combinations of design parameters. This operation guarantees the diversity of the solutions and prevents them from being mere local optimal solutions.

While the steps of Selection, Crossover, Mutation, and Evaluation are being repeated, the features combining excellent design parameters are inherited during the search for new solutions, enabling the search for a solution with the highest evaluation value of the target performance. In actual design, it is important to obtain solutions in a short time. Because GA repeatedly performs the creation and evaluation of design solutions, an evaluation method with a high calculation load is not suitable for the evaluation of performance. Hence, an approximate expression of the objective function with variables of the design parameters was constructed from the results of the numerical analysis of a small number of simple shapes and was used for the evaluation. This made it possible to significantly shorten the time, compared with using numerical analysis for the evaluation of the objective function.

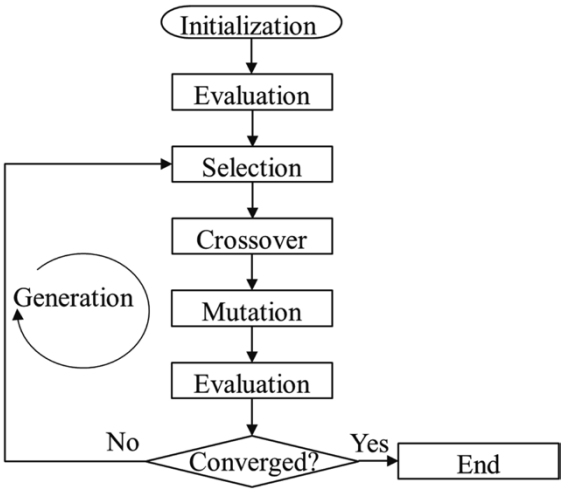

Fig. 2 Procedure for solving by genetic algorithm

2. Application to designing of intake duct

2.1 Duct shape

Fig. 3(a) is the schematic diagram of an intake duct for an iNDr system. This iNDr intake duct is simplified to produce the model shown in Fig. 3(b). The following is a consideration of the optimization of the simplified duct shape in Fig. 3(b). The intake duct of an iNDr is configured to take in the outside air from a rectangular opening on the top while the fan installed in the circular opening in the lateral face is in operation. Now, the duct is divided into two parts (**Fig. 4**(a)-(c)), and ventilation resistance and noise attenuation performance are evaluated for each of the duct parts. Here, the part shown in Fig. 4(b) is referred to as Duct A, and the part shown in Fig. 4(c) is referred to as Duct B. The outer shape of the duct was regarded as being defined by fixed values, since it is affected by the size of the machine body. As shown in Fig. 4, the design variables were set to be the ten dimensions defining the opening area and the opening position of the intake duct.

2.2 Mathematical modeling of ventilation resistance

The prediction equation for pressure loss in an

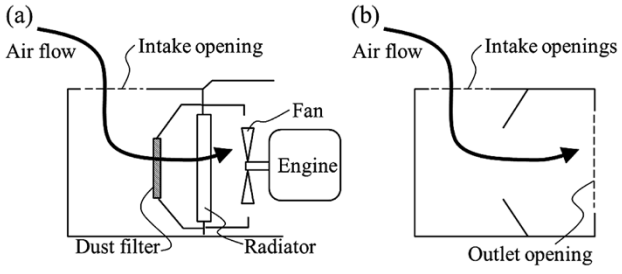

Fig. 3 Schematic image of intake duct
(a) iNDr system (b) simplified model

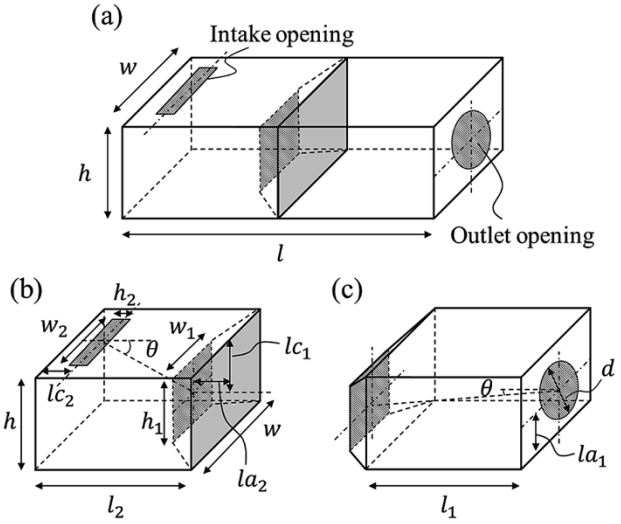

Fig. 4 Design variables for intake duct
(a) whole model (b) Duct A (c) Duct B

expansion-type silencer is proposed by Yoshihara,[3] and the prediction equation for pressure loss in an S-type silencer like Duct A is given by Equation (1). Shapes like that of Duct B are classified into Q-type and P-type depending on the presence or absence of an eccentric angle, and their pressure losses are expressed by Equations (2) and (3), respectively:

$$\Delta P = 1.808 m_A^{\frac{1}{8}} n_A^{\frac{1}{12}} \frac{\rho v^2}{2} \quad \cdots\cdots (1)$$

$$\Delta P = 0.324 m_B^{\frac{1}{8}} n_B^{\frac{3}{4}} \frac{\rho v^2}{2} (\text{for } \theta = 0) \quad \cdots\cdots (2)$$

$$\Delta P = 2.021 m_B^{\frac{1}{8}} n_B^{\frac{1}{12}} (\tan\theta)^{\frac{1}{8}} \frac{\rho v^2}{2} (\text{for } \theta \neq 0) \quad \cdots\cdots (3)$$

wherein,

ΔP: pressure loss of the duct
m_A (=S_C / S_A): expansion ratio of Duct A
m_B (=S_C / S_B): expansion ratio of Duct B
S_A (=$h_2 w_2$): opening area on the inflow side of Duct A
S_B (=$h_1 w_1$): opening area on the inflow side of Duct B
S_C (=h_w): cross-sectional area of the duct
n_A (=l_2 / d_A): cavity length ratio of Duct A
n_B (=l_1 / d_B): cavity length ratio of Duct B
d_A : hydraulic equivalent diameter of the opening on the inlet side of Duct A
d_B : hydraulic equivalent diameter of the opening on the inlet side of Duct B
θ : eccentric angle
ρ : air density
v : average flow velocity on inflow side

Yoshihara's equation is an estimation equation based on the experimental results for an inlet with a fixed inner diameter. Hence, in order to make the inlet shape serve as a shape design parameter, it is necessary to newly construct a prediction expression that takes into account the influence of the inlet shape.

For the mathematical modeling of ventilation resistance described in this paper, computational fluid dynamics (hereinafter referred to as "CFD") was used to calculate the pressure loss values of multiple ducts to construct experimental equations expressing the relationship among the dimensions of the duct and its pressure loss.

The duct subjected to shape optimization this time has 10 dimensions as its design parameters. In order to suppress the number of cases to be analyzed, the design parameters were selected using L18 orthogonal arrays so that the combination of design parameters greatly varies from case to case. Eighteen cases of analysis conditions were set on the basis of the L18 orthogonal arrays, and 18 types of numerical analyses were performed in each case to construct experimental equations from the results obtained by the numerical analyses. **Table 1** and **Table 2** respectively show the design parameters of Duct A and Duct B subjected to CFD. **Fig. 5** shows an example of the computational meshes used for the analysis.

Fig. 6 shows the factor effect diagram for Duct A, while **Fig. 7** shows the same for Duct B. As shown in Fig. 6, the pressure loss value of Duct A decreases with increasing opening width w_1 and opening height h_1 on the outflow side. It is found that the pressure loss is particularly sensitive to the change of the opening width w_1 on the outflow side. Fig. 7 shows that the pressure loss decreases as the diameter d of the opening on the outflow side increases. Yoshihara's equation does not include the

Table 1 L18 orthogonal arrays for Duct A

Case	l_2	la_2	lc_1	lc_2	h_1	h_2	w_1	w_2
1	0.60	0.10	0.35	0.20	0.40	0.25	0.30	0.30
2	0.60	0.10	0.40	0.25	0.50	0.30	0.50	0.50
3	0.60	0.10	0.45	0.30	0.60	0.35	0.70	0.70
4	0.80	0.10	0.45	0.25	0.60	0.25	0.50	0.30
5	0.80	0.10	0.35	0.30	0.40	0.30	0.70	0.50
6	0.80	0.10	0.40	0.20	0.50	0.35	0.30	0.70
7	1.00	0.10	0.45	0.20	0.50	0.30	0.70	0.30
8	1.00	0.10	0.35	0.25	0.60	0.35	0.30	0.50
9	1.00	0.10	0.40	0.30	0.40	0.25	0.50	0.70
10	0.60	0.20	0.35	0.30	0.50	0.35	0.50	0.30
11	0.60	0.20	0.40	0.20	0.60	0.25	0.70	0.50
12	0.60	0.20	0.45	0.25	0.40	0.30	0.30	0.70
13	0.80	0.20	0.40	0.30	0.60	0.30	0.30	0.30
14	0.80	0.20	0.45	0.20	0.40	0.35	0.50	0.50
15	0.80	0.20	0.35	0.25	0.50	0.25	0.70	0.70
16	1.00	0.20	0.40	0.25	0.40	0.35	0.70	0.30
17	1.00	0.20	0.45	0.30	0.50	0.25	0.30	0.50
18	1.00	0.20	0.35	0.20	0.60	0.30	0.50	0.70

Table 2 L18 orthogonal arrays for Duct B

Case	l_1	la_1	la_2	lc_1	h_1	w_1	d
1	0.30	0.55	0.10	0.35	0.40	0.30	0.40
2	0.30	0.45	0.20	0.40	0.50	0.50	0.50
3	0.30	0.35	0.30	0.45	0.60	0.70	0.60
4	0.40	0.45	0.10	0.45	0.60	0.50	0.40
5	0.40	0.35	0.20	0.35	0.40	0.70	0.50
6	0.40	0.55	0.30	0.40	0.50	0.30	0.60
7	0.50	0.55	0.10	0.45	0.50	0.70	0.50
8	0.50	0.45	0.20	0.35	0.60	0.30	0.60
9	0.50	0.35	0.30	0.40	0.40	0.50	0.40
10	0.60	0.35	0.10	0.35	0.50	0.50	0.60
11	0.60	0.55	0.20	0.40	0.60	0.70	0.40
12	0.60	0.45	0.30	0.45	0.40	0.30	0.50
13	0.70	0.35	0.10	0.40	0.60	0.30	0.50
14	0.70	0.55	0.20	0.45	0.40	0.50	0.60
15	0.70	0.45	0.30	0.35	0.50	0.70	0.40
16	0.80	0.45	0.10	0.40	0.40	0.70	0.60
17	0.80	0.35	0.20	0.45	0.50	0.30	0.40
18	0.80	0.55	0.30	0.35	0.60	0.50	0.50

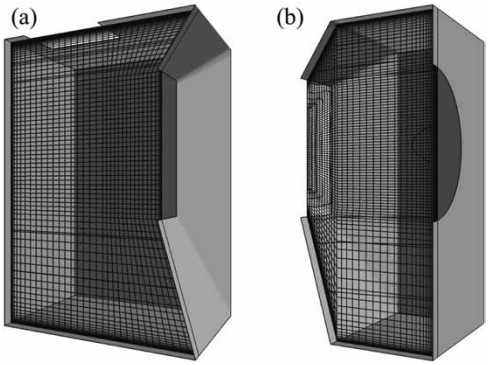

Fig. 5 Analytical models of intake ducts by CFD method
(a) Duct A, (b) Duct B

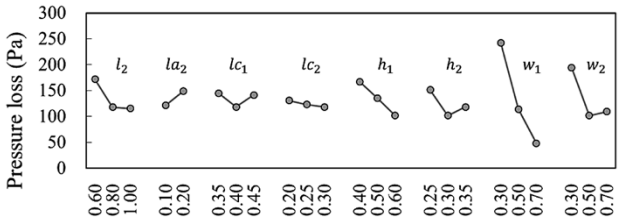

Fig. 6 Factor effect of Duct A

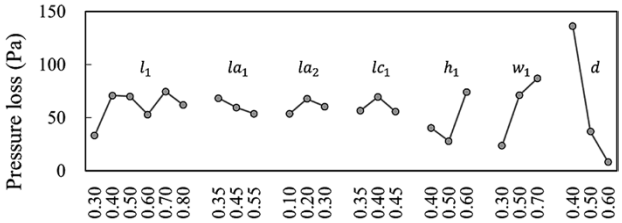

Fig. 7 Factor effect of Duct B

parameters related to the dimensions of the opening on the outflow side and is not capable of evaluating the changes in pressure loss due to the change in the shape of the outflow-side opening.

Hence, the modified equation takes into account not only the average flow velocity on the inflow side but also the average flow velocity on the outflow side. The modified equation consists of the weighted sum of the pressure loss value obtained by substituting the average flow velocity on the inflow side into Equations (1) through (3) and the pressure loss value obtained by substituting the average flow velocity on the outflow side into Equations (1) to (3). Moreover, the flow passage of Duct A has a bend of 90 degrees, and the length of the flow passage at the bent portion is considered to affect the pressure loss value. Hence, in addition to the area ratio of inflow side opening and outflow side opening, the length of the path connecting the center of the inflow side opening and the center of the outflow side opening was adopted as the weighting factor. For Duct B, the area ratio of inflow side opening and outflow side opening is assumed to contribute to the pressure loss value and was adopted as a weighting factor. Equations (4) to (9) are expressions predicting the pressure loss obtained. The prediction equation of pressure loss for Duct A is given by Equation (4):

$$\Delta P_A = \Delta P_{out} + \Delta P_{in} \frac{S_{in}}{S_{out}} \frac{(h_1/2)/h}{(l_2 - l_{c2} - l_{a2})/l_2} \quad \cdots\cdots (4)$$

wherein,

$$\Delta P_{in} = 1.808 m_A^{\frac{1}{8}} n_A^{\frac{1}{12}} \frac{\rho v_{in}^2}{2} \quad \cdots\cdots (5)$$

$$\Delta P_{out} = 1.808 m_A^{\frac{1}{8}} n_A^{\frac{1}{12}} \frac{\rho v_{out}^2}{2} \quad \cdots\cdots (6)$$

The prediction equation of pressure loss for Duct B is given by Equation (7).

$$\Delta P_B = \Delta P_{in} + \Delta P_{out} \left(\frac{S_{in}}{S_{out}} \right)^{0.2} - 20 \quad \cdots\cdots (7)$$

wherein,

$$\Delta P_{in} = \begin{cases} 0.324 m_B^{\frac{1}{8}} n_B^{\frac{1}{12}} \dfrac{\rho v_{in}^2}{2} & (\text{for } \theta = 0) \\ 2.021 m_B^{\frac{1}{8}} n_B^{\frac{1}{12}} (\tan\theta)^{\frac{1}{8}} \dfrac{\rho v_{in}^2}{2} & (\text{for } \theta \neq 0) \end{cases} \quad \cdots\cdots (8)$$

$$\Delta P_{out} = \begin{cases} 0.324 m_B^{\frac{1}{8}} n_B^{\frac{1}{12}} \dfrac{\rho v_{out}^2}{2} & (\text{for } \theta = 0) \\ 2.021 m_B^{\frac{1}{8}} n_B^{\frac{1}{12}} (\tan\theta)^{\frac{1}{8}} \dfrac{\rho v_{out}^2}{2} & (\text{for } \theta \neq 0) \end{cases} \quad \cdots\cdots (9)$$

Fig. 8 and **Fig. 9** show the pressure loss values obtained by CFD with the shapes shown in Table 1 and Table 2 (Calculation), the pressure loss values estimated by Yoshihara's equation, and the pressure loss values calculated from Equation (4) and Equation (7) (Modified equation). The Yoshihara's

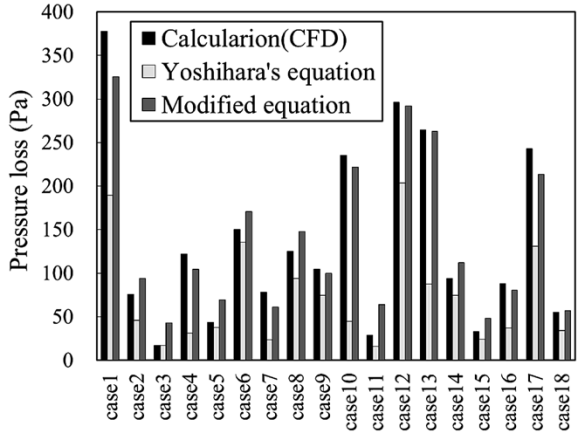

Fig. 8 Comparison of the estimated pressure loss in Duct A

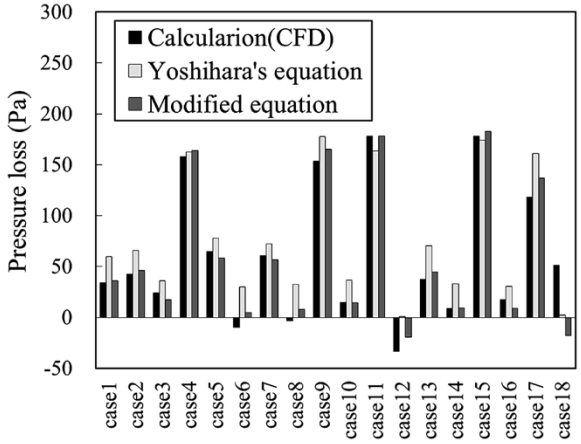

Fig. 9 Comparison of the estimated pressure loss in Duct B

equation departs from the CFD results, depending on the shape of the duct. This is probably because it is an estimation equation constructed on the basis of the experimental results when the inlet side inner diameter is fixed, and the pressure loss value cannot be accurately estimated for the duct shapes that are outside the applicable range. It is shown that Modified equation (4) and Modified equation (7) are the expressions that can reproduce the trends of the CFD results.

2.3 Mathematical modeling of noise attenuation performance

In the evaluation of Duct A's noise attenuation performance, a publicly known mathematical expression model is used, in which Duct A is regarded as a sound absorbing chamber. For the range of frequencies whose wavelengths are shorter than the dimensions of the duct, Equation (10) is used in accordance with the theory of indoor sound fields.[4] On the other hand, if the dimensions of the tube and the cavity are smaller than the wavelength of the sound and in the handling range of the plane wave, the attenuation amount of the insertion tube cavity is expressed by Equation (11).[5] Now, Duct B is regarded as an insertion tube cavity, and the noise attenuation performance is evaluated by Equation (11).

$$R_A = 10\log_{10}\left\{\frac{1}{S_{out}\left(\frac{\cos\theta}{2\pi d'}+\frac{1-\alpha}{\alpha S_w}\right)}\right\} \quad \cdots\cdots\cdots\cdots \quad (10)$$

$$R_B = 10\log_{10}\frac{1}{4}\left\{\left(1+\frac{S_c/S_{in}}{S_c/S_{out}}\right)\cos^2 kl_1 + \left(\frac{S_c}{S_{in}}+\frac{1}{S_c/S_{out}}\right)^2\sin^2 kl_1\right\} + 10\log_{10}\left(\frac{S_c/S_{out}}{S_c/S_{in}}\right) \quad \cdots\cdots\cdots \quad (11)$$

wherein,

- α : average indoor sound absorption coefficient
- S_{out}: outlet cross-sectional area
- S_c: cavity cross-sectional area
- S_{in}: inlet cross-sectional area
- S_W: duct interior surface area
- k: wavenumber
- d': distance between the inlet and outlet
- θ : the angle between the outlet opening plane and the direction connecting the inlet center and the outlet center.
- l_l: cavity length.

Because wavenumber k varies with frequency f_x, the noise attenuation performance of the duct expressed by Equations (10) and (11) has frequency dependence. Therefore, in order to reduce the OA value of the noise leaking out from the duct, it is necessary to assign frequency characteristics to the attenuation amount in accordance with the frequency characteristics of the noise source. Hence, in evaluating the noise attenuation performance of the muffler duct, the attenuation amounts $R_A(f_x)$ and $R_B(f_x)$ of the muffler duct were subtracted from the acoustic power level $L_{source}(f_x)$ of the sound source in each frequency band f_x to obtain a noise level $L(f_x)$, and the overall (OA) value, L_{OA}, was obtained by combining the noise levels of all the frequency bands. Equations (12) and (13) show the calculation formulae for the OA value, L_{OA}, and the noise level $L(f_x)$.

$$L_{OA} = 10\log_{10}\left(\sum 10^{\frac{L(f_x)}{10}}\right) \quad \cdots\cdots\cdots\cdots\cdots\cdots \quad (12)$$

$$L(f_x) = L_{source}(f_x) - \{R_A(f_x) + R_B(f_x)\} \quad \cdots\cdots\cdots\cdots \quad (13)$$

In this paper, the noise radiated from the engine and hydraulic pump of a hydraulic excavator was measured and used as the sound source.

2.4 Optimization of design parameter based on genetic algorithm

This paper describes a duct whose size has been randomly determined within the constraint range

of the design, in which the performance is evaluated using the ventilation resistance formula model and the noise attenuation performance formula model described above. The combinations of design variables determineded to have low ventilation resistance and high noise attenuation performance are kept as excellent combinations, while the combinations of design variables determined to have low performance are deleted. Repeating the above procedure weeds out any combinations other than those with low ventilation resistance and high noise attenuation performance, in the end, obtaining the combination of optimum design variables.

This problem is formulated as Equations (14):

$$\begin{aligned} &\textit{Minimize} \quad F_1 = \Delta P_A + \Delta P_B \\ &\textit{Minimize} \quad F_2 = L \\ &\textit{subject to} \quad G_1 > 0,\ G_2 > 0,\ \cdots,\ G_6 > 0 \end{aligned} \qquad \cdots\cdots \quad (14)$$

The outer shape of the duct has a maximum value determined by the size of the machine body, and constraint conditions are generated for the design parameter representing the inner shape of the duct.

The constraint conditions, G_1 to G_6, are given by Equations (15).

$$\begin{aligned} G_1 &= l_{c1} - \frac{1}{2} h_1 \\ G_2 &= h - \left(l_{c1} + \frac{1}{2} h_1 \right) \\ G_3 &= l_{c2} - \frac{1}{2} h_2 \\ G_4 &= l_2 - \left(l_{a2} + l_{c2} + \frac{1}{2} h_2 \right) \\ G_5 &= h - \left(l_{a1} + \frac{1}{2} d \right) \\ G_6 &= l_{a1} - \frac{1}{2} d \end{aligned} \qquad \cdots\cdots \quad (15)$$

When applied to GA, the constraint conditions G_1 to G_6 in Equations (14) were regarded as unconstrained optimization problems on the basis of the penalty function method.

Fig.10 shows the distribution of ventilation resistance and noise level of the initial population generated by initialization, while **Fig.11** is an example of a set of design solutions obtained by GA. The comparison of the initial population of the design solution with the distribution of the final generation clarifies that the optimization using GA weeds out the design solution with large ventilation resistance and noise level to obtain a favorable design solution for ventilation resistance and noise level. The Pareto optimal solutions shown in Fig.11 are ones in which an attempt to improve either the ventilation resistance or noise level deteriorates the other. The design solution is selected from these Pareto optimum solutions in consideration of the individual importance of ventilation resistance and noise level.

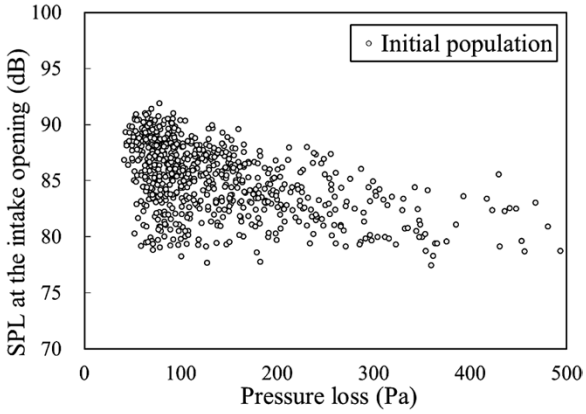

Fig.10 Distribution of the initial population

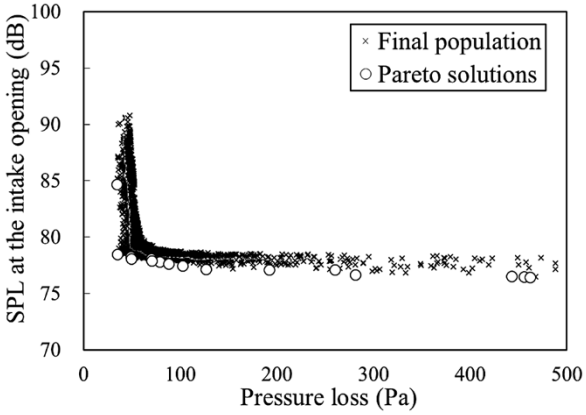

Fig.11 Distribution of the final population

3. Application to actual machines

The following describes the results of changing the intake duct layout, in which the change was made with reference to the ventilation resistance obtained by the optimization using GA and to the Pareto optimum solution of intake duct shape for reducing the noise level. In the case of the optimization using GA, the Pareto optimum solution is characterized by the enlarged opening area of the intake opening and the installation position of the dust filter being placed lower than in the conventional layout. This has been adopted as the shape of a new duct. Considering the placement of equipment to be installed inside the intake duct, the design parameters which are difficult to reproduce have been designed to take values as close as possible to the respective Pareto solutions. The acoustic power level in the intake opening of the new duct shape is shown in **Fig.12**. **Fig.13** shows the change rate of pressure loss before and after the change from conventional shape to new shape. As shown in Fig.12, the acoustic power level at

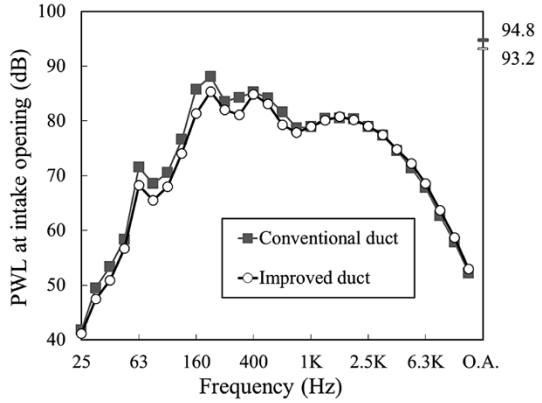

Fig.12 PWL at intake opening

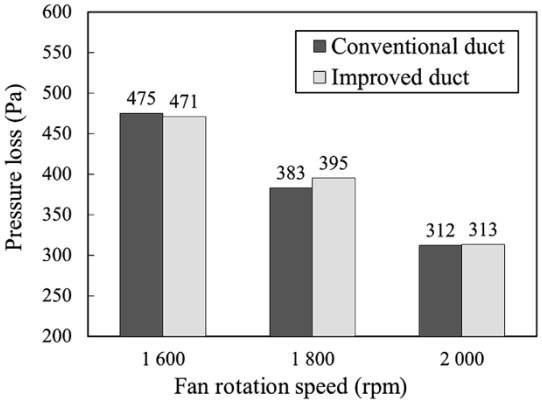

Fig.13 Change in pressure loss

the intake opening has decreased from 94.8 dB to 93.2 dB in terms of O.A. value, thanks to the shape change of the intake duct. As shown in Fig.13, the pressure loss deteriorates by approximately 3% at 1,800 rpm. However, it has achieved almost the same performance as the conventional shape.

As described above, the optimization technique according to this paper has made it possible to quickly implement the design of the duct to realize low noise while satisfying the cooling performance.

Conclusions

This paper has introduced a shape optimization technique using GA as a design technique to achieve both a low pressure loss and high noise attenuation performance of ducts. In this paper, the ventilation resistance and noise attenuation performance of the ducts subject to optimization are expressed by a mathematical model. Furthermore, the present model may be substituted with a response surface model based on the neural network or Kriging response surface method, enabling a solution to various design problems. We will strive to contribute to the development of machine products that meet the needs of society by applying this method.

References

1) H. Nakajima el al. *R&D Kobe Steel Engineering Reports*. 2012, Vol.62, No. 1, pp. 27-31.
2) M. Kubo et al. *Metaheuristics: A Programming Guide*, First edition, Kyoritsu Shuppan CO. LTD, 2009, pp. 61-62.
3) T. Yoshihara. *Ebara Engineering Review*. 1985, No. 130, pp.2-7.
4) H. Utsuno el al. *R&D Kobe Steel Engineering Reports*.1999, Vol.49, No.1, pp.56-59.
5) T. Katsuta el al. *AIJ Journal of Technology and Design*, 1959, 62, pp.79-85.

Loss Analysis of Electric Motors in Hybrid Excavator

Akira TSUTSUI*1, Ryo FUJISAWA*2, Kazuhide SEKIYAMA*2, Yoichiro YAMAZAKI*3, Seiji SAEKI*3, Dr. Kazushige KOIWAI*4

*1 Applied Physics Research Laboratory, Technical Development Group
*2 Mechanical Engineering Research Laboratory, Technical Development Group
*3 Advanced Technology Department, Design & Development Engineering Division, Global Engineering Center (GEC), KOBELCO CONSTRUCTION MACHINERY CO., LTD.
*4 Corporate Planning & Administration Department, KOBELCO CONSTRUCTION MACHINERY CO., LTD.

Kobelco Construction Machinery Co., Ltd. has launched a new 20 tonne hybrid excavator, equipped with two types of newly developed electric motors, namely, a permanent magnet type, flat, high-torque generator motor, and a compact high-output slewing motor. In an electric motor, iron loss and copper loss occur, and these losses increase as the internal temperature rises. Therefore, the challenge in making compact electric motors with high torque and high output is to release the heat generated inside the motors to the outside and to prevent their internal temperature from rising. A technique has been established for the coupled analysis of an electrical/magnetic circuit model and a heat transfer circuit model in an electric motor that enables an optimal design of the heat transfer path inside the motor, as well as making it possible to efficiently find an appropriate electromagnetic circuit for it. This has resulted in the development of electric motors with high torque density.

Introduction

Kobelco Construction Machinery Co., Ltd. has commercialized hybrid excavators, each with a diesel engine equipped with a generator motor for power assist, in which the slewing system, which used to be driven hydraulically, is driven electrically. The company has launched 8 tonne machines and 20 tonne machines into the market so far. These products, however, employ general purpose devices for their power electronics such as generators, slewing electric motors, and inverters; these devices are large and expensive. Also, exclusive designs that are different from those of the standard hydraulic excavators are increasingly being used for the main body of these excavators to accommodate the spaces for installing the power electronics devices, posing a challenge in terms of cost.

Hence, in the new 20 tonne hybrid excavator, each power electronics device was downsized with our own exclusive design. For example, the generator motor has been flattened, with higher torque, and built-in between the engine and hydraulic pump. In addition, the slewing electric motor was downsized with a higher output so that it can fit in the installation space in each slewing hydraulic motor.

In this development, an analysis technology was established to quickly verify the output performance, efficiency, and feasibility of heat balance, so as to develop a small, high-output electric motor in a short time. This paper outlines this analysis technology.

1. Challenges in designing electric motor with high torque density

Heat dissipation/cooling is an issue in downsizing an electric motor with high output. In electric motors, heat is generated by copper loss, iron loss, and mechanical loss. Downsizing an electric motor decreases the heat transfer area for heat dissipation, which raises the internal temperature, making its coil more susceptible to burn out. This temperature rise increases the resistance value of the coil, which causes the copper loss to increase, leading to a further rise in temperature. In addition, the rising internal temperature causes the thermal demagnetization of the magnet, leading to a decrease in the output.[1] Moreover, the electromagnetic-steel sheet used for iron cores tends to experience increased iron loss when stress is applied.[2] Therefore, it is possible that the iron loss is increased due not only to the residual stress at the time of forming such as punching,[3] but also to the change in thermal stress caused by the rise in internal temperature.

Furthermore, the increase in iron loss also lowers the output torque of the electric motor.[1, 4] Current control by an inverter to maintain the target output torque results in an increased input current, further increasing the above-mentioned copper loss, iron loss, and temperature rise, making it difficult to achieve the target output performance.

Thus, in the design of an electric motor with high torque, it is necessary to consider electromagnetic design and heat transfer design as a coupled problem to be optimized. One means for performing this is a magnetic field analysis and heat transfer analysis using three-dimensional FEM. Coupling these two analyses to derive the optimum solution, however, results in a high calculation load and does not necessarily facilitate the study of the design change.

To solve these problems, Kobe Steel has used an electromagnetic field analysis method based on

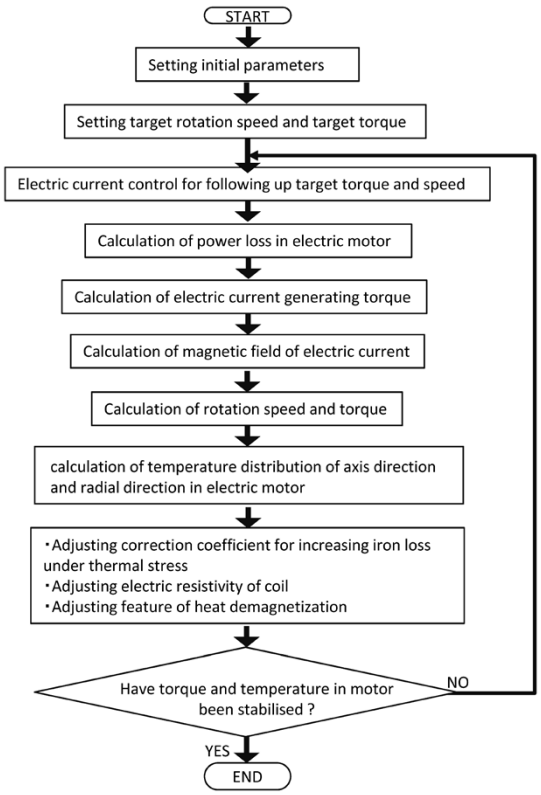

Fig. 1 Process of coupled simulation for electromagnetic circuit and heat transfer

the voltage equations for conventional motors and magnetic circuit calculations in accordance with the permeance method,[4] incorporating therein a process of calculating the amount of heat generated considering the temperature dependence of copper loss and stress dependence of iron loss. A simple analysis technique (**Fig. 1**) was also established to enable the electromagnetic circuit designing of an electric motor while visualizing the two-dimensional heat transfer state and temperature distribution in the axial direction and radial direction inside the electric motor. A small, high-output electric motor satisfying the requirements for the new hybrid excavator has been realized by utilizing this simple analysis technique. The following explains the calculation method for each loss and analytical model of heat transfer in this simplified analysis technique.

2. Calculating amount of heat generated inside electric motor

2.1 Calculating iron loss of stator iron-core and rotor iron-core

Iron loss is the main heat generation factor of the stator iron-core, rotor iron-core, and magnet of an electric motor. The calculation method adopted was the Steinmetz empirical equation (Equation (1)),

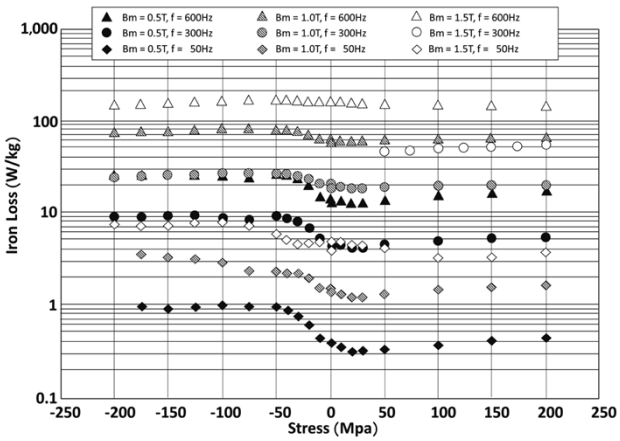

Fig. 2 Relationship between stress and iron loss

which takes into account the influence of frequency and magnetic flux density on both the hysteresis loss, W_h, and eddy current loss, W_e;

$$W_F = W_h + W_e = K_h f B_m{}^{1.6} + K_e \frac{(tfB_m)^2}{\rho} \quad \cdots\cdots\cdots\cdots\cdots (1)$$

wherein W_F is iron loss; W_h, hysteresis loss; W_e, eddy current loss; K_h, hysteresis loss coefficient; K_e, eddy current loss coefficient; t, iron plate thickness; ρ, the resistivity of the magnetic body; and B_m, the maximum magnetic flux density of the magnetic flux currently occurring.

The proportion factors K_h and K_e/ρ of hysteresis loss and eddy current loss, respectively, are determined on the basis of the data for high-frequency iron loss curves, published by the manufacturers of electromagnetic steel sheets, to organize the relation between frequency and magnetic flux density. This equation is regarded as the basic equation.

On the other hand, the hysteresis loss and eddy loss of an iron core increase with stress[5], which must be taken into account. For this reason, as shown in Equation (2), the correction factors K_{fh} and K_{fe} are incorporated into Equation (1) to increase each loss in accordance with the stress change, and, at the same time, the characteristics of iron loss change are evaluated by a stress test (**Fig. 2**) so as to change K_{fh} and K_{fe} with the increase/decrease ratio of the loss in accordance with the stress change to calculate the iron loss.

$$W_F = K_h K_{fh} f B_m{}^{1.6} + K_e K_{fe} \frac{(tfB_m)^2}{\rho} \quad \cdots\cdots\cdots\cdots\cdots (2)$$

wherein K_{fh} is the correction factor for hysteresis loss, and K_{fe} is the correction factor for eddy current loss.

The iron loss is calculated by applying Equation (2) of iron loss calculation to the three parts, namely, stator yoke, stator teeth, and rotor core. In the case of the iron core, the stress changes due to thermal expansion; to take this into account, a thermal stress analysis was conducted in advance in order to

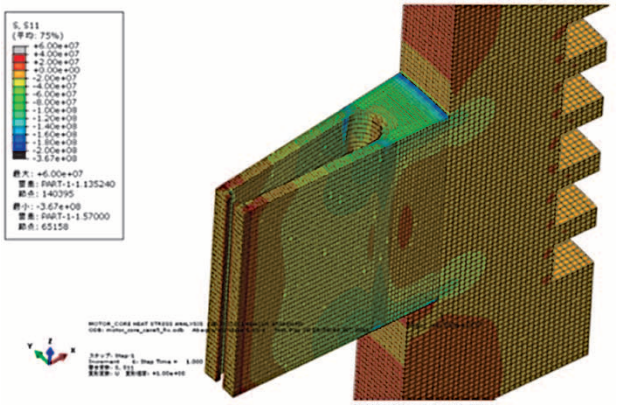

Fig. 3 Thermal stress distribution

understand the stress change and its distribution characteristics against temperature change (**Fig. 3**). Next, a calculation was performed to correct the stress value in accordance with the temperature change for the three divided parts, the yoke, teeth, and rotor.

2.2 Calculating copper loss of coil

The electric resistance of copper adopted to the coils of electric motors increases at a ratio of 0.39%/°C; hence the copper loss is calculated by Equation (3).

$$W_C = R_{20}\{1 + 0.0039(T-20)\}I^2 \quad \cdots\cdots\cdots\cdots\cdots\cdots \quad (3)$$

wherein W_C is the copper loss (W), R_{20} is the resistance (Ω) at 20°C, T is the coil temperature (°C), and I is the electric current (A).

2.3 Mechanical loss including bearing loss and windage loss

The bearing loss and amount of heat generation are calculated on the basis of formulae[6] published by a bearing manufacturer. The windage loss is calculated by the product of the circumferential velocity and the viscosity coefficient determined in accordance with the rotor surface area.

3. Heat-transfer calculation model for electric motor

3.1 Basic model for heat-transfer calculation

In this paper, Microsoft EXCEL is used as a platform for establishing the analysis environment to analyze various losses and distributions inside an electric motor computed by electromagnetic simulation, as well as the heat transfer state and the temperature distribution inside the electric motor with its losses as the sources of heat generation.

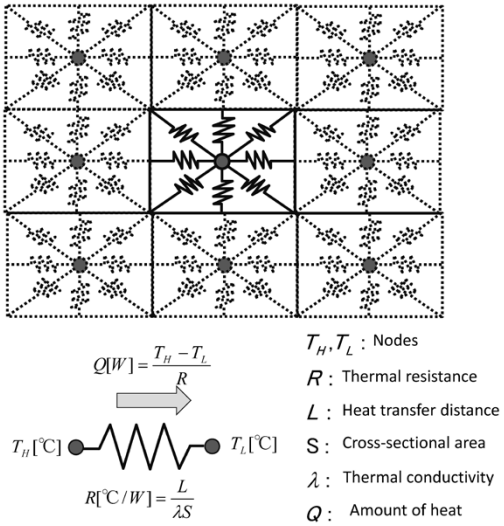

Fig. 4 Element model for heat transfer simulation

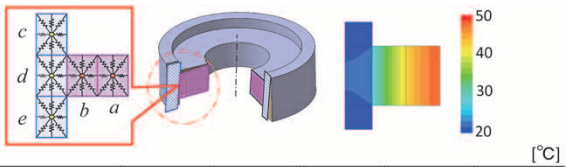

Temperature	T_a	T_b	T_c	T_d	T_e
Proposal simulation	42.4	31.3	20.4	21.9	20.4
FEM analysis	45.4	34.7	20.6	21.7	20.5
Difference	3.1	3.4	0.1	−0.2	0.1

※Each temperatures in this table are averages of each elements.

Fig. 5 Comparison of temperatures between proposed model and FEM analysis

Excel is suitable for preparing a process of describing an arithmetic expression in each cell to calculate the influence of adjacent cells. In the cases where shapes are changed frequently as in the case of electric motor designing, the software is convenient for easily coping with the changes in shapes and heat transfer circuits by copying and pasting cells. Therefore, a basic model of heat-transfer calculation was prepared, regarding each cell of Excel as a basic element of the heat transfer circuit (**Fig. 4**). In this figure, each rectangle is a basic element dividing the heat transfer circuit. Using the Excel cells for this rectangle enables the expression of the heat transfer characteristics between adjacent basic elements (cells). For the preliminary verification, thermal conduction was calculated for an assumed electric motor as shown in **Fig. 5**. For the calculation, a heat generation amount of 200 W was set for each coil-equivalent part (parts a, b), and the temperature of the circumferential surface of the hollow cylinder (parts c, d, and e; material, aluminum) was fixed at 20°C. Comparing the results of this calculation with those of the FEM analysis has confirmed that the difference is approximately 3°C.

3.2 Heat transfer model of coil part

As shown in **Fig. 6**, the coil part in the slot of an electric motor stator is composed of multiple materials such as copper wire, insulation coating, filler for the voids created by copper wire, insulation paper, air, and iron core. This analysis is devised to calculate this composite member structure as one member using the heat transfer model of Fig. 4 as the base. The equivalent thermal resistance in the axial direction of the electric-motor with this composite structure can be regarded as the synthetic resistance of each parallel circuit of the thermal resistance of the corresponding member; and the equivalent thermal conductivity, λ_H, in the axial direction of the electric motor can be calculated by Equations (4). On the other hand, the equivalent thermal resistance in the radial direction of the electric motor can be regarded as the synthetic resistance of the series circuit of the thermal resistance of each member, and the equivalent thermal conductivity, λ_L, of the electric motor in the radial direction can be calculated by Equations (5).

$$\begin{cases} \dfrac{1}{R_H} = \dfrac{1}{R_{H\_1}} + \dfrac{1}{R_{H\_2}} + \dfrac{1}{R_{H\_3}} + \dfrac{1}{R_{H\_4}} \\ R_H = \dfrac{H}{\lambda_H A_0},\ R_{H\_i} = \dfrac{H}{\lambda_i A_i}\ (i = 1, 2, 3, 4) \end{cases} \quad \cdots\cdots\cdots\cdots\ (4)$$

$$\begin{cases} R_L = R_{L\_1} + R_{L\_2} + R_{L\_3} + R_{L\_4} \\ R_L \fallingdotseq \dfrac{A_0}{\lambda_L HW^2},\ R_{L\_i} \fallingdotseq \dfrac{A_i}{\lambda_i HW^2}\ (i = 1, 2, 3, 4) \end{cases} \quad \cdots\cdots\cdots\ (5)$$

wherein

R_H: the equivalent thermal resistance in the axial direction of the coil composite structure,

R_{H_r}: the thermal resistance in the axial direction of each material in the coil composite structure,

R_L: the equivalent thermal resistance in the radial direction of the coil composite structure,

R_{L_r}: the thermal resistance in the radial direction of each material in the coil composite structure,

λ_H: the equivalent thermal conductivity in the axial direction of the coil composite structure,

λ_L: the equivalent thermal conductivity in the radial direction of the coil composite structure,

λ_i: the conductivity of each material in the coil composite structure,

A_0: the cross-sectional area of the coil composite structure,

A_i: the cross-sectional area of each material in the coil composite structure,

i= 1, for copper wire; = 2, for insulation coating; = 3, for copper wire; = 4, for voids.

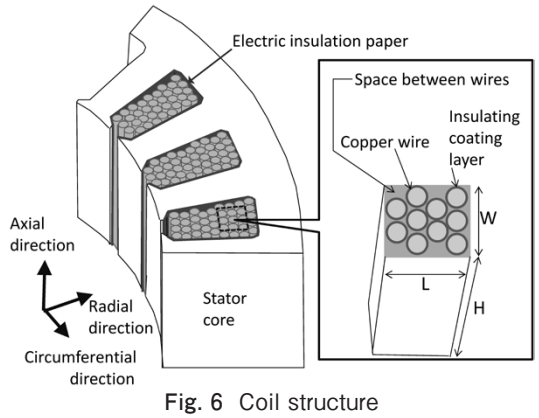

Fig. 6 Coil structure

Regarding the coil part of the electric motor as one member with different equivalent thermal conductivities λ_H and λ_L in the axial and the radial directions has simplified the heat-transfer calculation. It should be noted that, when each material itself has different thermal conductivities in the axial and the radial directions, the equivalent thermal conductivity must be calculated using the respective thermal conductivity.

3.3 Heat transfer model of bearing

In a bearing in its stopped state, heat is transferred from the outer surface on the high temperature side of each rolling body to the inside, and further to the surface on the low temperature side, causing a heat transfer between the inner ring and the outer ring. When a bearing is rolling, each part of the outer surface of the rolling body contacts the inner ring and the outer ring alternately, thus causing thermal conduction. Therefore, the heat transfer model in Fig. 4 was used as the base to prepare a model for thermal conduction, in which the heat accumulated on the outer surface of the rolling body is thermally conducted between the inner ring and the outer ring without being conducted through inside the rolling body (**Fig. 7**). The rolling body was simulated with 4 point elements on its surface, and 1 point element at its center, in which the four elements on the surface have thermal resistance on the sides of both the inner ring and outer ring; and the thermal resistance of the element in contact with the inner ring or the outer ring, depending on the rotation of the rolling body, is given a small thermal resistance value, while the thermal resistance of the element not in contact is switched to a large value, thereby enabling the calculation of the thermal conduction at the surface of the rolling body.

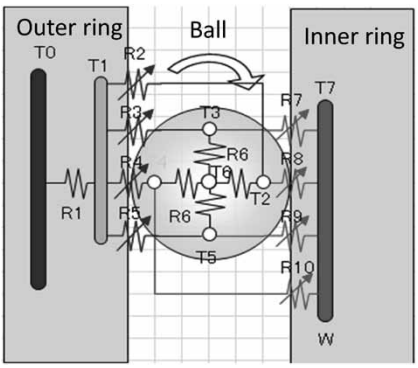

Fig. 7 Heat transfer model of ball bearing

4. Coupled simulation of electricity magnetism and heat transfer

In an electric motor, a part of the input power is consumed as a copper loss and/or iron loss. In particular, the iron loss consumes a part of the electric current to be converted to output torque, and an increase in iron loss causes a decrease in output torque. Therefore, it is necessary to increase the input electric current to output the target torque. In order to determine the substantially necessary input electric current considering the above, following the chart in Fig. 1, the magnetic flux and electric current in the electromagnetic circuit inside the electric motor are calculated, while the iron loss, copper loss, and bearing loss are calculated as above, to arrive at the output torque considering the influence of each loss. Then, the input electric current is increased for the decrease in the output torque with respect to the target torque by operating the input electric current control. These iterative calculations are repeated until the output torque is stabilized at the target value and the temperature of each part of the electric motor is also stabilized. The results of this calculation allow the prediction of how the heat generated by iron loss, copper loss, and mechanical loss, occurring in each part of the electric motor, is transferred to the cooling section of the electric motor housing via the heat transfer route of the structural members of the electric motor and the air layer in its inner space. As a result, it is possible to optimally design the electromagnetic circuit and heat transfer circuit that meets the target output performance and target temperature of an electric motor. This coupled simulation environment has been used to design a small electric motor with high output for a hybrid excavator. Furthermore, after simulation confirmed that the target performance is achievable, an electric motor was prototyped to verify the output performance, efficiency, and feasibility of heat balance.

The coupled simulation constructed this time

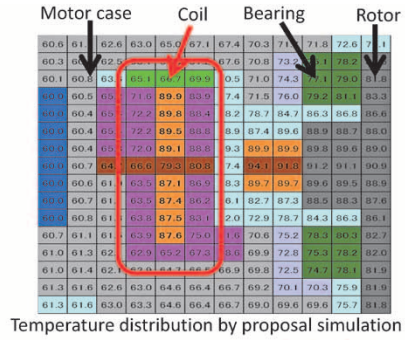

Temperature distribution by proposal simulation

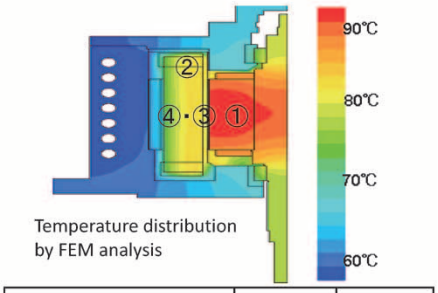

Temperature distribution by FEM analysis

	Proposal simulation	FEM
①Rotor [℃]	93.0	92.0
②Coil end[℃]	89.9	84.7
③Coil in slot[℃]	85.7	80.7
④Teeth[℃]	80.8	83.9

Fig. 8 Comparison of heat transfer between proposed simulation and FEM analysis

was used to calculate the internal temperature distribution at the rated output of the slewing electric motor that was designed. **Fig. 8** shows the results of the computation. For comparison, FEM analysis was also carried out to confirm validity.

The efficiency distribution calculation results of all output region will be described in the next section.

5. Performance evaluation of electric motor design

Due to space limitations, this paper reports only the evaluation results for the slewing electric motor prototyped. An electric motor designed to have the performance confirmed by the simulation described above was prototyped (**Fig. 9**). Heat balance testing for verification by comparison with the analysis result of Fig. 8 and the efficiency distribution measurement in the whole output range were carried out on a motor bench apparatus.

A heat balance test was carried out at a rated output condition, and the results show that the temperature distribution inside the electric motor tends to be approximated to the analysis, although the in-slot coil temperature became 10 to 13°C higher than the analysis results (**Fig.10**). Moreover, there is a good agreement between the analysis results of efficiency distribution for the entire output range

Fig. 9 Prototyped motor of slewing motion

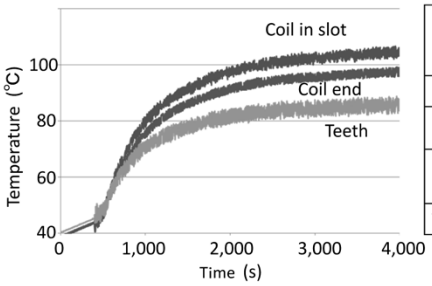

	Temperature on rated output
Rotor	90.0
Coil end	98.0
Coil in Slot	103.0
Teeth	86.0

Fig.10 Experimental results of heat balance of prototyped electric motor

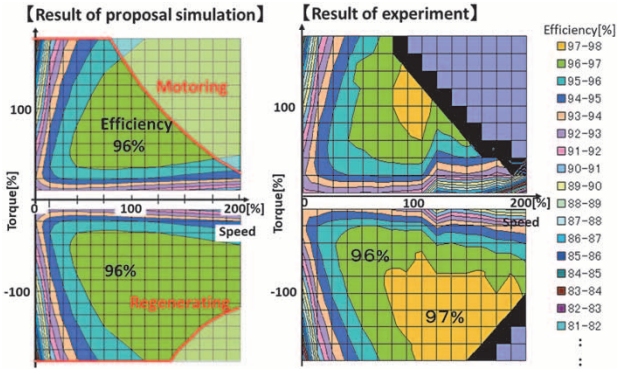

Fig.11 Comparison of efficiency distribution of prototyped motor between simulation and experimental results

and experimental results (**Fig.11**), confirming that the highest efficiency can be predicted.

Conclusions

This paper has focused on the issues of heat generation, heat extraction and heat transfer, which poses problems in the designing of a compact electric motor with high output and torque, and introduced a coupled analysis technology for electricity magnetism and heat transfer, the technology established to find the structural design for removing heat generated inside a motor to the outside with a minimum heat transfer and radiation area. This technology has led to the successful development of a small, high-output slewing electric motor for hybrid excavator and a flat high-torque generator motor.

There still will be a need for further performance upgrading of electric motors and lead-time reduction of the development. We will strive to advance the development of analytical prediction technologies.

References

1) D. Ebihara . *Mōta gijutsu jitsuyō handobukku 1st edition*. 2001, p.419, p.692.
2) J. Magn. *Sec. Jpn*. 2006, Vol.30, pp.196-200.
3) J. Toda el al. *JFE Technical Report*. 2015, No.36, pp.24-31.
4) Y. Takeda el al. *Umekomi jishaku dōki mōta no sekkei to seigyo 1st edition*. Ohmsha, 2001, p.17, pp.74-84.
5) K. Narita. *JMAG Newsletter*. January 2014, pp.37-41.
6) *Roller bearing general catalog (Cat. No.2202/J)*. NTN Corporation, p.A-71.

Disturbance Rejection Filter for Depth Sensor

Masashi HAMAGUCHI*1, Dr. Takashi HIEKATA*2

*1 Applied Physics Research Laboratory, Technical Development Group
*2 General Administration Department, Technical Development Group

In recent years, data obtained from sensors attached to excavators are being widely used in assisting the operators. The processing unit logic of such a sensor system has been developed to ensure flexibility in the design of the sensor system. As a part of this development, an effort has been made to solve the problem of detecting disturbances, such as rain, snow, and insects, when the depth sensor is used for outdoor measurements. An object placed in front of a depth sensor in a raining environment was moved back and forth while continuously measuring the appearance of the object. In the measured data, points with possible disturbances were chosen. The speed, direction, and acceleration between frames were calculated as feature quantities, which led to the development of a disturbance rejection filter that eliminates the points above set thresholds. This filter has been confirmed to detect the position of objects while ignoring the influence of rain in real applications.

Introduction

Recently, data obtained from sensors are being widely used in assisting operators. For example, a system has been developed having a monitoring camera attached to the rear of an excavator to display the backside image, and thus to warn the operator when surrounding objects or people approach.[1] Also, a system has been developed that uses 3D point cloud data acquired with a camera sensor to perceive the current status of a construction site in a short time.[2]

The sensor systems adopted to these applications are often made by specialized sensor manufacturers with their original know-how. Relying on another company for a sensor system may result in its detection unit and processing unit being integrated into a black box (**Fig. 1**), making it difficult to change the sensor, or to add functions to the processing section as needed. This leads to increased development period and development cost.

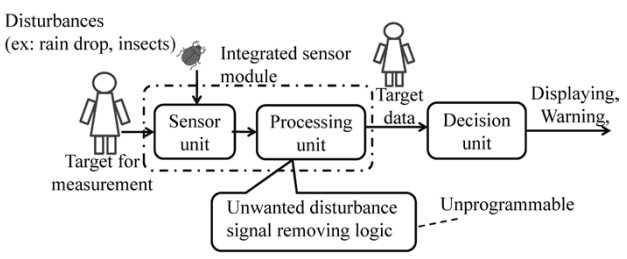

Fig. 1 Components of sensor system

In order to solve the above problems, a processor logic has been developed in-house while using general purpose products for the sensors. This paper relates to a distance sensor attached to an excavator to detect objects approaching the excavator in outdoors. This report describes a newly developed technique for eliminating disturbances caused by rain, snow, insects, etc.

1. Sensors used for excavators

Japan Construction Machinery and Construction Association Standard[3] lists laser sensors, ultrasonic sensors, and ultrasonic transponders for danger detection, along with closed circuit televisions and the like for blind-spot assistance, and defines their test methods and standard performance requirements.

These sensors are attached to an excavator to make measurements in the area surrounding it, to perceive the status of work, assist operation, and detect/give a warning when approaching objects. An excavator must be capable of measuring the distance to each object; hence, distance sensors are used for this purpose.

Laser sensors and ultrasonic sensors are most commonly used for distance measurement. A laser sensor is superior in accuracy and responsivity thanks to the high speed of light waves; however, it has a risk of malfunctioning when refraction occurs due to water wetting or smearing on its emission port. An ultrasonic sensor is superior in environmental resistance thanks to the characteristics of sound waves, which are less prone to refraction even in the rain, or dust and the like; however, its resolution is poor due to the low propagation speed and low frequency of sound waves, causing errors of centimeter order in distance measurement. Assisting excavator operators in perceiving the surrounding area requires high measurement accuracy over a wide range of subjects. Therefore, the depth image sensor described in this paper employs a laser type that can two-dimensionally measure the distance to each object.

2. Influence of disturbance on sensors

When a depth image sensor is used outdoors, there is a risk that the distance to the measurement object cannot be measured correctly due to rain, snow, insects, or the like. Therefore, this study investigated the influence of rain on the measurement results of the depth image sensor. An object (approximately 75 cm square) was placed in front of a depth sensor in a raining environment as a detection target and was moved back and forth manually for two rounds (**Fig. 2**). The motion of the object was captured by a depth image sensor that can measure continuously at a rate of several tens of frames per second. The two-dimensional distance data obtained was used to detect the most proximal distance between the sensor and object.

Fig. 3 shows the detection results of object positions. The vertical axis shows the most proximal distance, and the horizontal axis shows the elapsed measurement time. This figure shows the most proximal distance measured and the median value of the most proximal distances measured in the last 3 frames.

The graph of the detection results is supposed to have a shape such as that shown in **Fig. 4** with two gentle peaks indicating the two rounds of back and forth movements. The detection results in Fig. 3, however, indicate that the sensor reacts to the laser

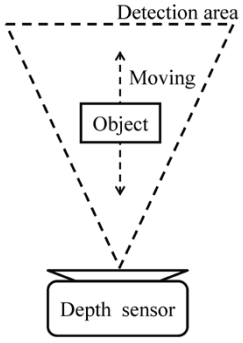

Fig. 2 Equipment layout for experiment

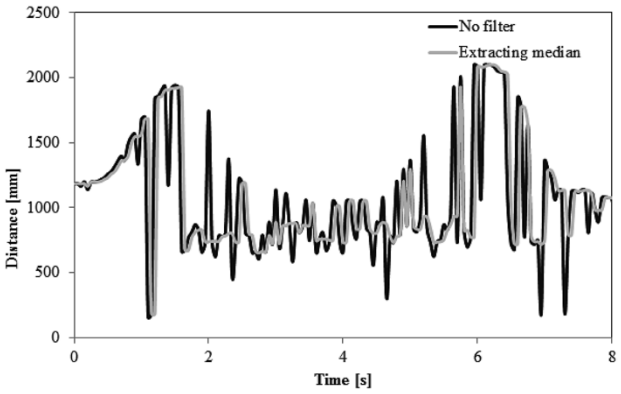

Fig. 3 Detection of object position

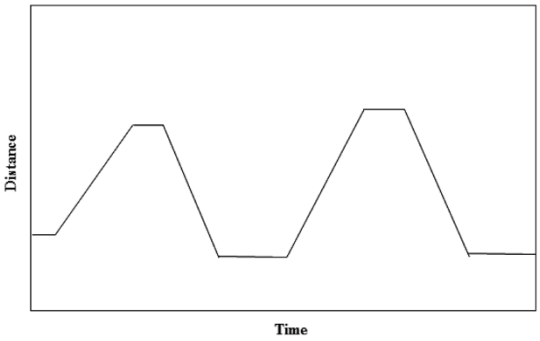

Fig. 4 Image of object position change

reflection on raindrops, and the detected position changes greatly in a short time. In addition, even when the median value of the last 3 frames was adapted to the processing, the detected positions still changed greatly in a short time, indicating that the influence of rain could not be removed. Since it was envisaged that other flying objects such as snow and insects would cause similar effects, a study was conducted on a filter for removing these disturbances.

3. Development of disturbance rejection filter

To develop a filter that rejects disturbances caused by rain, snow, insects, etc., a study was conducted on a technique that comprises extracting multiple points including the detection target as disturbance candidates for each frame, calculating velocity, direction and acceleration as feature quantities on the basis of the distance traveled in the preceding frames, and determining the point exceeding the numerical value that can be taken by the detection target as disturbance.

The basic flow chart of this technique is shown in **Fig. 5**. First, a distance image is acquired from the depth image sensor, and an initial filter (such as a smoothing filter for noise rejection) is applied to the distance image obtained. After that, the point which is most proximal to the sensor is sought in the distance image and taken as one of the disturbance candidates. In order to extract a plurality of disturbance candidates, circular ranges, each with a predetermined radius r and centered at respective points found previously, are rejected from the search range in the distance image. After this, the most proximal points are sought again. These operations are repeated for a predetermined number of times to extract disturbance candidate points. They are also performed for all the measured frames.

Next, disturbance candidate points are associated time-wise. An example of the association of disturbance candidate points is shown in **Fig. 6**. For each disturbance candidate point $p1(n)$ at a

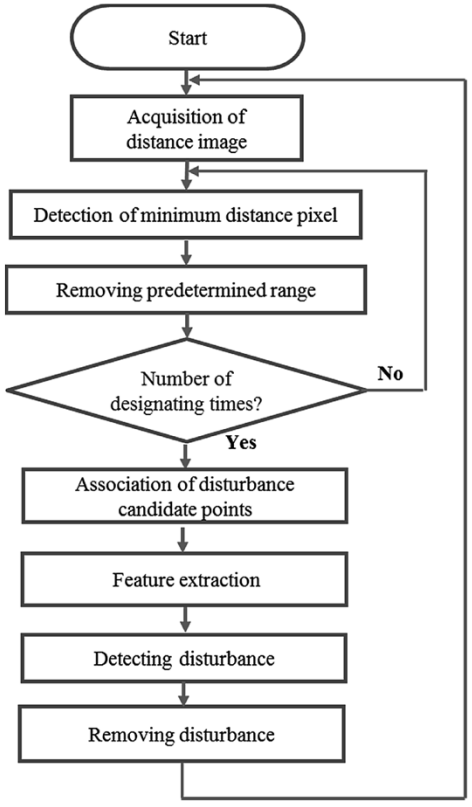

Fig. 5 Flowchart of disturbance rejection filter

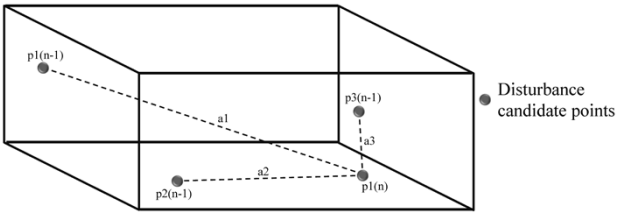

Fig. 6 Association of disturbance candidate points

certain time, *n*, the distance from the disturbance candidate point of the immediately preceding frame is calculated, and this is carried out for all the combinations. Here, the point that gives the shortest travel distance is regarded as the same point in the immediately preceding frame and is associated time-wise. In Fig. 6, there are three disturbance candidate points in the immediately preceding frame *n-1;* namely, *p1*(*n-1*), *p2*(*n-1*), and *p3*(*n-1*), and the travel distances are expressed as *a1*, *a2*, and *a3*, respectively. Here, it is assumed that *a1>a2>a3*. At this time, the shortest travel distance is given by *a3*, and thus the same point in the immediately preceding frame of the disturbance candidate point *p1(n)* is associated time-wise with *p3(n-1)*.

After the time-wise association of the disturbance candidate points is performed as described above, the speed, angle, and acceleration are calculated as feature quantities for determining the existence of a disturbance. When the disturbance candidate points

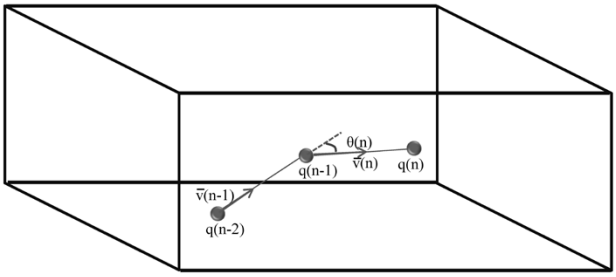

Fig. 7 Position of disturbance candidate points

are positioned as in **Fig. 7** and the candidate points of each frame are associated time-wise with *q(n)*, *q(n-1)*, and *q(n-2)*, the velocity vector, $\bar{v}$, is calculated by Equation (1) and Equation (2).

$$\bar{v}(\mathrm{n}) = (q(n)\text{-}q(n\text{-}1))/\Delta t \quad \cdots\cdots (1)$$

$$\bar{v}(\mathrm{n}\text{-}1) = (q(n\text{-}1)\text{-}q(n\text{-}2))/\Delta t \quad \cdots\cdots (2),$$

wherein Δt is the time length between the frames.

Subsequently, the angle θ of the velocity vector between the frames is calculated by Equation (3).

$$\theta(\mathrm{n}) = \angle(\bar{v}(\mathrm{n}), \bar{v}(\mathrm{n}\text{-}1)) \quad \cdots\cdots (3)$$

Further, the acceleration vector, $\bar{a}$, is calculated by Equation (4).

$$\bar{a}(\mathrm{n}) = (\bar{v}(\mathrm{n})\text{-}\bar{v}(\mathrm{n}\text{-}1))/\Delta t \quad \cdots\cdots (4)$$

A disturbance is judged to exist when any one of the results of calculating Equations (1) to (4) exceeds the set threshold. It should be noted that the velocity vector and the acceleration vector are determined by absolute values.

The points judged to be disturbances by the disturbance rejection filter described above are excluded from the distance measurement on the distance image to prevent erroneous detection.

4. Verifying effects of disturbance rejection filter

The most proximal points were extracted from the results of the test performed in Section 2, in which the disturbance rejection filter described in Section 3 was applied, and the results are shown in **Fig. 8**. Here, the search range exclusion radius of each disturbance candidate was *r*=150 mm, the number of extraction times for each disturbance candidate was 10, and the thresholds for the judgement of a disturbance are set at 5 m/s for the speed, 3 m/s^2 for the acceleration, and 90 degrees for the angle. The time interval between the frames was set at 50 ms. For the setting of each threshold, reference was made to the falling velocity of 6.5 m/s for a raindrop with a standard size (diameter 2 mm)[4] and the acceleration of approximately 4.8 m/s^2,

which is the minimum value of the acceleration measured for an insect (fly),[5] to set respective values lower than these. For the angle, there was no suitable data, and a numerical value was provisionally determined.

The results of the position detection of the object exhibit a graph clearly showing the back and forth motion of the object for two rounds, showing that the influence of disturbances is rejected to allow the position detection of the detection target.

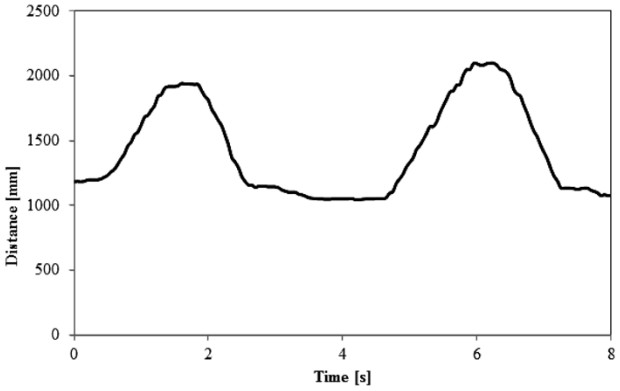

Fig. 8 Detection of object position through disturbance rejection filter

Conclusions

A filter to reject the influence of disturbances such as rain and snow has been developed for a sensor installed on an excavator and used for acquiring information on the surrounding area in an outdoor environment. This filter is configured to judge and reject disturbances, using the velocity, acceleration, and angle of disturbance candidate points in measurement frames, and its ability to detect the positions of objects even in the rain has been confirmed. In the future, this technique will be used for sensors to acquire distance information in the surrounding area, which will lead to the new functional development of excavators.

References

1) N. Mitsuyanagi. *Kensetsu no sekō kikaku*. 2009, No. 709, pp. 52-57.
2) C. Shike el al. *Komatsu technical report*. 2015, Vol. 61, No.168, pp. 2-6.
3) *Japan Construction Machinery and Construction Association Standard*. JCMAS H017, 2003.
4) M. Kumai el al. *Journal of the Meteorological Society of Japan*. 1954, Vol. 32, No. 3, pp. 69-76.
5) R. P. Ray el al. *Nature Communications*. 2016 Vol. 7, No. 10851.

Development of 20-tonne Class Hybrid Excavator, SK200H-10

Yoichiro YAMAZAKI*1, Seiji SAIKI*1, Nobuhiro KOGA*2, Akira TSUTSUI*3, Kazuhide SEKIYAMA*4, Kengo MAEDA*5

*1 Advanced Technology Department, Design & Development Engineering Division, Global Engineering Center (GEC), KOBELCO CONSTRUCTION MACHINERY CO.,LTD.
*2 Hydraulic Excavator Engineering Department, Design and Development Engineering Division, Global Engineering Center (GEC), KOBELCO CONSTRUCTION MACHINERY CO.,LTD.
*3 Applied Physics Research Laboratory, Technical Development Group
*4 Mechanical Engineering Research Laboratory, Technical Development Group
*5 Research and Development Planning Department, Head Office

Power electronics technology continues to evolve, particularly in the automobile industry, with the aim of reducing fuel consumption and the environmental burden. This technology was adapted for a hybrid hydraulic excavator, the SK200H-10, equipped with a lithium-ion battery, as introduced in this paper. A continuous engine assist has been realized for the hydraulic excavator by effectively using the regenerative energy generated during slewing deceleration, due to the large inertia of its slewing body, and by adopting a lithium-ion battery with high output and large capacity. As a result, the fuel consumption of the excavator has been reduced significantly. The scrap handling machine (with magnet), the SK210DLC-10, has the same generator motor as SK200H-10 and applies a hydraulic excavator with a totally new power generation system, which was formerly based on a hydraulic pump. This machine enjoys a remarkably increased magnetic attraction and considerably reduced fuel consumption, thanks to the reduced energy loss during power conversion.

Introduction

The reductions of greenhouse gases that cause global warming, including CO_2, as well as the reduction of nitrogen oxides (NOx) causing air pollution and health damage, are major issues for the international community as a whole. These issues are characterized by the slogans of "ecology" and "sustainable society."

The greatest number of construction machinery units in operation are hydraulic excavators, and energy conservation and reduction of the environmental burden are their major challenges. In response, hybrid hydraulic excavators exploiting power electronics technology have recently been commercialized.

This paper summarizes the hybrid hydraulic excavator, the SK200H-10,[1)] which is equipped with a lithium-ion battery that is being used for hybrid electric vehicles (HV) and electric vehicles (EV) to further reduce fuel consumption and the environmental burden. This paper also introduces the SK210DLC-10, a scrap-handling machine with a magnet (hereinafter referred to as a "lifting magnet excavator"), which adopts the same generator motor as the SK200H-10 and has a renewed power generation system, which has conventionally been driven by a hydraulic pump.

1. Efforts to reduce fuel consumption of hydraulic excavators

A hydraulic excavator repeats high-load tasks such as digging and low-load tasks such as leveling in a short time and thus is subjected to a great fluctuation of the load. The flow of energy in a hydraulic excavator is shown in **Fig. 1**. This figure shows the energy loss at each part of the hydraulic excavator, assuming the combustion energy to be 100%. A hydraulic excavator supplies power that can handle the maximum load from its engine. However, the energy loss in each part is approximately 55% for the engine, approximately 15% for the hydraulic pump, approximately 20% for the hydraulic control system and approximately 1% for the mechanical transmission elements. As a result, the final effective output is only approximately 9% of the combustion energy.

On the basis of the above, various improvements have been made for hydraulic excavators to reduce these energy losses. For the fuel combustion of the engine, where the loss is the greatest, the combustion efficiency has been improved by increasing the fuel injection pressure through, among other means, the common-rail system. Furthermore, the combustion efficiency is improved by, for example, adopting the variable nozzle VG turbo (**Fig. 2**) so that the amount of intake air can be adjusted by the opening of the exhaust side nozzle. For the hydraulic control system, where the loss is the second greatest after

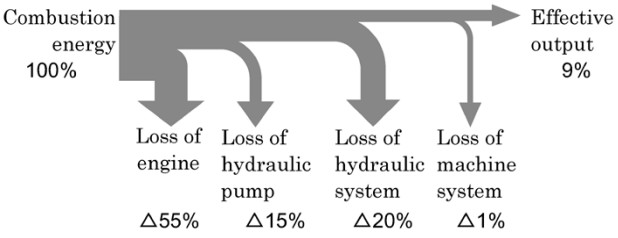

Fig. 1 Energy flow of hydraulic excavator

the engine, the efficiency has been improved by such means as reducing the pressure loss in hydraulic devices and hydraulic piping, and by hydraulic regeneration circuits that utilize the mass of the attachment on the hydraulic excavator (**Fig. 3**).

These efficiency improvement technologies have been adopted to conventional hydraulic excavators. The following section introduces the hybrid technology applied to SK200H-10 (**Fig. 4**).

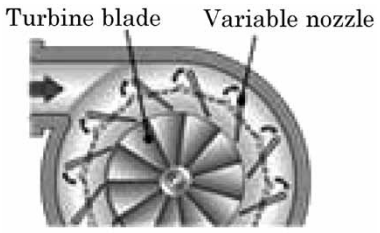

Fig. 2 Variable nozzle VG turbo

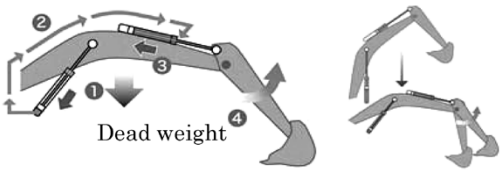

①Boom cylinders are contracted by its dead weight.
②High-pressure oil supplied to arm cylinder.
③Arm cylinders are contracted.
④Arm moves forward.

Fig. 3 Hydraulic regenerative circuit

Fig. 4 Overview of SK200H-10

2. Outline of hybrid system

Fig. 5 shows the constitution of the hybrid system for the SK200H-10. In this system, the hydraulic pump is driven by both the engine and the generator motor directly connected to it. In addition, the actuator for slewing the machine body is electrically driven and separated from the hydraulic circuit. Furthermore, the regenerative energy of slewing deceleration is converted into electrical energy.

Kobelco Construction Machinery Co., Ltd. (hereinafter referred to as "the Company") has released hybrid hydraulic excavators, including the SK80H, in 2009 and the SK200H-9 in 2012. The SK200H-10 has adopted a generator motor to continuously support the engine and, at the same time, utilized for the first time a large-capacity lithium-ion battery with high output in order to accelerate and decelerate the excavator's slewing body with a large inertial mass. The hybridization has significantly improved its environmental performance.

3. Outline of hybrid devices

We developed the main devices mounted on the SK200H-10 (**Fig. 6**) with the aim of making the vehicle size and layout common with those of the standard hydraulic excavators, pursuing energy saving performance, and maximizing the work capacity. To this end, we decided to start development from scratch and to manufacture the generator motor, slewing electric motor, and lithium-ion battery unit in-house.

In particular, all the devices adopt liquid cooling systems in order to achieve compactness and high output. For the lithium-ion battery, a heating system and protection system compliant with the standards for electrically-powered automobiles were adopted to cope with harsh working conditions and a natural

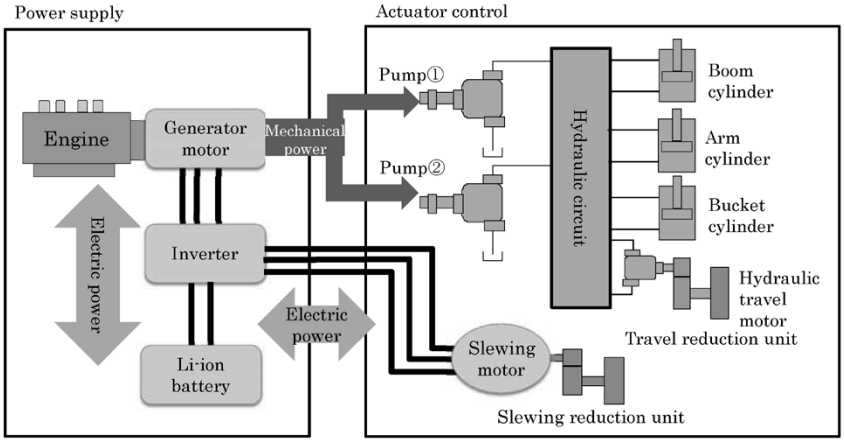

Fig. 5 Constitution of hybrid system

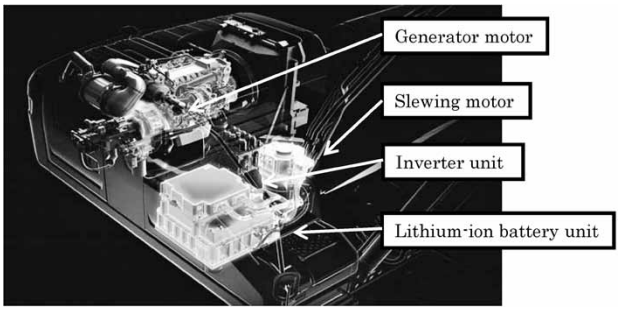

Fig. 6 Overview of main hybrid device

environment. An outline follows.

3.1 Generator motor

In order to give the body the same width as that of the standard hydraulic excavator, a flat-type water-cooled generator motor with an axial direction dimension (total length) of approximately 140 mm was newly developed so as to fit between the engine and hydraulic pump. A permanent-magnet three-phase synchronous AC motor was adapted to enable engine assist, which is effective in reducing fuel consumption. This motor has the further capability of generating power high enough to charge the large-capacity lithium-ion battery and to accelerate the slewing electric motor.

3.2 Slewing electric motor

A water-cooled slewing electric motor was newly developed to ensure a mountability comparable to that of the conventional hydraulic motor, and to realize a machine-body slewing performance equivalent to that of the standard hydraulic excavator. A permanent-magnet three-phase synchronous AC motor was adopted as a vertical high-speed motor to allow its direct connection to the slewing reduction gears. This has enabled the energy generated during slewing deceleration to be efficiently regenerated, while realizing smooth and powerful slewing acceleration characteristics.

3.3 Inverter unit

In order to secure mountability to the machine body, the slewing motor inverter and generator motor inverter were integrated into a newly developed, small water-cooled inverter unit. This inverter unit was linked with the controllers for the hydraulic devices and engine in order to control the entire hybrid system, including the control for generator-motor/slewing-motor and the charge-discharge control of the lithium-ion battery, to realize a remarkable reduction in fuel consumption.

3.4 Lithium-ion battery unit

Since the operating temperature range of a lithium-ion battery is limited, it is housed in a protective casing having a cooling function and warming function. The unit comprises a function that detects leaks and automatically shuts off power, as well as a manual shut-off switch, to prevent any direct/indirect electric shock caused by the lithium-ion battery, not to mention its compliance with the United Nations Recommendations on the Transport of Dangerous Goods.

4. Features of SK200H-10

4.1 Energy saving effect and work volume

The SK200H-10 adopts a high-output, large-capacity, lithium-ion battery. This has enabled the engine assist of the generator motor and effective use of regenerative energy of slewing deceleration while greatly reducing the fuel consumption and increasing the work volume. **Fig. 7** shows the measurement results for fuel consumption (fuel consumption per hour) during the digging/loading operation. The SK200H-10 exhibits a fuel consumption that is 17% less than that of the conventional hydraulic excavator and 12% lower than that of the SK200H-9. **Fig. 8** compares the work volume (the amount of material carried per hour) with that of the conventional hybrid machine. This figure indicates the difference for each working

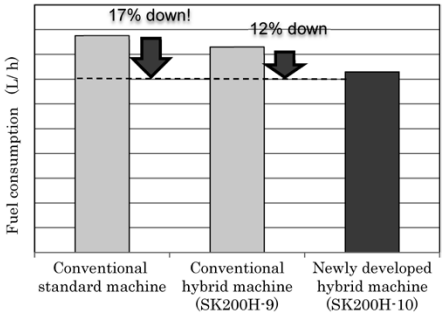

Fig. 7 Comparison of fuel consumption under same workload

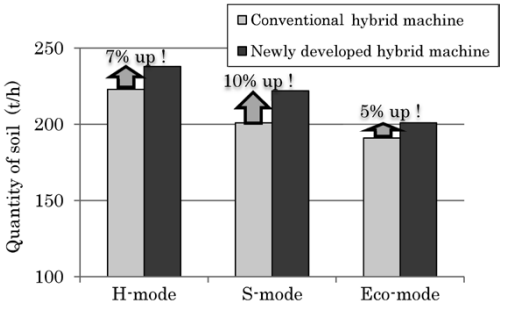

Fig. 8 Comparison of work volume between conventional and newly developed hybrid machines

mode, showing a 7% to 10% increase in work volume for all the modes. The increase in work volume is attributable to the improvement of work performance described below. It should be noted that this measurement was carried out on the basis of the Company's own standards and the work modes are a heavy work mode (H-mode), a normal work mode (S-mode), and an energy-saving mode (Eco-mode).

4.2 Improvement of work performance

In the Company's hybrid system, the actuator driving the slewing body with a large inertial mass is fully motorized and separated from the hydraulic circuit, which has eliminated hydraulic interference during combined operations of attachment and travelling. Furthermore, in the SK200H-10, the combination of a large capacity lithium-ion battery and a slewing electric motor has greatly increased the acceleration energy of slewing, achieving operability that is smoother and more powerful than that of the conventional machines.

The work performance of the SK200H-10 is suitable not only for civil engineering works in Japan, but also supports various work types and area characteristics, including Europe, where rotary tilt buckets (**Fig. 9**) are heavily used, and North America, where work volume with large buckets is emphasized. Thanks to this, it has a successful reputation among customers around the world.

Fig. 9 Overview of SK200H-10 equipped with tilt bucket

5. Development of SK210DLC-10

5.1 New lifting magnet excavator

The SK210DLC-10 scrap handling machine with magnet (lifting magnet excavator), which is developed based on a hydraulic excavator, adopts the same generator motor as that of the SK200H-10 to renew its power generation system which had been driven by a hydraulic pump. **Fig.10** shows the system configuration diagram of the new lifting magnet excavator and **Fig.11** shows its appearance.

5.2 Increased magnetic attraction and energy saving effect

Reducing the energy loss at the time of power conversion has greatly increased the magnetic attraction and significantly reduced the fuel consumption. As shown in **Fig.12**, the power conversion loss has been improved, going from 57% to 14%. This is an effect of changing the power generation, which was accomplished with a hydraulic pump in a system using a generator

Fig.11 Overview of scrap handling machine with new-type magnet

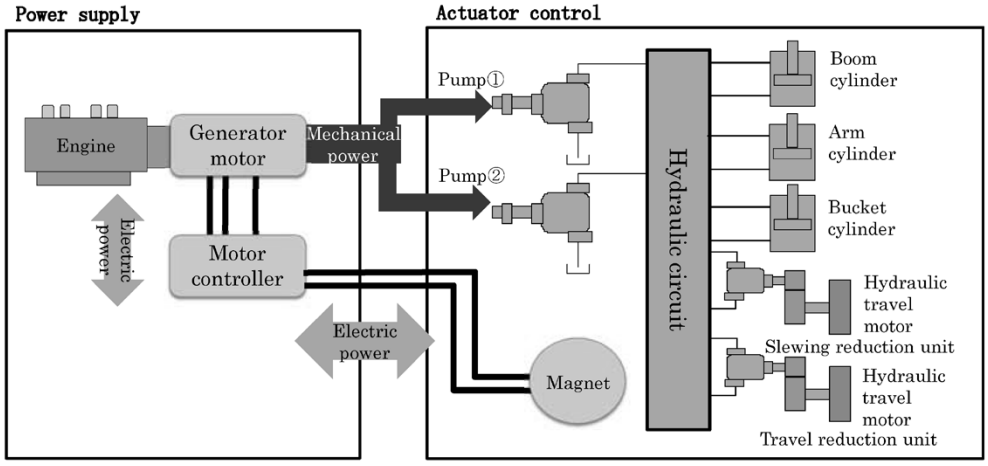

Fig.10 System constitution of scrap handling machine with new-type magnet

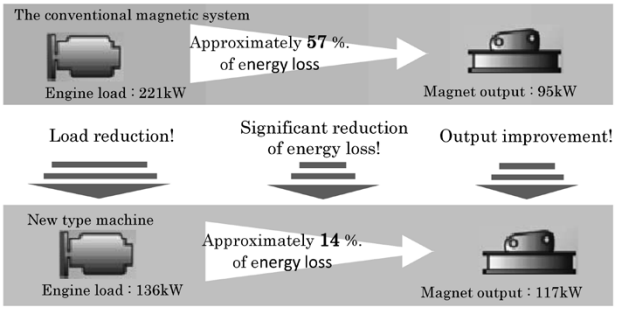

Fig.12 Power conversion efficiency

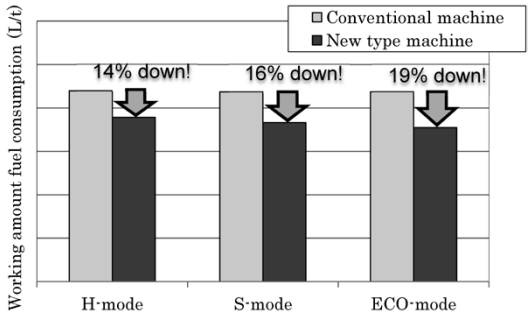

Fig.13 Comparison of work volume fuel consumption

motor that is disposed in series between the engine and hydraulic pump. **Fig.13** compares the work volume fuel consumption (fuel consumption per tonne of transported sediment) of the various working modes, measured in accordance with our own standard. Here, the differences among the working modes are shown, and the work volume fuel economy has been improved by 14% to 19% in all the modes. This is attributable not only to the improved power conversion efficiency, but also to the increased attraction of the magnet.

5.3 Improvement of visibility and maintainability

In parallel with the simplification of the system, the control panel, which was placed on the right front of the conventional machine body, was housed in a guard, thereby simplifying that side of the machine body. As a result, the visibility for the operator and accessibility to the upper surface of the machine body during maintenance has been greatly improved (**Fig.14**).

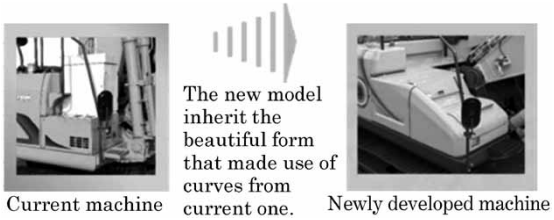

Fig.14 Comparison of appearance of right front spaces in conventional and newly developed machines

6. Utilization of IT data

In recent construction machinery, including hydraulic excavators, there has been an upsurge in the installation of communication devices and utilization of IT data. The SK200H-10 and SK210DLC-10 are also equipped with functions to closely monitor the operating state of their electric motors, inverters, lithium-ion batteries, including the electric motor output, system voltage, and temperature of the main devices for the hybrid system and the magnet power generation control system, in addition to the operating status of the hydraulic system and engine. Furthermore, the monitoring data on the machine side is statistically processed by a cloud server to detect any signs of abnormality, thus enhancing the preventive maintenance and maintenance services (**Fig.15**).

Moreover, operational information such as the daily fuel economy and work volume is offered to customers to be utilized in their machine operation management and operation planning.

Conclusions

This paper has introduced the SK200H-10 equipped with a lithium-ion battery and the SH210DLC-10 with a renewed power generation system as examples of efforts to reduce the CO_2 footprint and fuel consumption of hydraulic excavators.

The hybrid excavator has realized the effective use of the regenerative energy generated when the large inertial mass of the slewing body decelerates. In addition, a high output/large capacity lithium-ion battery has been adopted, enabling a sustainable

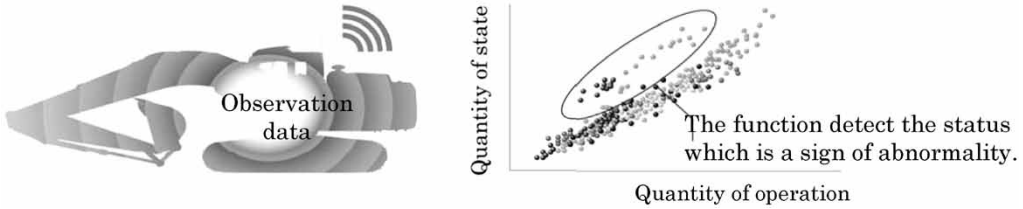

Fig.15 State observation function using IT measurement data

engine assist, and achieving a significant reduction in fuel consumption.

In the lifting magnet excavator, reducing the energy loss during power conversion has greatly increased the magnet attraction while greatly reducing the fuel consumption.

It is envisaged that the development of new technology for zero emissions will be accelerated, led by the automobile industry. We will strive to introduce these technologies in the construction machinery represented by hydraulic excavators to further decrease fuel consumption and reduce the environmental burden.

References

1) S. Saeki. *Journal of JCMA. 2017*, Vol.69, No.1, pp.35-38.

Evolution and Development of iNDr

Kazuhiro UEDA*1, Tomoyuki TSUCHIHASHI*2, Hajime NAKASHIMA*3, Zenzo YAMAGUCHI*4, Kyoko MASUDA*5, Satoshi TABUCHI*5

*1 Advanced Technology Department, Design & Development Engineering Division, Global Engineering Center(GEC), KOBELCO CONSTRUCTION MACHINERY CO.,LTD.
*2 Hydraulic Excavator Engineering Department, Design & Development Engineering Division, Global Engineering Center(GEC), KOBELCO CONSTRUCTION MACHINERY CO.,LTD.
*3 ICT Promotion Department, KOBELCO CONSTRUCTION MACHINERY CO.,LTD.
*4 KOBELCO MACHINERY EUROPE GmbH.
*5 Mechanical Engineering Research Laboratory, Technical Development Group, Kobe Steel, LTD.

Integrated Noise & Dust Reduction (iNDr) is an advanced proprietary cooling system with the two unique functions of noise reduction and dust removal. It is installed in an ultra-low-noise hydraulic excavator launched for the first time in 2007. With its extremely low noise and dust-proof performance, it is used preferentially at many sites. Rather than becoming obsolete, it has gained in popularity, thanks to its performance. Environmental regulations are becoming increasingly stringent, and the constraints on equipment have become increasingly severe in connection with the development of smaller models: for example, the addition of a new function, mixing cooling exhaust and engine exhaust, is now required. Due to these circumstances, design tools based on fundamental theories, which allow more efficient study, are being utilized to evolve the iNDr into a "cross-over duct" with a new structure, while maintaining its extremely low-noise performance.

Introduction

In July 2007, Kobelco Construction Machinery Co., Ltd (hereinafter referred to as the "Company") launched an extremely low-noise-type hydraulic excavator equipped with an integrated noise & dust reduction cooling system (iNDr). The iNDr is a state-of-the-art cooling system uniquely developed by the Company. It combines the two functions of soundproofing and dust removal, contributing to the significant reduction of noise in the surrounding area, while dramatically improving the maintainability of cooling devices such as radiators. With its remarkable, extremely-low noise performance and dustproof performance, it has gradually penetrated the market since its launch. Its extremely low noise performance has been highly evaluated, mainly by general civil engineering customers, and its dustproof performance has been highly evaluated by industrial waste and forestry customers. Meanwhile, the environmental regulations imposed on engines have been strengthened all over the world. The noise regulations that had been enforced in Japan and Europe were also enforced in China in 2012, and three years later, in 2015, the regulation value was further strengthened by 3 dB.

It was against this backdrop that the iNDr technology, which had originally been established for urban-type, general-purpose, heavy equipment excavators, was adapted for mini-excavators, which, among all the types of excavators, are more often used near residential areas. This new iNDr was launched into the market.

In addition, the conventional iNDr for urban-type, general-purpose, heavy equipment excavators has been improved to keep up with engine emission regulations, which are being strengthened step-by-step, while maintaining its extremely low noise, dustproof performance. However, postprocessing apparatuses for exhaust emissions are required to comply with the 4th regulation for engine exhaust emissions. This has imposed extremely severe mounting conditions, making it difficult to arrange the sound absorbing duct that characterizes the iNDr, for example. Hence, a sound-absorbing exhaust duct was newly developed to achieve extremely low noise performance equivalent to that of the conventional machine.

This paper introduces the adoption of iNDr in mini-excavators and the evolution of iNDr associated with compliance with the engine emissions regulations for heavy equipment excavators.

1. Adoption of iNDr in mini-excavators

1.1 Features and challenges for mini-excavators

Mini-excavators belong to a class of excavators whose total body weight is 5 tonne or less, and have been designed differently from heavy equipment excavators because of their machine body structures. Therefore, in order to adapt the iNDr developed for heavy equipment excavators to mini-excavators, it was necessary to review the basic design of mini-excavators and make it as close as possible to that of heavy equipment excavators.

One major difference exists in the cooling systems for engine and hydraulic devices, as seen in the positional relation of the heat exchanger

elements such as the cooling fan, driven by the engine, and the radiator that passes the cooling air. A heavy equipment excavator employs a suction type, in which air is suctioned from the outside and first passes the heat exchanger before entering the engine room. In contrast, a mini-excavator adopts a pusher type, in which the air passes through the engine room before being exhausted outside via a heat exchanger. This is due to the fact that a mini-excavator is configured to place the driver's seat directly above the engine room, which is a heat source, and it is necessary to intake the air as close as possible to the engine room to keep the temperature there low. In such a pusher type, the exhaust temperature after the air has been cooled by the heat exchanger is higher than in suction-type heavy equipment excavators. In addition, the exhaust opening is disposed on the upper side of the engine room in a heavy equipment excavator, whereas, in the mini-excavator, it is placed on the right side of the machine body close to ground level. Furthermore, apart from the cooling exhaust, the engine exhaust of a heavy equipment excavator is discharged through a muffler tail pipe to the upper side of the machine body in the same way as the cooling exhaust. In the case of a mini-excavator with a small machine body and a driver's seat disposed on the top of the body, the engine exhaust is discharged at a low position in the rear of the machine and away from the operator.

Mini-excavators are often operated in narrow spaces, and there is a potential problem in that plants, such as hedges, that are close to the excavator may be withered by the hot air from the exhaust (**Fig. 1**), and it is necessary to consider this at the time of adapting the iNDr.

1.2 Adaption of iNDr = "iNDr+E" [1), 2)]

A cooling system has been developed to adapt iNDr to mini-excavators, not just by incorporating the concept of iNDr for heavy equipment excavators but also introducing solutions to potential problems due to exhaust emissions, as described above.

An iNDr comprises a dust filter on the intake side to prevent dust from entering the machine body. In order to apply this structure to mini-excavators, the cooling fan and heat exchanger are configured to be of the same suction type as in heavy equipment. Also, in devising the positions and sizes of the intake and exhaust openings, the duct was configured to fit in the very narrow machine body of each mini-excavator. The problem of heat affecting the driver's seat was solved by installing the seat with a sufficient amount of heat-insulating material.

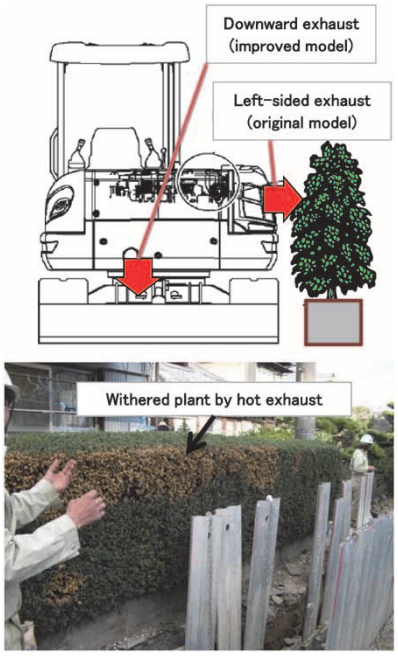

Fig. 1 Example of heat damage caused by mini excavator

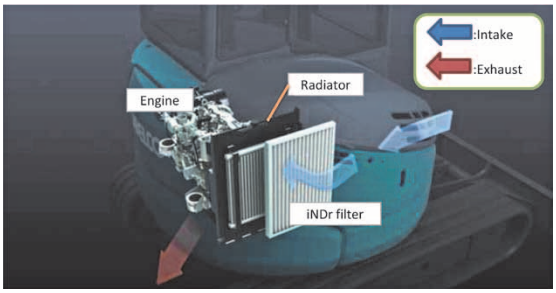

Fig. 2 Cooling air flow of newly developed mini-excavator

In this configuration, the opening on the right side of the machine body, the opening which conventionally has been for exhaust, is used as an intake opening. From this intake opening, a fan, which becomes the source of noise, can be seen directly through the heat exchanger. Hence, as a measure against noise, the duct was offset toward the front so that the internal sound source cannot be seen directly from the opening to reduce the direct sound.

The cooling exhaust, on the other hand, is configured such that its duct fits in the small space around the engine to take into account the previously mentioned harm to plants. The conventional direct exhaust to the left side of the machine body has been changed to an exhaust directed downward from the machine body. **Fig. 2** shows the flow of cooling air in the newly developed mini-excavator.

The hot exhaust gas from the muffler is diffusively discharged into a sound-absorbing exhaust duct installed in the engine room and mixed in the sound-absorbing duct with the exhaust

that has passed through the cooling devices, so that the temperature and sound of the exhaust are reduced as a whole (**Fig. 3**). Having the exhaust flow downward from the machine body has completely eliminated the exhaust to the side or to the rear of the machine body. The tail pipe in the duct has been devised to facilitate the mixing of the engine exhaust with the exhaust passing the cooling devices. That is, the structure of a diffusion pipe covered all over with small holes has been adopted, in which the number and arrangement of the holes have been adjusted so that the exhaust gas is discharged uniformly.

The above new function is referred to as "iNDr + E" ("E" for exhaust) and has been set as a standard on-board function for mini-excavators.

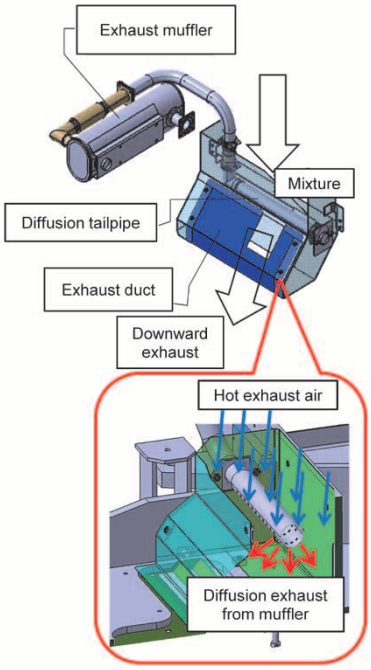

Fig. 3 iNDr+E: Mixing part of diffusion exhaust in exhaust duct

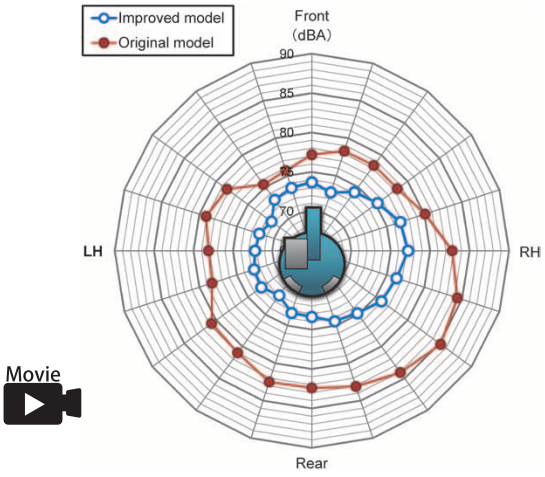

Fig. 4 Comparison of noise near mini excavator

As described above, the change from the conventional side exhaust to downward exhaust has enabled a significant reduction of noise in the proximal area of the excavator (1 m from the machine side, **Fig. 4**) and has resolved the issue of heat damage to plants, etc.

2. Evolution of iNDr for heavy equipment excavators

2.1 Challenges of iNDr for heavy equipment excavators

Since its launch in 2007, urban-type, general-purpose, heavy equipment excavators, each equipped with an iNDr, have gradually penetrated the market and gained recognition, while repeating minor changes and maintaining iNDr's extremely low noise performance and dustproof performance.

The 4th regulation of engine exhaust emissions, however, requires urea selective catalytic reduction (SCR) in addition to the conventional diesel particulate filter (DPF). The measures taken to comply with the 4th regulation of engine exhaust emissions and the layout of the post-processing apparatus are shown in **Fig. 5**. In the conventional iNDr, the exhaust side had a sound absorbing duct structure fitting the width of the machine body in the lateral direction (the left-to-right direction in Fig. 5) to secure the length and thereby to secure the noise reduction performance. The installation of urea SCR, however, has made it difficult to secure enough length even if a bending duct is constructed before the urea SCR.

In addition, securing the necessary exhaust opening area makes it difficult to maintain extremely low noise performance, because of the difficulty it causes in configuring the engine room such that no part of its interior can be seen from the exhaust opening. Furthermore, regarding the heat balance, the amount of heat generated in the engine body has been increased to comply with the engine emissions regulations, requiring an increase in the amount of cooling air.

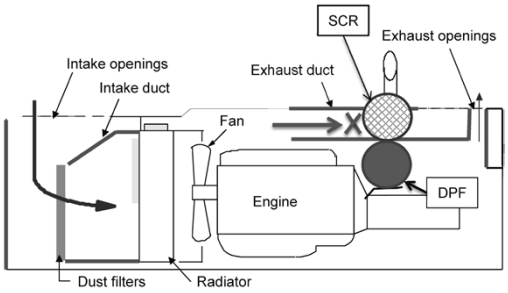

Fig. 5 Influence of SCR addition in heavy equipment excavator

Noise and heat balance are in a trade-off relationship, and the important challenge in this development has been to maintain both the cooling performance and heat balance while maintaining extremely low noise performance in a limited space.

2.2 Utilization of one-dimensional (1 D) design tool

In order to establish the heat balance performance, a sufficient amount of cooling air must be secured. The amount of cooling air can be determined from the capacity of the installed fan and ventilation resistance. The ventilation resistance of the complicated duct structure and the flow passage configuration in the engine room has so far been estimated by repeated verification using simplified bench tests and actual machine mockups based on the design review proposals, and a large amount of time has been spent in model-making for the experiment.

A 1-D design tool for predicting the amount of cooling air was developed and utilized to enable simple examination during the initial stage of the planning. For this tool, the excavator's engine room is first modeled as a piping flow passage connecting the intake opening to the exhaust opening (**Fig. 6**), and the resistances estimated from the resistance coefficients for typical pipeline types are summed up to obtain the ventilation resistance. Then the estimated resistance is matched with the performance diagram of the fan to finally estimate and calculate the air volume.

Fig. 7 shows the calculation results of the ventilation resistance predicted for an iNDr machine equipped with the new sound-absorbing exhaust duct. A complex flow passage configuration has been divided into simple models, and the calculation has been performed on the coupling of these simple models. As a result, a ventilation resistance equal to or less than that of the conventional model has been obtained with the prospect of securing the necessary air volume.

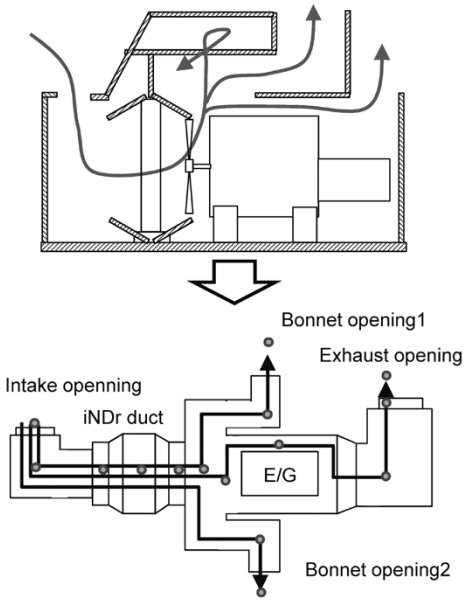

Fig. 6 Modeling of duct for cooling air passage in engine room of heavy equipment excavator

2.3 Installation of new sound-absorbing exhaust duct

In order to make use of the effect of the L-shaped duct conventionally adopted, a study was conducted using the 1-D design tool for a new sound-absorbing exhaust duct with a soundproof structure combining two L shaped ducts, each having an exhaust opening with an area half that of the required area. As a result, it has been revealed that a three-dimensionally crossing arrangement (upward and leftward) of the duct, instead of a unidirectional arrangement of the intake/discharge ports of the duct, realizes an L-shaped duct whose inside is not directly visible, being configured in a very narrow space. The configuration of the newly developed sound-absorbing exhaust duct is shown in **Fig. 8** along with the flow of exhaust cooling air.

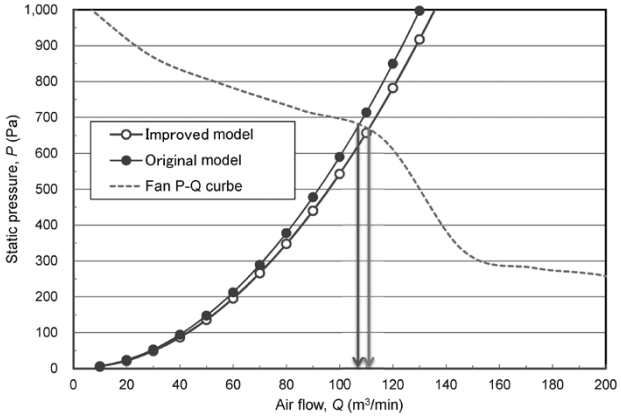

Fig. 7 Calculation results predicting ventilation resistance of conventional and improved excavator models

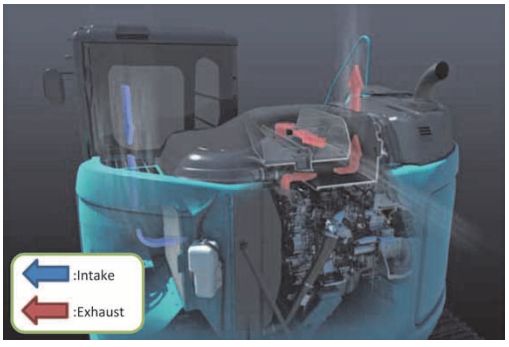

Fig. 8 Cooling air flow of "Cross Over duct" for heavy equipment excavators

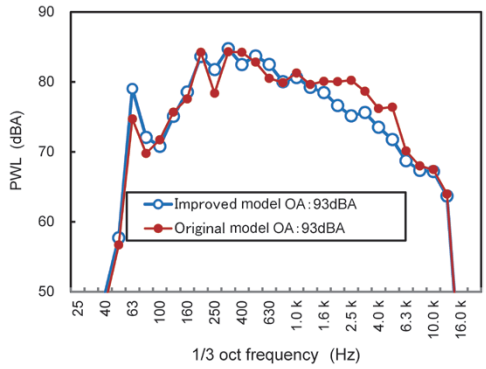

Fig. 9 Comparison of measured sound levels in conventional and in improved model heavy equipment excavators

Thus, the development of a "crossover duct," in which L-shaped ducts are three-dimensionally crossing, has made it possible to simultaneously secure the heat balance and extremely low noise performance, which was the challenge during development.

Fig. 9 compares the acoustic power levels (measured values) of the conventional machine and the new machine. This figure shows that the surrounding area noise of the new machine is 93 dBA, which is equivalent to the value for the conventional machine.

Conclusions

It has been recognized that low noise performance and heat balance are in a trade-off relationship and it is necessary to be constantly aware of and aim at both. This achievement, however, has become more difficult for each new development, and this trend is expected to continue in the future.

As a study tool for this issue, it will be necessary to enhance the 1-D design tool that takes advanced and detailed analysis technology trends into account to find trends with various review conditions in the early stages of designing.

It is also important to improve the work environment from the viewpoint of the labor supply, which is decreasing due to a low birthrate and longevity; and, to this end, the noise of hydraulic excavators must be further reduced in the future.

With regard to the noise in surrounding areas, it is envisaged that not only the noise from the main machine body, but also the noise, including impact sounds, emanating from various parts during actual operation, must be reduced in the future. Moreover, measures against noise in the cabs are required in addition to the measures against surrounding area noise. It is conceivable that, rather than simply reducing the noise level, it will become necessary to improve the sound quality in the driver's cab, making use of the sort of sound that is necessary for operating the machine and is less likely to fatigue the operators. Furthermore, lowering noise will contribute to safety aspects, in that communications in the surrounding area will be improved as the once inaudible sound (voice) becomes audible.

We will continue to develop extremely-low-noise-type hydraulic excavators to contribute to the improvement of the work environment and will strive to improve the technology to realize work sites that are more comfortable and safer.

References

1) H. Nakajima et al. *R&D Kobe Steel Engineering Report*. 2012, Vol.62, No.1, pp.27-31.
2) K. Ueda. *Journal of Japan Construction Mechanization Association, Construction Mechanization*. 2014, Vol.66, No.1, pp.20-23.

Development of New Production Scheduling and Manufacturing Logistics System for Takasago Machinery Plant

Rihito IZUTSU*1, Toyohiro UMEDA*2, Hideo IKEDA*2, Yukihiro ONISHI*3, Ryusuke MORISAKI*3

*1 AI Promotion Project Department, Technical Development Group
*2 Production Systems Research Laboratory, Technical Development Group
*3 Takasago Machining & Instrumentation Assembly Department, Machinery Center, Machinery Business

For the machinery plant of the make-to-order (MTO) type Machinery Center in the Takasago Works of Kobe Steel, a system for scheduling and logistics management has been developed to improve the product assortment rate, an index for the rate of on-time delivery to the subsequent assembly plant. For scheduling, a method was devised for estimating excessive overloading to support the determination of the amount to be outsourced. For the logistics, a mechanism was established to collect progress data and the locations of parts with RFIDs, the information necessary for preparing schedules. The introduction of this system has improved the assortment rate by approximately 20% compared with the value normalized by the average assortment rate before the introduction of the system.

Introduction

Kobe Steel's Machinery Business manufactures made-to-order machinery such as (reciprocating, turbo, and screw) compressors, resin mixers and rubber mixers at its Takasago Works. Parts machined in-house are manufactured at the processing plant in the Works and assembled together with outsourced items into final products in the assembly plant. To improve the productivity of assembly, it is essential that necessary parts be available in the assembly process on the scheduled start date of assembly. In order to improve the "assortment rate," the index of availability, the machines and workers, which are the resources of the processing plant, must be fully used. In addition, to avoid overload situations, the minimum required amount of work must be outsourced beforehand to adjust the load of the processing plant.

The processing plant, however, is a large-scale, job-shop type plant that processes each item to order, and it has conventionally been impossible to prepare the schedules for the total of 50,000 operations even with multiple planners. There was no way of making instructions for the work site considering the plant as a whole. Thus, at a large-scale plant, the process planning was unavoidably limited to certain types of machines. It has been difficult to accurately estimate the load situation for the next half year or so, an estimation necessary for production management, making it impossible to properly judge the need for outsourcing or to adjust the load by overtime work. Also, no location management of a large number of parts was implemented in the plant, making it difficult to synchronize transportation with the plans, posing a challenge to the improvement of the assortment rate.

There are various studies on the technique for solving scheduling problems in job-shop-type plants, and simulation-based techniques have been proposed for due-date oriented problems.[1] There also have been proposed simulation-based techniques for adjusting overtime work to prevent delayed delivery.[2), 3] A technique has also been proposed for estimating the amount of overtime using a genetic algorithm so as to strictly adhere to the due date.[4]

The reported examples,[2)-4] however, are based on the adjustment of the overtime put in by in-house workers and do not assume the use of outsourcing. Meanwhile, a time-bucket technique that calculates the load per unit period has been proposed as a technique for estimating the required strengthening of in-house machines, rather than outsourcing.[5] The time-bucket technique, however, cannot determine the clock time of a task by its nature, and its accuracy tends to be rough, making it difficult to properly adjust the load.

In order to solve the problem of estimating the amount of outsourcing necessary in order to strictly meet the due date in job-shop-type factories, Kobe Steel proposed a simulation-based technique allowing high-speed calculation and constructed a scheduling system using it. Also developed was a logistics management system, called Innovative Logistics and Intelligent Scheduling System (hereinafter referred to as "iLiss"), for collecting the progress information necessary for planning and information on the parts locations required for transportation synchronized with the plan. This paper outlines those systems.

1. System configuration

As shown in **Fig. 1**, the newly developed system consists of a scheduling system (hereinafter referred to as "iLiss-S") and a logistics management system (hereinafter referred to as "iLiss-L"). The scheduling

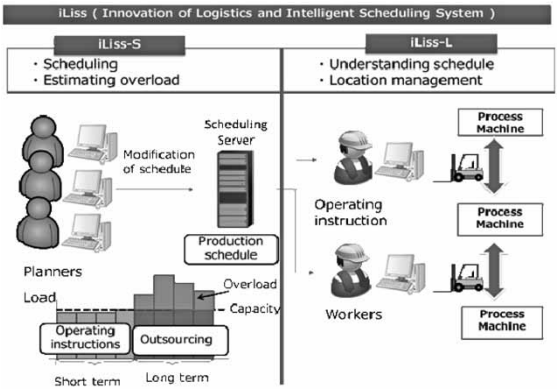

Fig. 1 Outline of newly developed scheduling and logistics systems

system draws up medium-to-long term plans (more than 1 month away) and short term plans (current to 1 month away). These plans are devised and used differently. The short term plan is used to transmit task orders to the field workers, and the medium-to-long term plan is used to determine outsourcing. The logistics management system enables the confirmation of scheduling and progress input by PCs installed on the work site. It also uses radio frequency identifications (RFIDs) to perform the location management of parts necessary to realize transportation synchronized with the plan.

The following sections describe the respective functions of the scheduling system and the logistics management system.

2. Scheduling system

The scheduling system adapts a planning method of forward scheduling whose details are different from those of short term planning and mediam-to-long term planning.

The medium-to-long term planning aims at grasping the excess load in order to make a decision on outsourcing. Hence, plans are created adhering to the due date restriction, and the machine capacity restriction and worker capacity restriction are relaxed as necessary. The machines and workers that can be allocated in the shortest term, are selected from the available ones in the master data. The dispatching rule applies SLACK,[6] which is effective in reducing delivery delay. SLACK is a method for performing task allocation in the ascending order of margin time, which is the time remaining after the time for residual tasks is subtracted from the time remaining until the due date. The details will be described in Section 2.1.

The short term plans aim at instructing the work site about tasks; hence a feasible plan that adheres to the machine capacity restriction and worker capacity restriction is drafted. The same machines and workers selected before rescheduling are used, and the dispatching rule is set in the order of the earliness of the start time in the previous plan before rescheduling. **Table 1** shows the scheduling methods of short, medium to long-term plans.

2.1 Planning algorithm for medium-to-long term plan

The planning algorithm for the medium-to-long term plan is as follows.

Step 1: [Selection of task]

The task with the smallest margin time, the time remaining after the time for residual tasks is subtracted from the time remaining until the due date, is selected from among the unallocated tasks whose previous jobs have been allocated. As an example, a case is considered where a certain job is processed through the tasks of the first to third steps. If the allocation up to the first step has been completed, the margin time for the second step is calculated as follows:

$$d - now - \Sigma_{i=2}^{3} T_i \quad \cdots\cdots (1)$$

wherein d is the due date of the job, now is the end-time of the first step, and T_i is the task time of the i^{th} step.

Step 2: [Preliminary allocation of task]

The selected task is preliminarily allocated within the machine capacity restriction and worker capacity restriction. Here, among the available machines, the one that can be allocated earliest is selected. For the worker, the person who use the smallest number of machines is selected.

Step 3: [Allocation of task]

If the end-time of the preliminarily allocated task does not exceed the latest end-time, the preliminary allocation is regarded as the final allocation, as is. If it exceeds the latest end-time, it is allocated as an overload task immediately after the previous task in

Table 1 Scheduling method for short, and medium-to-long term plans

Term	Purpose	Restriction	Dispatching rule	Machine selection	Worker selection
Short	Operating instructions	Machine and worker capacity	Earliest start-time in prior schedule	Fixed	Fixed
Long	Making decision on outsourcing	Machine and worker capacity (Relaxing restriction if needed) On-time delivery	SLACK	Select machine so that a task can start earliest.	Select worker with smallest number of available machines.

the job of said task. Here the term "latest end-time" refers to the time when any task finished after this time causes a delivery delay, even if the later process is allocated the shortest time. For example, the latest end-time of the first step of the job described in Step 1 is as follows:

$$d - \sum_{i=2}^{3} T_i \quad \cdots\cdots (2)$$

[Repeat]

Steps 1 to 3 are repeated until all the tasks have been allocated.

Fig. 2 shows the image of the algorithm. The medium-to-long term plan is made so as always to keep the due date because the allocation as an overload task is restricted by the due date and the restriction of machine capacity is relaxed as necessary. The planners can focus on overload tasks to make decisions on planning modifications such as the outsourcing of the overload task and workers overtime.

2.2 Planning algorithm for short term plan

The specific planning algorithm for the short term plan is as follows:

Step 1: [Selection of task]

The task with the earliest start time before the rescheduling is selected from among the unallocated tasks whose previous jobs have been allocated.

Step 2: [Allocation of task]

The selected task is allocated within the machine capacity restriction and worker capacity restriction. Here, the machine is to be the same one as before the rescheduling. For the worker, the person who can use the smallest number of machines is selected.

In the task selection of Step 1, changes in the plan before and after rescheduling are suppressed, since the task having the earliest start time before rescheduling is selected. For example, a task planned for the next day is not allowed to suddenly be automatically postponed by one week after the rescheduling. This prevents confusion on the work site.

[Repeat]

Steps 1 and 2 are repeated until all the tasks are allocated.

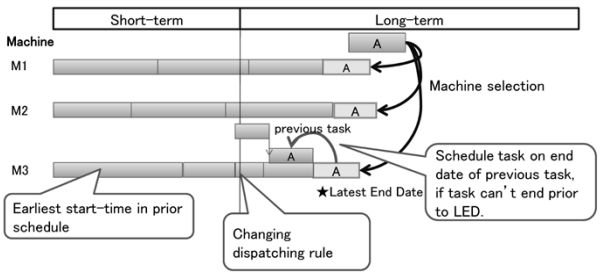

Fig. 2 Scheduling method for overload tasks

2.3 Necessity of plan modification

As mentioned above, allocation in the medium-to-long term plan is performed in the priority order of the margin time based on due date. A task planned for the medium-to-long term will be planned for the short term as time passes. Hence, the short term plan, which prioritizes the start time of the previous plan, is indirectly regarded as an allocation with the priority of margin time. Merely setting such margin time in priority order is inadequate in the following cases, and the plan must be modified according to the judgment of the planner.

- In some cases, tasks can be streamlined by continuing the same type of task. To this end, the planner judges as to whether some tasks are of the same type, and modification occurs to make those tasks continue.
- In the short term plan, a machine change or modification in task order occurs to reduce the non-operating time of the machine caused by the difference between the plan and the progress made. In such cases, if the machine is changed or the task order is modified automatically by the planning logic, there may be confusion on the work site.

On the other hand, the medium-to-long term plan is a plan for at least one month in advance, and an automatic change in the plan after rescheduling will not cause any confusion on the work site. Therefore, if the planning logic is rescheduled in consideration of the margin time in accordance with a progress shift, there will be no need to change machines or task orders with the planner's judgment, and it will only be necessary to decide which processing vendors should be assigned the outsourcing of the overloaded tasks.

2.4 Behavior of rescheduling after modification

Since there are several planners in the plant, a function has been developed to allow more than one planner to modify plans. A modification is focused on the change of task order in each machine and the machine used for each task. For a short-term plan and medium-to-long term plan, the modifiable points differ as follows:

- For short term plans, the task orders and machines are changeable.
- For medium-to-long term plans, machine selection is made within the planning logic, but the machine can be set in advance if the planner

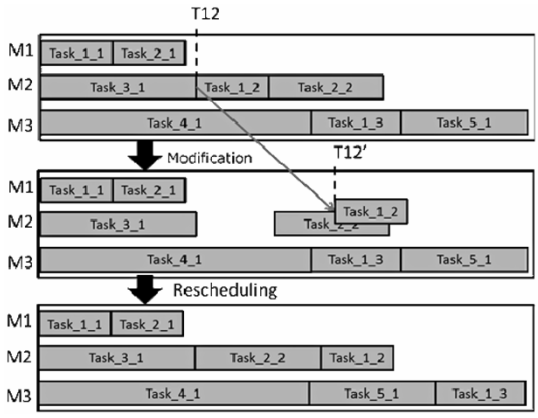

Fig. 3 Rescheduling after modification

wishes. Also, the subcontractors for overload tasks can be selected. Even if the task order in a machine is changed, the planning is performed with the margin time as a priority.

As for the modification of plans by planners, only the tasks that have editing rights in the Gantt chart can be modified. In other words, if the right to edit a task has been given to other planners, that task will not be provided with editing rights. This prevents the same task from being modified by multiple people simultaneously.

The rescheduling behavior after a modification is explained on the basis of the example in **Fig. 3**. The Gantt chart at the top represents the situation before rescheduling; the one in the middle, immediately after the modification; and the one at the bottom, after rescheduling. Here, Task_K_N means the N^{th} step of Job K, and TKN indicates the start time of Task_K_N. Before the rescheduling in the middle, the right to edit Task_1_2 is acquired, and its start time is modified from T12 to T12'. For rescheduling after modification, a short term plan logic is applied for short term plans and a medium-to-long term plan logic is applied for medium-to-long term plans. For modified Task_1_2, T12' is set as the start time of the previous plan.

Immediately after the plan is modified by the planner, the start time, T12', of Task_1_2 falls in the future (later) direction of the start time, T13, of the subsequent task, Task_1_3, causing a contradiction in the anteroposterior relationship of the tasks. It is shown that the contradiction has been resolved after the rescheduling.

3. Logistics management system

Approximately 190 PC terminals were installed beside the processing machines in order to instruct the work site concerning the plan prepared by the scheduling system and to collect the latest progress information necessary at the time of rescheduling.

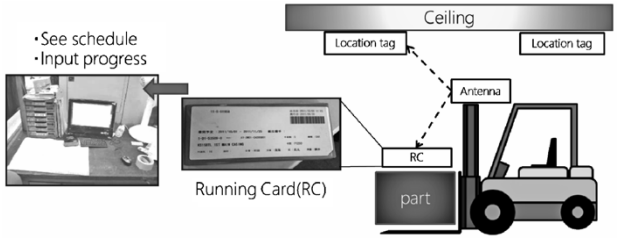

Fig. 4 Logistics management system

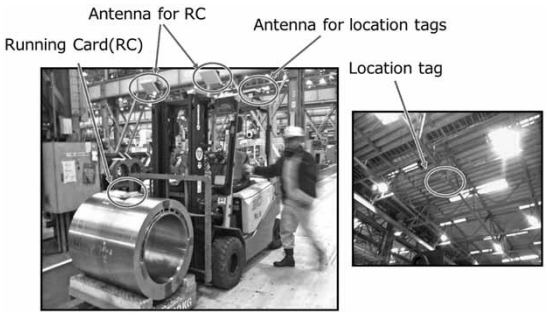

Fig. 5 Location management functions in logistics management system

In addition, RFIDs were introduced to carry out the location management of the parts necessary for realizing transport synchronized with the plan. **Fig. 4** shows the configuration of the logistics management system.

3.1 Achievement collection function

Progress information, such as which tasks are completed, and how long they are in progress and how long they are likely to take to be completed in the case of long tasks that take several days is important for highly accurate scheduling. Hence, an achievement collection function has been developed to allow PC terminals to read the task instruction cards with an RFID placed on each part and allow management to input progress information.

3.2 Location management function

A function has been developed to detect which items have been transported to which locations by installing approximately 300 long-distance detection type RFID tags on the above task instruction cards, ceilings, pillars, etc., while detecting them using an antenna installed on each forklift. Another function has also been developed so that a worker can wirelessly transmit a request to a forklift terminal to transfer processed parts to the next process. These two functions have enabled the synchronization of processing and logistics within the plant, synchronization being difficult to achieve by scheduling alone. **Fig. 5** shows the operational status of location management.

4. Operational status

The developed scheduling/logistics management systems were put in operation in the processing plant in February 2012. The time required to schedule the preparation of 50,000 tasks up to six months in advance is about 20 minutes; this includes the acquisition of order data and actual data from the upper production management system. **Table 2** shows the specifications used by the scheduling server in preparing the schedules.

The transition of the assortment rate since the start of operations was normalized by the average assortment rate in 2011 and is shown in **Fig. 6**. The improvement in the assortment rate has been confirmed after the introduction of this system.

Table 2 Specifications of scheduling server

OS	Windows Server 2008
CPU	Intel Xeon 2.30 GHz
MEMORY	12 GB

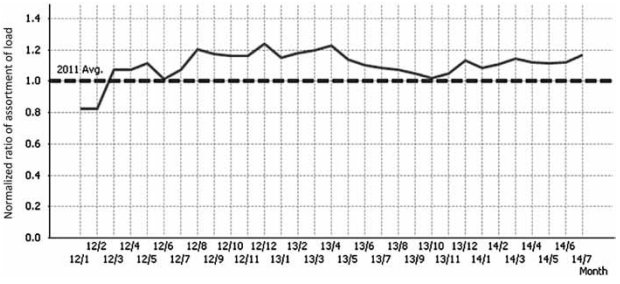

Fig. 6 Normalized assortment rate

Conclusions

A scheduling system has been constructed for a plant machining parts for machinery to prepare medium-to-long term plans that support the judgment on outsourcing necessary to meet the due date of processing, and short term plans to be used for task instruction. This system comprises two plan newly developed logics; namely, a medium-to-long term plan logic, which takes the due date as a restriction for outsourcing decision while relaxing as necessary the restriction on machine capacity, and a short-term plan logic to prepare a short-term plan seamlessly connected with each medium-to-long term plan. In addition, a logistics management system utilizing RFIDs has been developed to collect progress information and other data necessary for preparing the plans.

The direct effect of this system has been confirmed by the improvement of assortment rate after operation. The future technical challenge lies in the method of extracting a task that makes a large contribution to the improvement of the assortment rate upon outsourcing, in order to further improve the efficiency of the outsourcing study.

References

1) M. Fuyuki et al. *Journal of Japan Industrial Management Association*. 1995, Vol.46, No.2, pp.144-151.
2) M. Arakawa. *Journal of Japan Industrial Management Association*. 2001, Vol.51, No.6, pp.603-612.
3) M. Arakawa. *Transactions of the Institute of Systems, Control and Information Engineers*. 2003, Vol.16, No.9, pp.451-460.
4) M. Yoda. *Transactions of the Japan Society of Mechanical Engineers*. 2013, Vol.79, No.807, pp.423-433.
5) J. C. Chen et al. *International Journal of Electronic Business Management*. 2011, Vol.9, No.1, pp.46-57.
6) Jens Kuhpfahl. *Job Shop Scheduling with Consideration of Due Dates*. Springer Gabler, 2015, Vol.1, p.173.

Method for Predicting Gas Channeling in Blast Furnace

Kazufumi KAMO*1, Kazuhisa HAMAMOTO*1, Dr. Hiroshi NARAZAKI*1, Dr. Tomoyuki MAEDA*2, Masahiro YAKEYA*3, Yosuke TANAKA*4

*1 AI Promotion Project Department, Technical Development Group
*2 Production Systems Research Laboratory, Technical Development Group
*3 Ironmaking Development Department, Kakogawa Works, Iron & Steel Business
*4 Ironmaking Department, Kakogawa Works, Iron & Steel Business

In order to maintain stable operation of a blast furnace, deviations from the steady state should be quickly detected and corrected. Because internal physical states are difficult to measure directly, experienced operators play a crucial role in integrating information from various sources such as sensors and visual observations so as to recognize, predict, and react to probable anomalies. Overlooking undesirable symptoms or delayed actions possibly leads to the excessive loss of heat, which, in the worst case, can cause the abnormal shutdown of operation. One of the events highly associated with the risk of heat loss is gas channeling, which sets off an alarm signaling to the operator to decrease the flow rate of input hot gas. Gas channeling is judged to be imminent by the integration of indices designed so as to detect unusual changes in the variations and patterns of sensory data. The precision of our prediction method is evaluated by using actual data.

Introduction

In an integrated steelworks, iron ore, auxiliary materials and sintered ore, which is pretreated iron ore, are constantly charged from the top of a blast furnace and are reduced, melted, and carburized inside the furnace to continuously produce high-temperature molten iron. The interior of a blast furnace is a high-temperature, high-pressure, dusty environment, and it is difficult to directly measure the conditions inside the furnace. Hence, a number of sensors are installed on the furnace walls. It is important for the stable operation of a blast furnace to estimate and predict the state and its changes inside the furnace from the data acquired by these sensors such that appropriate operational action can be taken. Overlooking anomaly symptoms and/or making an erroneous judgment may result in equipment damage due to high-temperature gas, or the solidification of pig iron inside the furnace due to the lack of a heat supply: this can lead to the discontinuation of production. Since a blast furnace is located at the uppermost stream of each steelworks, a disruption of the blast furnace production will affect the entire steelworks.

Thus, maintaining the stable operation of the blast furnace is an important task, and a variety of research has been carried out on the subject. Examples include estimating the shapes formed by fused matter in the furnace, which influence the state of the blast furnace,[1] and furnace heat control using AI technology.[2] These technological developments have been carried out to support stable operation by estimating and evaluating the furnace conditions from burden materials and sensor information. A blast furnace process, however, has various factors that are complicatedly intertwined, and, in reality, a large part of the furnace operation relies on the comprehensive judgment and skills of experienced operators.

Meanwhile, experienced operators are being replaced by younger ones as the generations change, causing concerns about missing anomaly symptoms and making erroneous judgments due to the lack of their experience and resulting lack of skills. Therefore, there is a demand for technologies and tools that support the awareness and judgment of operators.

Recent advancements in ICT have made significant progress in the technology for analyzing a large amount of data to support human judgment and actions. It was against this backdrop that Kobe Steel began to develop a gas-channeling prediction technology based on data analysis for supporting operators in order to raise awareness of the risk of gas-channeling occurrence, which is one of the anomaly events in blast furnace operation. Gas channeling is a phenomenon in which the pressure inside a blast furnace gradually increases, and the blast furnace gas is discharged from the furnace top at a pressure and temperature higher than usual. This is caused by disturbed furnace conditions obstructing the flow of the hot air, which is blown from the furnace bottom and rises up in the blast furnace as reductant gas (hereinafter referred to as ventilation failure).

Various methods have been attempted to predict gas channeling, including the analysis of pressure frequency[3] and the analysis of the main component.[4] The cause of gas channeling, however, is complicated, leaving some room for the operators' judgment.

Hence, Kobe Steel applied statistical processing and pattern classification techniques to various types of sensory information and defined a plurality of

feature quantities that correlated highly with the risks of gas channeling. By combining these feature quantities, the company has put into practical use an operation support system that provides operators with a quantitative index of gas channeling risks. This paper gives an outline of the system and reports the results of its application.

1. Outline of gas channeling prediction system

Once it occurs, gas channeling may cause serious troubles such as the destruction of furnace-top equipment and furnace heat drop due to increased heat loss. A precursor phenomenon of this gas channeling is a pressure rise due to a failure in the ventilation of reductant gas. Ito et al. use the magnitude of monitoring data including pressure as the criterion for gas channeling prediction.[5] The pressure rise, however, occurs due to various factors, and considering only the occurrence of pressure rise as a "gas channeling risk" leads to overdetection. From the viewpoint of data processing, such a problem can also be regarded as a change-point detection problem in time series data. There is, for example, a technology that detects internet virus infection on the basis of changes in data communication volume;[6] however, gas channeling is an event occurring in a nonsteady state, and it is not easy to detect changes in a great fluctuation in the first place. A detailed examination of the data on actual gas channeling occurrence has revealed that the pressure rise is immediately accompanied by a significant deviation from the normal state of the furnace temperature and its spatial distribution.

Therefore, an attempt was made to express the risk of gas channeling by a permeability index that involves not only pressure but also a number of the temperatures of these anomaly states, which appear before gas channeling. Kobe Steel has now developed a system for predicting gas channeling in which an alarm, "Timing for lowering blow," is issued at the time when pressure suddenly rises during a period with a high index of permeability.

A method has been proposed in the past for predicting the occurrence of gas channeling by calculating a plurality of feature quantities from such data behavior before gas channeling.[7] Prediction based on a plurality of feature quantities, however, requires a plurality of parameters corresponding thereto, and it is necessary to adjust each parameter each time the operational state changes. Adjusting these parameters with operation analysis done by hand can hinder long-term stable operation.

Hence, a tool has also been developed to enable the adjustment of multiple parameters with less effort by standardizing the method of parameter adjustment.

2. Constitution of permeability index and method of calculating it

This section details the feature quantities and how they are calculated; feature quantities constitute the permeability index, which is the core of the gas channeling prediction system.

2.1 Selection of feature quantities constituting permeability index

As mentioned above, gas channeling phenomena deeply involve temperature distribution in a furnace in addition to pressure rise. For this reason, feature quantities, SC_1 to SC_8, described below, are set as the constituents of the permeability index. As will be described later, the permeability index is finally derived by combining these feature quantities.

2.1.1 Pressure fluctuation

Data analysis has revealed that the pressure violently fluctuates each time before gas channeling occurs. Two fluctuation patterns have been found: one that continues for a long period of time and another that becomes concentrated in a short period of time. Furthermore, it has been found that the fluctuations occur across furnace walls. Therefore, these phenomena with different time scopes were quantified using multiple variances of the measured values of the pressure, and the pressure fluctuation was quantified by combining them. More specifically, four time periods of 5 minutes, 60 minutes, 120 minutes, and 240 minutes are set for four height positions: that is, 4 heights × 4 time periods = 16 periods are set. On the basis of the number of periods where the fluctuation exceeds the threshold adjusted on the basis of the actual results, a score is calculated by Equation (1):

$$SC_1 = N\left(\sum_h f_1(P_{h,t}(t-5), P_{h,t}(t-60), P_{h,t}(t-120), P_{h,t}(t-240))\right) \quad \cdots\cdots (1)$$

wherein

SC_1: temporal fluctuation feature quantity of pressure (hereinafter, different subscripts indicate respective feature quantities),

t: time (minute(s)),

N: function to convert input value to the index value of 0~1 (detail is described in Section 3),

f_1: value scored by counting the number of items of input variables exceeding the threshold

and giving the zeroth and first items 0 points, second item 1 point, third item 2 points, and fourth item 3 points,

h: height in the blast furnace (for the present feature quantity, the four heights from the upper furnace to the lower furnace[Note 1)]),

$p_{h,t}(t_1)$: time average value between t_1 and t of 120 minutes variance of the average value of total pressure at height h.

2.1.2 Uniformity of temperature distribution in circumferential direction

For a case where the gas flow is disturbed (drifted), the temperature distribution and the position of the center of gravity in a cross-section of a blast furnace are shown by the star in **Fig. 1**. The temperature distribution becomes uneven in the cross-section of the furnace, and the high temperature range expands in a specific direction. Then, the center of the mass coordinate is calculated on the basis of the temperature distribution in the circumferential direction, as expressed by Equation (2), so that the deviation from the center is incorporated in the permeability index. The deviation is calculated for each one of multiple heights and indexed into a real value from 0 to 1 (indexing method will be described later), and the maximum value of the index value at each height is taken as the score of the temperature distribution evaluation:

$$SC_2=\max_h N(f_2(T_{h,d}, n_h, \theta_{h,d}))$$
$$f_2=\frac{1}{n_h}\sqrt{\left(\sum_{d=1}^{n_h} T_{h,d}\cos\theta_{h,d}\right)^2+\left(\sum_{d=1}^{n_h} T_{h,d}\sin\theta_{h,d}\right)^2} \quad \cdots\cdots (2)$$

wherein

h: heights in the blast furnace (the upper three heights in this feature quantity),

d: the serial number of each sensor at height h,

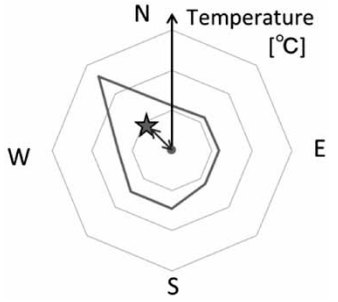

Fig. 1 Temperature distribution in circumferential direction

$T_{h,d}$: measurement value of d^{th} temperature sensor at height h,

n_h: number of temperature sensors at height h,

$\theta_{h,d}$: angle of the d^{th} sensor with respect to the first sensor at height h.

2.1.3 Uniformity of upper furnace temperature

Before gas channeling occurs, there is a tendency for the stave temperature distribution in the height direction to change greatly: e.g., the mid-furnace temperature becomes higher than the upper furnace temperature. In order to capture such phenomena, a feature quantity as in Equation (3) is defined:

$$SC_3=N\ (T_{h1}-T_{h2}) \quad \cdots\cdots (3)$$

wherein

$h1, h2$: heights in a blast furnace (in this feature quantity, representing two heights in the upper furnace),

T_h: 120 minutes time average of the average values of all temperature sensor measurements at height h.

2.1.4 Upper furnace temperature

Before gas channeling, the temperature in the upper part of the furnace often becomes markedly high, and if the upper furnace temperature is uneven, it is assumed that the risk of gas channeling has increased further. Therefore, in addition to the upper furnace temperature, a feature quantity that also takes into account the feature quantity of *"upper furnace temperature uniformity" is defined:*

$$SC_4=\frac{\Sigma_h N(T_h)+\mathrm{SC}_3}{4} \quad \cdots\cdots (4)$$

wherein

h: heights in a blast furnace (in this feature quantity, it represents three heights in the upper furnace),

T_h: average value of the average values, for the past 120 minutes, of all the temperature sensors at height h.

2.1.5 Mid-furnace temperature

So far, in the main, temperatures measured in the upper part of the furnace have been used to calculate the score. However, when the furnace condition deteriorates, the temperature in the mid-furnace tends to rise greatly as compared with what is usual. Therefore, the increase in the mid-furnace temperature is captured as a feature quantity in Equation (5).

Note 1) In this paper, the blast furnace is divided into three parts in the perpendicular direction; i.e., upper furnace, mid-furnace, and lower furnace, in order from the top.

$$SC_5 = N\left(\max_{(h,d)} Z_{h,d}\right) \quad \cdots\cdots (5)$$

wherein

h: heights in a blast furnace (in this feature quantity, it represents two heights in mid-furnace)

d: the serial number of each sensor at height h,

$Z_{h,d}$: normalized temperature of $T_{h,d}$,

μ: average over time,

σ: standard deviation over time

2.1.6 Temperature difference in perpendicular direction

Fig. 2 shows the values at three time points before gas channeling that occurred in the past, with the vertical axis as height in the blast furnace and the horizontal axis as normalized temperature. It is shown that, as gas channeling approaches, the temperature difference between the high temperature part and the low temperature part becomes remarkable, and the temperature distribution deviates from normal. The change in the distribution at that time is captured by a feature quantity expressed by Equation (6).

$$SC_6 = N\left(\max_{d}\left(\max_{h} Z_{h,d} - \min_{h} Z_{h,d}\right)\right) \quad \cdots\cdots (6)$$

2.1.7 Temperature of furnace-top gas

The temperature of furnace-top gas rises when furnace conditions deteriorate. Therefore, its maximum value for a certain period is used as the feature quantity:

$$SC_7 = N\left(\max_{t} T_{top}\right) \quad \cdots\cdots (7)$$

wherein T_{top}: temperature of furnace-top gas

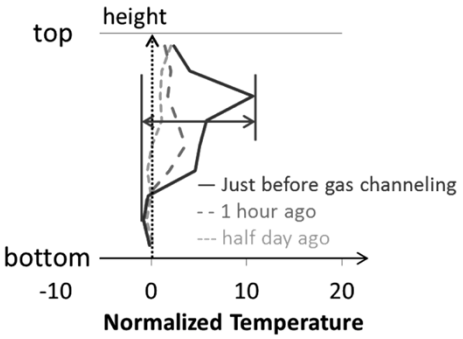

Fig. 2 Temperature distribution along furnace axis immediately before channeling

2.1.8 Blast pressure

Like the furnace-top gas temperature, the blast pressure has the same tendency to rise and is defined as the feature quantity:

$$SC_8 = N\left(\max_{t} P_{bottom}\right) \quad \cdots\cdots (8)$$

wherein P_{bottom}: blasting pressure.

2.2 Method of indexing feature quantities

Before combining these feature quantities, indexing was carried out to express the degree of deviation from the median value in the distribution of each feature quantity. The method of indexing is shown in **Fig. 3**. Fig. 3 shows the frequency distribution of the data collected in the top of the furnace, the cumulative distribution in the middle, and the indexed function using the parameters determined from the distribution in the bottom. As shown in Fig. 3, the indexing is performed as follows using the 50% value of cumulative frequency and α% value.

0 ～50%: 0 (regarded as the normal state)

50%～α%: 0～1 (regarded as a period of transition to a deviated state)

α%～100%: 1 (regarded as the deviated state).

The parameter α is determined by a method explained in Section 3.

2.3 Definition and evaluation of permeability index

Kobe Steel has developed a permeability index with a combination of feature quantities and

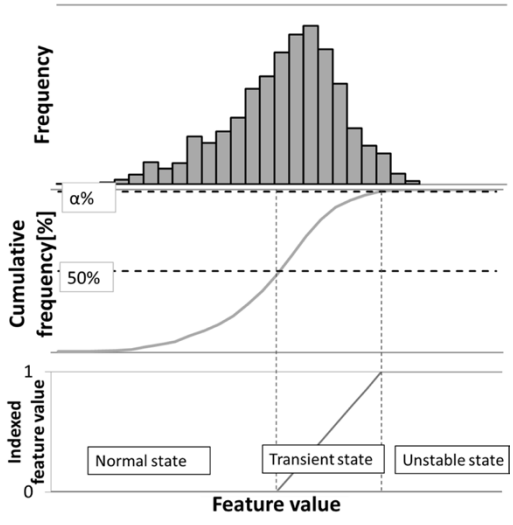

Fig. 3 Conceptual representation of indexed feature quantity using parameter α from cumulative frequency distribution

developed an approach to select the best candidate among three types of index candidates (SC_A, SC_B, SC_C).

In the first candidate, SC_A, the "pressure fluctuation" (Section 2.1.1), has been defined as the permeability index as expressed by Equation (9), focusing on the large pressure fluctuation before gas channeling:

$$SC_A = SC_1 \quad \cdots\cdots (9)$$

In the second candidate, SC_B, considering the feature quantities of the temperature patterns (Section 2.1.2 and Section 2.1.3) characteristically observed before gas channeling that is difficult to detect by SC_A, the permeability index is defined by Equation (10):

$$SC_B = \min(SC_1, SC_2, SC_3) \quad \cdots\cdots (10)$$

In the third candidate, SC_C, considering that the SC_A and SC_B are often overdetected, the number of fulfillment for the determination indices (SC_4-SC_8) is added when the SC_B is large in order to define the permeability index as expressed by Equation (11):

$$SC_C = \begin{cases} SC_B & (SC_B < 0.8) \\ \dfrac{SC_B - 0.8}{2} + 0.8 & (SC_B \geq 0.8 \cap K < T_k) \\ 0.9 \sim 1 \text{ (determined by K)} & (SC_B \geq 0.8 \cap K \geq T_k) \end{cases} \quad \cdots (11)$$

wherein K is the number of the fulfillment of SC_4 to SC_8, and T_K is its threshold. Since the parameters for indexing each score are adjusted, there is no need to adjust these parameters for each operational change; they are given in advance as fixed values.

The performance of these three types of permeability indices, SC_A, SC_B, and SC_C, has been evaluated with one year's actual operational data, which has confirmed that each index can detect all the large-scale gas channeling.[Note 2)] In addition, as shown in **Fig. 4**, it has been found that SC_C results in the smallest number of times when a threshold is exceeded, best suppressing overdetection. From this, it has been found that SC_C is the most appropriate index for the risk of gas channeling. **Fig. 5** includes charts showing the transitions of the permeability index (Index value), the pressure in the blast furnace shaft and its temperature. Since multiple sensors for pressure and temperature are disposed at each height, each chart depicts multiple pressures or temperatures. As shown in Fig. 5, the pressure fluctuation increases, which disturbs the temperature distribution, triggering the increase in the permeability index. The reason why the change in the permeability index is delayed

Note 2) Large-scale gas channeling is defined as having a blow-lowering rate of 30% or greater.

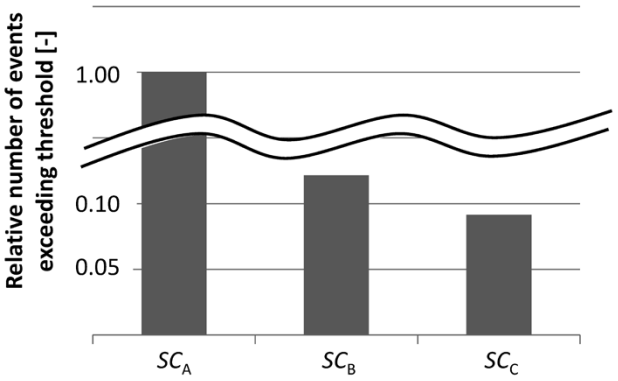

Fig. 4 Relative number of times of SC_A, SC_B, and SC_C beyond threshold (assuming 1 for the number of times of SC_A)

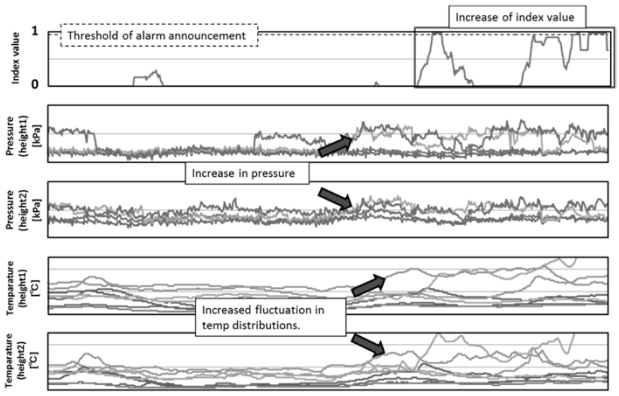

Fig. 5 Transition of index value in deteriorating furnace conditions

relative to the change in pressure and temperature is that the permeability index detects continuous fluctuation rather than the temporary fluctuation of pressure and temperature. During the period when this permeability index increases, deterioration of the raw material quality and the rise of the residual iron occurred, which verifies the fact that the deterioration of the furnace condition has been expressed.

3. Parameter adjustment technique

This section describes the technique for adjusting parameter α used for the indexing described in Section 2.2. In the case where the characteristics of the raw materials and the composition of sintered ores, etc., used in the blast furnace have changed drastically, significantly affecting the population data set and the frequency distribution obtained from them, it is important to properly adjust the parameters to accurately quantify the furnace conditions. Therefore, the frequency distribution of the target feature quantity is constantly monitored and, if there is a change, the adjustment of parameter α is performed uniformly. Distribution calculation is performed on the cases for a certain past period

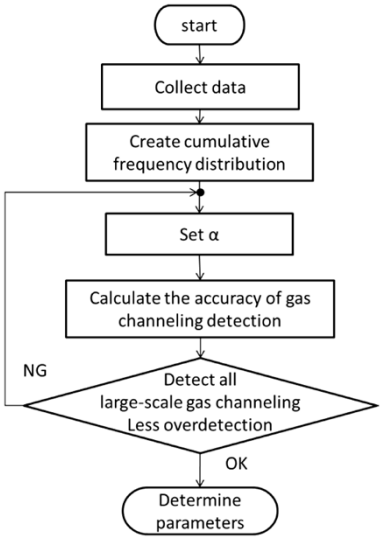

Fig. 6 Adjustment method of parameter α

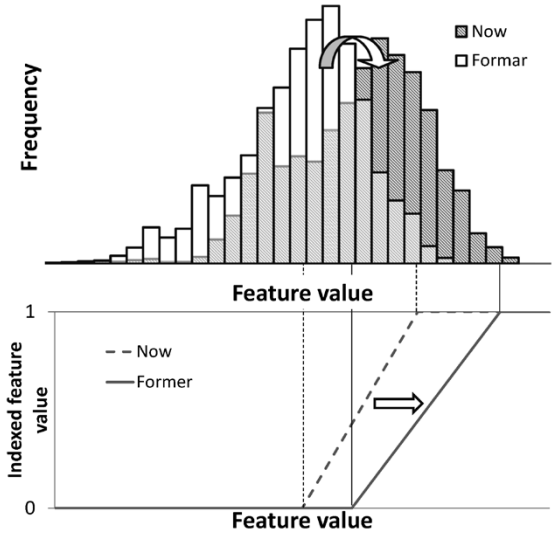

Fig. 7 Change of frequency distribution of feature quantities and method of indexing

including gas channeling incidents to adjust the parameters to optimum values so as not to overlook the large-scale gas channeling and to minimize overdetection.

This parameter adjustment technique was standardized in accordance with the flow chart shown in **Fig. 6**. A tool to automatically perform this iterative process has been developed to facilitate the parameter adjustment.

Fig. 7 shows the frequency distribution (top) obtained from two different data sets and the indexed feature determined using parameter α (bottom).

As shown in Fig. 7, when the frequency distribution changes, the indexing function changes, and the permeability index matching the change in blast furnace operating conditions can be calculated.

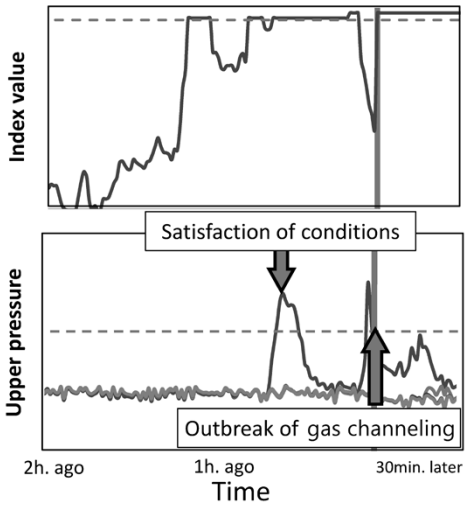

Fig. 8 Transition of index value and pressure before gas channeling

4. Evaluation of gas channeling prediction system

On the basis of the permeability index and parameter adjustment technique developed, a standard has been formulated for gas channeling prediction. That is, when performing the gas channeling preventive action, instructions are issued for "blow lowering" when the following two conditions (blow-lowering conditions) are simultaneously satisfied:

(1) the index value exceeds the threshold,

(2) the maximum pressure in the upper furnace exceeds the threshold.

As a specific example, **Fig. 8** shows the transition of the index value and upper furnace pressure upon gas channeling in the past. The blow-lowering condition has been reached before gas channeling, showing that gas channeling is prevented by preliminarily lowering the blow.

To assess the accuracy of this technology, an evaluation was performed on two aspects of data in a period not used for the parameter adjustment, i.e., to see whether there was overdetection when the blow-lowering condition had been reached, and whether there was any large-scale gas channeling had gone undetected. As a result of investigating the timing when the blow-lowering condition was reached in the data for the previous year and a half, gas channeling occurred in more than 90% of the cases. Although gas channeling did not occur in the remaining 10% of the cases, those were cases where the furnace conditions were so poor that it could have occurred, according to the operations department, so those cases were not considered to be overdetection. In addition, the blow-lowering conditions had been met before all the large-scale gas channeling occurrences, verifying the correctness

of the prediction.

Thanks to the above accuracy evaluation, the present system is now being utilized in actual operation for instructing blow-lowering timing.

Conclusions

For gas channeling, an anomaly state of blast furnaces, a gas-channeling prediction technology has been developed by quantifying the deterioration of furnace conditions, which is a background event, and by detecting the timing on the basis of furnace pressure.

This technique has enabled the prediction of gas channeling with high accuracy and is being utilized in actual equipment. In reality, the estimation of permeability deterioration in other processes relies heavily on operators, and the application of this technology is believed to enable the prediction of an anomaly state only on the basis of objective information.

References

1) M. Kase et al. *TETSU-TO-HAGANE*. 1980, Vol.13, p.148.
2) T. Aoki et al. *CAMP-ISIJ*. 1991, Vol.4, p.1340.
3) S. Yamamoto et al. *CAMP-ISIJ*. 1996, Vol.9, p.904.
4) JFE Steel Corp. OPERATION METHOD OF BLAST FURNACE. Japanese Unexamined Patent Application Publication 2017-128805. July 27, 2017.
5) M. Ito et al. *Transactions of the Society of Instrument and Control Engineers*. 2009, Vol.8, No. 10, pp.82-89.
6) K. Yamanishi. *Anomaly Detection with Data Mining*. KYORITSU SHUPPAN CO., LTD., 2009, p.45.
7) R. Yamamoto et al. *TETSU-TO-HAGANE*. 1986, Vol.10, pp.1545-1551.

Collision Warning System for Locomotives Carrying Molten Pig-iron in Kakogawa Works

Dr. Toshiharu IWATANI*1, Hiroshi KATSURA*2, Masahiro TAMURA*2

*1 Production Systems Research Laboratory, Technical Development Group
*2 Process Control Department, Kakogawa Works, Iron & Steel Business

This paper describes a collision alert system for locomotives that carry molten pig iron in the Kakogawa Works of Kobe Steel. This system comprises a process computer that stores the positional information, determined by the GPS, of locomotives along with their railroad track information in order to generate warnings. The railroad tracks laid in the steel works are more complicated than those of railroad companies and may cause various types of collisions. Hence, the railroad tracks are represented in a computer on the basis of graph theory to establish an algorithm for predicting collisions accurately and quickly. The newly developed system has been utilized continuously, promoting the safety of the locomotive operation.

Introduction

This paper describes a collision warning system (hereinafter referred to as the "present system") constructed to strengthen the safety of the locomotives running in the molten-iron treatment area of Kakogawa Works of Kobe Steel. All the locomotives in that area are equipped with GPS enabling the measurement of their positions. In addition, each driver carries an exclusive handy terminal, which makes it possible to transmit various kinds of information via wireless LAN. Hitherto, the collision avoidance of locomotives has been dependent on the driver's visual attention. The development of the present system aims at realizing safer locomotive operations by utilizing the above information equipment.

This paper is organized as follows: Section 1 outlines the locomotive logistics in the molten-iron treatment area and describes the expression method using symbols and two types of collisions that are important subjects in the collision avoidance problem of the locomotives (hereinafter referred to as "the present problem"). Section 2 introduces collision prevention technologies for various vehicles and shows that the collision prevention technologies for automobiles and aircraft cannot easily be applied to the present problem. Section 3 introduces two issues specific to the present problem through comparison with the automatic train control applied to ordinary railways. Lastly, Section 4 shows the method for solving the problems and the algorithm that has been developed.

1. Locomotive logistics in molten-iron treatment area of Kakogawa Works

1.1 Outline of subject logistics

In the Kakogawa Works of Kobe Steel, molten iron is tapped off from a blast furnace at about 1,500°C and charged into a torpedo car (hereinafter referred to as a "torpedo") to be transported to a molten-iron treatment plant or other area by diesel locomotives. The molten iron is transferred into a pot in the molten-iron treatment plant; and the now-empty torpedo, slag and metallic adhesions having been removed, is sent to the blast furnace for a repeated charging of molten iron. The term, "molten-iron treatment area," refers to an area to which molten-iron is transported.

Fig. 1 outlines the processes carried out in the molten-iron treatment area. The transportation time for molten iron affects the energy cost and iron & steel yield, and the efficiency of logistics is important. To this end, various measures have been attempted.[1] Meanwhile, the damage caused by molten iron leakage in the event of an accident would be enormous, and ensuring safety is of utmost importance as a major premise for efficiency.

The locomotive railway track laid in the molten-iron treatment area has a total extension of about 25 km, and there are approximately 100 junction/branching points (hereinafter referred to as (a) "branch(es)"). The locomotives are operated at speeds less than 10km/h, which is slower than those

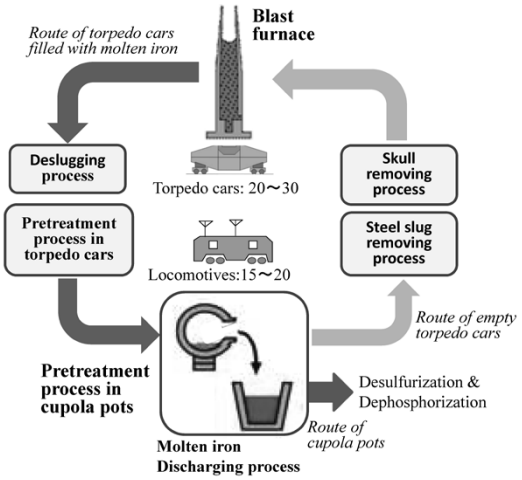

Fig. 1 Outline of molten-iron treatment area

of the ordinary railway.

1.2 Railway tracks in molten-iron treatment area and their expressions

Fig. 2 depicts the actual railway track in the molten-iron treatment area. In the figure, the solid circles, ●, indicate branches (i.e., bifurcation points, hereinafter referred to "BPs"), and the pentagonal marks indicate locomotives (hereinafter referred to as "LMs"). The tip of each pentagonal mark indicates the traveling direction of the respective locomotive.

The study in this paper uses symbols to represent the railway track, which has such a complicated shape (**Fig. 3**). A branch is represented by a lowercase letter, a, b, c, and the railway tracks between branches (called Zones) are indicated by straight lines and labeled Zone A, Zone B, and so on. The starting points and ending points (hereinafter "EPs") of the railway track are not branches in a strict sense, but are treated as branches for simplicity of discussion.

Not all the zones that touch a branch are mutually transferable. For example, in the branch shown in Fig. 3, Zones A, B, and D are connected, and a locomotive can move from Zone A to both Zones B and D. It is also possible to move from Zone B or Zone D to Zone A. However, movement from Zone B to D, or from Zone D to B would require a sharp turn at a branch and is impossible. In order to predict the collision of two locomotives, it is necessary to derive the branches and zones that are reachable for the locomotives after satisfying this restriction.

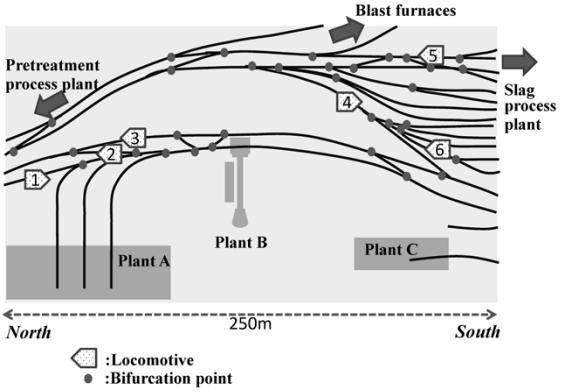

Fig. 2 Part of railway track map in Kakogawa Works

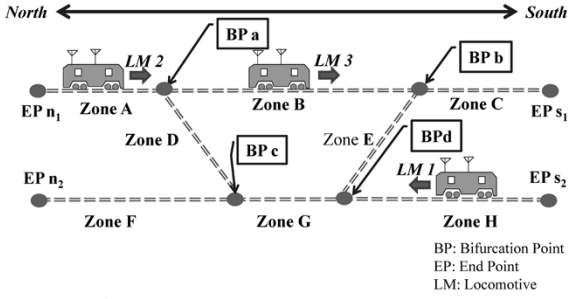

Fig. 3 BPs, EPs and Zones in rail track map

1.3 Two types of collisions involved in the present problem

In collision prediction for the ordinary railway, in which trains are traveling in the same direction on the same railway track, focus is placed on the prevention of rear-end collisions, in which a following train collides with one in front. For the present problem, two types of collisions, in addition to rear-end collisions, provide important solution tasks, as described in this section.

Two running directions are defined for the locomotives in the present problem, the "north bound" and "south bound," which are similar to the inbound and outbound in an ordinary railway. However, even if there are multiple railway tracks traveling in parallel as shown in Fig. 2, there is no provision for the north bound only, or south bound only, as in the case of an ordinary railway, and all railway tracks allow travelling in both directions. Therefore, there is a risk of frontal collision with Locomotives 4 and 6 in Fig. 2.

Also, the railway track in the molten-iron treatment area has branches at short intervals of several to several tens of meters. At a branch, a locomotive may come in from another railway track. In the case of Fig. 2, Locomotives 2 and 3 may collide at the junction.

Appropriate alarm generation for the above two types of collision is an important issue in the present problem.

2. Comparison with existing collision avoidance technologies

2.1 Outline of existing collision avoidance technologies

Collision avoidance and warning technologies for general transportation vehicles have been studied for a long time, mainly on aircraft and trains. The automatic driving technology for passenger cars also includes collision avoidance technology. These technologies have been developed independently, since there are significant differences in the degree of freedom of the traveling route of the target transportation vehicles, and in their collision avoidance targets. The outlines of those technologies are shown in **Table 1**, and the applicability of each technology to the present problem has been examined.

Table 1 Types of technology for collision avoidance

Target	Directions	Collision avoidance targets	Collision avoidance methods
Airplane (TCAS)	3 dimensions	Airplanes (limited)	Change direction, altitude (limited)
Automobile (Automated Driving System)	2 dimensions	Man, car and building (many types)	Breaking, Change direction, etc.
Trains (ATS)	1 dimension	Trains on the same railway (very limited)	Breaking (limited)
Locomotive in steel works(Our developed system)	1 dimension (with many branches)	Locomotives in the same area	Breaking (limited)

2.2 Applicability of aircraft collision warning technology to the present problem

In Japan, each aircraft with more than 20 seats is required to be equipped with a traffic alert and collision avoidance system (TCAS) to prevent aerial collisions.[2] Aircraft carrying TCAS mutually recognize each other's positions. An alert is issued when a possible collision is identified from such information as distance, altitude, and navigational direction.

A similar warning system may be established for the locomotives in the molten-iron treatment area, since they all collect and record positional information with GPS. In the present problem, however, there are cases where it is impossible to properly determine the possibility of collision solely from the distance and travel directions of other vehicles.

Among the three locomotives shown in Fig. 3, LM1 is north bound, and LM2 and LM3 are south bound. There is a possibility that LM1 in Zone H will move to Zone G, and even to Zone D. At this time, if LM2 in Zone A also enters Zone D or Zone G, it may collide head-on with LM1. Meanwhile, the only reachable zone for LM3 in Zone B is Zone C (Zone E is not reachable because of the acute angle turn.), and there is no possibility of LM3 colliding with LM1. In other words, LM1 has a risk of colliding with LM2, which is at a greater distance, rather than with the nearby LM3. Thus, the collision determination method focused on distances that is used for locomotives is inadequate as a solution for the present problem, in which the moving range is restricted by the railway track.

2.3 Applicability of automatic driving technology for passenger cars to the present problem

The automatic driving technology for passenger cars has evolved remarkably in recent years,[3] and it is envisaged that automatic driving on public roads will be realized within a few years in Japan. As shown in **Table 2**, the automatic driving technologies are classified into 5 levels. In this classification, only level 3 or higher is called automatic driving technology, and the levels below it are regarded as driving support technology.

First, the difference between driving support technology and automatic driving technology is outlined. Driving support technology of level 2 or below recognizes obstacles from images in the traveling direction and, from the recognition results, determines the possibility of a collision accident, whereas the automatic driving technology of level 3 or higher comprises highly accurate 3D map information in addition to obstacle recognition. In addition to the static information, it also has a digital map that integrates time-varying information, such as traffic jam information and vehicle position and progress information, in addition to information on road traffic laws and traffic regulations. Such maps are called "dynamic maps" and are being developed on a national level because the development task involves highly complicated, large-scale technology.[4] By integrating the spatial (railway track, road, etc.) recognition technology making use of the information and the aforementioned image recognition results, accurate collision risk recognition is realized, enabling automatic driving.

Now, a case is considered where the driving support technology or automatic driving technology is applied to the situation shown in **Fig. 4**. In the molten-iron treatment area, there are many places in which two curved railway tracks, as shown in Fig. 4, are laid almost in parallel. When two locomotives

Table 2 Definition of automatic driving technology

Level	Name	Execution of steerling, acceleration, and deceleration	Monitoring of driving environment	Fallback performance of dynamic driving task	System capability (driving mode)
0	No Automation	Human driver	Human driver	Human driver	n/a
1	Driving Assitance	Human driver and	Human driver	Human driver	Some driving modes
2	Partial Automation	System	Human driver	Human driver	Some driving modes
3	Conditional Automation	System	System	Human driver	Some driving modes
4	High Automation	System	System	System	Some driving modes
5	Full Automation	System	System	System	Full driving modes

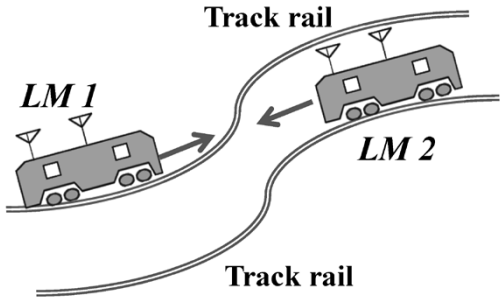

Fig. 4 Example of possible situation of false warning

pass each other at such a place, there is no risk of collision, since the locomotives travel on different railway tracks. However, if the two locomotives were equipped with driving support technology, it is highly likely that each locomotive would recognize the other in front of it and in its direction of travel, erroneously determining a risk of collision. On the other hand, an automatic driving function, if implemented, can refer to the information of the dynamic map and recognize that the other, oncoming locomotive is running on another railway track, determining that there is no risk of collision.

The image processing technology that recognizes obstacles for driving support is certainly applicable to the present problem. However, in order to realize the dynamic map, which is the core of the automatic driving technology, it is necessary to keep renewing various sorts of information accurately in real time, and it is not easy for Kobe Steel to accomplish this alone.

In this way, it is difficult to extract a part of the automatic driving technology and apply it directly to the present problem. Hence, it is considered necessary to develop a level of technology intermediate between driving support technology and automatic driving technology and specialized for the present problem.

3. Comparison with ATC and realization of problem-solving method for the present problem

In order to consider the mechanism for displaying and sounding appropriate collision warning using the information on the connection branches and zones in railway track, an overview of the automatic operation technology for railway follows.[5), 6)]

Japan's first system for automatically stopping vehicles on railway track was introduced in the 1950s as automatic train stop (ATS). There is a system, Automatic Train Control (hereinafter "ATC"), which is similar to ATS, and it is difficult to strictly distinguish between them. The former is a system that performs an auxiliary brake operation when the driver misses an existing ground signal, whereas the latter system constantly monitors the vehicle speed and intervenes in the brake operation when the speed limit derived in accordance with each zone is exceeded. Thus, ATC is regarded as a more sophisticated function, and only ATC is considered in the comparison made here.

3.1 Fixed block ATC and moving block ATC[7)]

There are two types of ATC, namely, a fixed block system and a moving block system. **Fig. 5** (a) shows an example of the fixed block system realized in the 1960s. The railway track is divided into zones in advance. When there is a vehicle in Zone A, the locomotive in adjacent Zone B is slowed down and prohibited from entering Zone A. The upper speed limit for Zone C in the rear is set at 20 km/h, and the upper speed limit for Zone D, further to the rear, is set at 50 km/h. There is no special control for Zone E and beyond. Each zone provided for performing a different control is called a "blocked zone," and the fixed block system is so called because the control is performed with the blocked zones fixed.

The fixed block system ensures the avoidance of rear-end collisions. In this case, however, other locomotives in Zone B are not allowed to enter Zone A, regardless of where the locomotive in Zone A is located, and this hinders the efficient operation of locomotives. In order to solve this problem, a technique is needed to eliminate fixed zones and find the distance between vehicles on the basis of

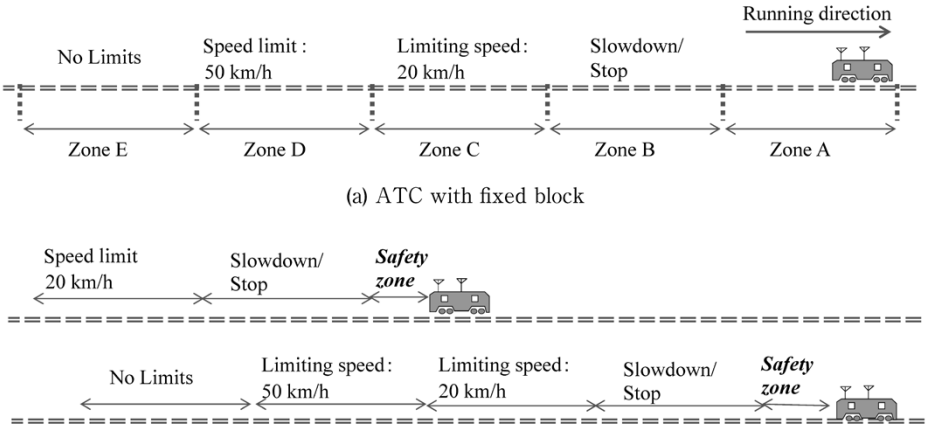

Fig. 5 Examples of ATC system

the position of each locomotive, which changes from time to time, so as to control the following locomotive. It was the moving block ATC that realized such control in the 2000s.[7] As shown in Fig. 5 (b), a safety zone is dynamically set in the immediate rear of the locomotive in accordance with its movement, prohibiting other locomotives from entering said zone and, in addition, speed control is performed on the following zones. In this way, the moving block system keeps the distance between locomotives shorter than does the fixed block system, while securing safety.

However, the moving block system needs to accurately grasp the locomotive positions with no delays. In the molten-iron treatment area, it is not easy to thoroughly, unfailingly and accurately grasp the positions using GPS, due to the radio disturbance caused by the building for large equipment. Therefore, the moving block system ATC is regarded to be as infeasible.

3.2 Function for searching branches and zones with potential collision risks

In the railway where ATC is used, all the zones are set to be of almost equal length. This enables safety to be secured by speed control based on the number of zones to the rear of the locomotive, as shown in Fig. 5(a), whereas the railway track that is the subject of this study (Fig. 2) has inter-branch zone lengths greatly varying from several to several hundreds of meters. Therefore, the possibility of collision cannot be determined only by the number of zones between the following locomotive and the one in the forefront.

Accordingly, it is necessary to derive all zones and branches reachable within a certain time for each locomotive on the basis of the branch/junction information for the railway track. Furthermore, if there is a zone/branch that is reachable by multiple locomotives, this is regarded as a collision risk and as an object of warning or an advisory, one rank lower.

3.3 Dynamic function applying warning algorithm

For locomotive collision warning in the molten-iron treatment area, the possibility of two locomotives colliding cannot be determined merely from their respective zones. The reasons are described below:

Each car carrying a torpedo has no GPS, and only the position of the locomotive is collected. Hence, if torpedo cars are connected, it is necessary to correct the position for the length of the torpedo cars with respect to the positional information of the locomotive. There are two ways of connecting torpedo cars with a locomotive for transportation; i.e., a towing connection, in which the torpedo cars are connected to the rear of a locomotive, and a pushing connection, in which torpedo cars are connected to the front of a locomotive (**Fig. 6**).

The length of a torpedo car falls in the range of 20 to 30 m depending on the type, and multiple cars may be connected. Since a collision usually occurs near the head of a train, it is important to grasp that position. Hence, no positional correction is required for a towing connection; however, a pushing connection requires a positional correction of several tens of meters. The distance corresponding to the length of the torpedo cars in the traveling direction of a locomotive is herein called a "correction distance."

In addition, as with automobiles, each locomotive has a braking distance, and even if braking is applied, the locomotive will not at once stop completely. The braking distance changes depending on the speed of the locomotive, the weight of the torpedo cars during transportation, and/or the weather, and the difference can reach several tens of meters. Hence, the braking distance must be corrected in accordance with the circumstances.

3.4 Two types of collision avoidance

As described in Section 1.3, there are two typical patterns of collision that may occur due to the present problem. One is the case where two locomotives with different traveling directions (travelling face to face) cause a frontal collision in a zone, as shown in **Fig. 7** (a): this is hereafter called "zone collision." The other is the case where two locomotives traveling on different railway tracks towards a branch collide in the vicinity of the branch (Fig. 7(b)): this is hereafter called "branch collision." For these two types of collisions, different methods must be applied to determine the collision possibilities.

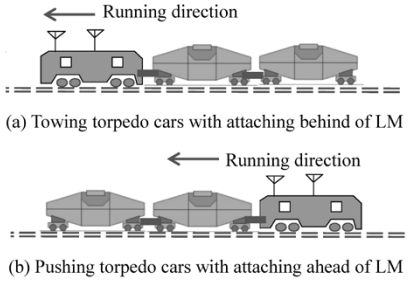

Fig. 6 Two ways to transport torpedo cars

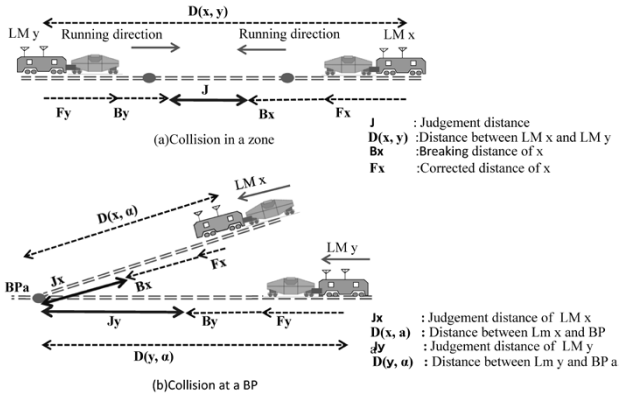

Fig. 7 Two types of locomotive collisions

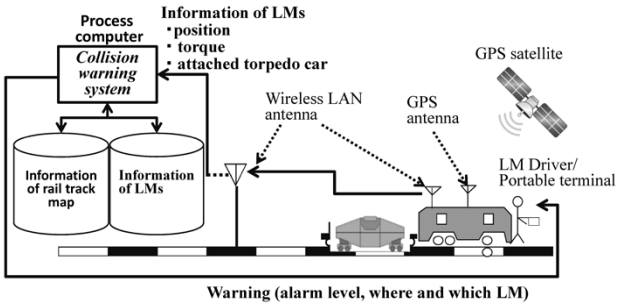

Fig. 8 Hardware configuration of developed collision warning system

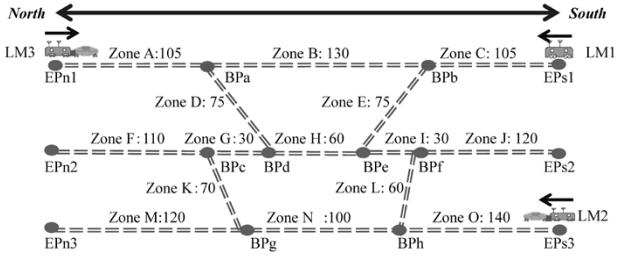

Fig. 9 Example of collision determination

4. Method of realizing collision warning system

4.1 Hardware configuration

As described in the previous sections, the determination of collision requires varied information on each locomotive. It is also necessary to indicate the result of collision risk determination to the locomotive drivers. **Fig. 8** shows the configuration of the hardware providing the foundation to do this.

The vehicle information on the position acquired from the GPS, direction, and transmission, as well as the information on the condition of the torpedo car connections, towing or pushing, is transmitted from the wireless LAN antenna of each locomotive. These pieces of information are received by ground antennas installed at several locations in the molten-iron treatment area and sent to the process computer for molten-iron logistics. The process computer holds all locomotive and railway track information in the molten-iron treatment area. From these two types of information, the collision risk of each locomotive is determined, and necessary display and sound warnings are given by the handy terminal carried by each locomotive driver.

4.2 Software configuration

The following describes, with examples, a method for implementing the function necessary to solve the present problem, described in Sections 3.2 - 3.4. **Fig. 9** is a symbolic representation of a railway track consisting of 14 branches and 15 zones. The number paired with each zone name indicates the zone length (unit: m). Three locomotives are assumed to be in service. In the initial state, LM1 is north bound and located at EPs1 without any torpedo car connected. LM2 is north bound with one torpedo car connected to its front (north side) and is located at EPs3, while LM3 is south bound with one torpedo car connected to its front (south side) and is located at EPn1. For convenience of explanation, all the locomotives are assumed to be initially located on branches; however, the argument in this section can readily be extended to cases where the initial locations are in the zones.

4.2.1 Preliminary calculation of inter-branch distances

As described in Section 3.2, the present problem requires the derivation of which zone and branch are reachable for each locomotive, and what is the shortest distance to reach it. Since the connection information for the railway track is predetermined, the reachability and shortest distance for each inter-branch can be calculated in advance.

The branches reachable for LM1-LM3 in Fig. 9 and the shortest distances are shown in the third column of **Table 3**, and the reachable zones are shown in the fourth column of Table 3. LM1 can reach branch BPa via Zones C and B, or it can reach the same via Zones E, H and D. The distance of the former route, which is shorter, is adopted. This example is simple, and the determination of the shortest distance is easy. However, the actual railway track in the molten-iron treatment area is so complicated and large that intuitive determination is impossible. In graph theory,[8] there are algorithms,[9) 10)] such as Dijkstra's algorithm,[11)] that can facilitate calculation, shortening the time.

Table 3 Present position, direction and reachable BPs and Zones of each LM

LM	Position/ Direction	Reachable BPs and Distances	Reachable Zones
LM1	EP s1/ Northbound	(s1, 0), (b, 105), (a, 235), (n1, 340), (e, 180), (d, 240), (c, 270), (N2, 380)	C, B, A, E, H, D, G, F
LM2	EP s3/ Northbound	(s3, 0), (h, 140), (g, 240), (N3, 360), (c, 310), (n2, 420)	O, N, M, K, F
LM3	EP n1/ Southbound	(n1, 0), (a, 105), (b, 235), (s1, 340), (d, 180), (e, 240), (f, 270), (s2, 390),	A, B, C, D, H, E, I, J

4.2.2 Collision possibility of each locomotive

The following describes the method for deriving the collision probability of the three locomotives in Fig. 9 using the information in Table 3. First, the combinations of locomotives that require verification on the occurrence of zone collision, i.e., the combinations of locomotives having different traveling directions, are LM1 & LM3, and LM2 & LM3. In the case of the former combination, there are many reachable zones, such as A, B, C, D, H, and E, shared by both locomotives and there are possibilities of zone collision, whereas in the latter combination, no reachable zone is shared, and it can be determined that there is no possibility of zone collision.

Next, the combinations of locomotives are considered in order to verify the occurrence of branch collision. The combination of locomotives traveling in the same direction is LM1 & LM2, and there is the possibility of collision in the reachable branch (BPc, EPn2) shared by the two locomotives. If the common reachable branch is none, it is determined that there will be no collision.

4.2.3 Determining the necessity of warning

The previous section described the occurrence possibility of zone collision between LM1 and LM3 and branch collision between LM1 and LM2. This section describes the algorithm for determining the necessity of warning.

First, the determination method of zone collision (Fig. 7 (a)) is shown. Once the positions of locomotives on the railway track are known, the distance D(x, y) between them can be derived using Table 3. Furthermore, the corrected distances, Fx, Fy, of LMx and LMy, respectively, are determined on the basis of the torpedo car connection information, and the braking distances Bx, By are also derived from the transmission information for each locomotive and the torpedo car connection information. It should be noted that these distance data are tabulated for quick determination.

Using the above data, the determination distance J is calculated by Equation (1):

$$J=D(x, y)-(Fx+Bx)-(Fy+By) \quad \cdots\cdots (1)$$

This determination distance J is compared with preset thresholds, L_1 and L_2 ($L_1 < L_2$), and if it is smaller than L_1, a "Warning" for a high degree of risk is declared, while, if $L_1 < J < L_2$, an "Advisory" milder than "Warning" is declared. Here, L_1 and L_2 are determined on the basis of the distance assumed to be traveled before the locomotive driver notices the warning (or advisory) and activates the brake, as well as the error of the position information obtained by GPS.

Next, the method of determining branch collision (Fig. 7 (b)) is described. Even when there is a possibility of collision at more than one branch, it should be sufficient to consider only the possibility of collision at the branch closest to both locomotives (BPc in Fig. 9). The algorithm of this determination is explained on the basis of Fig. 7 (b). In the case of branch collision, both distances D (x, α) and D (y, α) between the branch position (in this case BP α) and the two locomotives are derived. Then, the determination distances for the respective two locomotives are calculated by Equation (2):

$$\left.\begin{aligned} Jx&=D(x, \alpha)-(Fx+Bx)\\ Jy&=D(y, \alpha)-(Fy+By)\end{aligned}\right\} \quad \cdots\cdots (2)$$

In the case of branch collision determination, three thresholds, K_1, K_2, and K_3 ($K_1 < K_2 < K_3$), are used, and the degrees of risk, P_x and P_y of LMx and LMy, respectively, are classified into four levels using the determination distance (Equations (3), (4)). The larger the value, the greater the risk that a branch with collision risk is located nearby. As in the case of L_i, K_j is determined to take into account the distance travelled before the driver notices the alarm and GPS error.

$$\left.\begin{aligned} P_x&=3 \ (\text{when } Jx<K_1)\\ &=2 \ (\text{when } K_1<Jx<K_2)\\ &=1 \ (\text{when } K_2<Jx<K_3)\\ &=0 \ (\text{when } K_3<Jx)\end{aligned}\right\} \quad \cdots\cdots (3)$$

$$\left.\begin{aligned} P_y&=3 \ (\text{when } Jy<K_1)\\ &=2 \ (\text{when } K_1<Jy<K_2)\\ &=1 \ (\text{when } K_2<Jy<K_3)\\ &=0 \ (\text{when } K_3<Jy)\end{aligned}\right\} \quad \cdots\cdots (4)$$

On the basis of the combination of P_x and P_y, a warning/advisory report, and display/sound are determined. With this logic, if either P_x or P_y is 0, for example, no display / no sound is determined upon (there is no risk of branch collision), and if both are 2 or greater, an alarm is issued. This determination method is also tabulated in the system.

Fig.10 Alert message displayed on handy terminal

The warnings and advisories derived by the above logic are displayed on handy terminals carried by locomotive drivers. An example of the display screen is shown in **Fig.10**. This screen alerts the driver of Locomotive 217 that there is a risk of frontal collision with Locomotive 210.

Conclusions

This paper has outlined the warning system constructed for the collision problems of the locomotives travelling in the molten-iron treatment area of the Kakogawa Works of Kobe Steel. There are many technologies for detecting the collision possibility of transportation vehicles and the technologies for automatic driving. This paper has described why diverting these technologies cannot help with the present problem. Also introduced is the existence of many branches featuring in the logistics of the molten-iron treatment area, and an algorithm implemented to respond to the need for dynamically changing the collision determination logic.

The present system operates on real machines, and each locomotive driver refers to the warnings indicated on the handy terminal to realize safer and more secure operation. It is expected that this function will be extended to create safe and efficient routes and so on.

The automatic driving technology and driving support technology of transportation vehicles used in public areas are expected to progress steadily in the future. However, as described in this paper, there are many pieces of transportation equipment that are operated under special conditions on production work sites where general automatic driving technology cannot easily be applied. Even within steelworks, there are, for example, large special vehicles that transport semi-products and waste, and overhead cranes in the plants. We will strive to extend this development experience to benefit driving support and automation for these machines.

References

1) H. Tamaki et al. *TETSU-TO-HAGANE*. 2014, Vol.100, No.4, pp.485-490.
2) T. Inagaki. *The Institute of Electronics, Information and Communication Engineers, Engineering Sciences Society, Fundamentals Review*. 2008, Vol.2, pp.22-30.
3) T. Kurashiki. *NTN Technical Review*. 2017, No.85, pp.2-13.
4) H. Takada et al. *Transactions of the Institute of Systems, Control and Information Engineers*. 2016, Vol.60, No.11, pp. 457-462.
5) T. Mizuma. *Journal of the Society of Instrument and Control Engineers*. 2017, Vol.56, No.2, pp.93-98.
6) H. Arai. *RRR (Railway Research Review)*. 2008, Vol.65, No.07, pp.22-25.
7) S. Konno. *Transactions on Electrical and Electronic Engineering*. 2010, Vol.130, No.8.
8) R. J. Wilson. *Introduction to Graph Theory*. Addison Wesley Longman Ltd., 5th Edition (2012).
9) H. Terada et al. *Japanese Unexamined Patent Application Publication* 2014-210570.
10) H. Terada et al. *Japanese Unexamined Patent Application Publication* 2014-210571.
11) K. Ishihata. *Algorithms and Data Structures*. Iwanami Shoten, Publishers., 1989.

Development of Prediction Technique for Temperature Distribution of Molten Steel in Steelmaking

Dr. Nobuyuki TOMOCHIKA*1, Dr. Takehiro NAKAOKA*2, Takehiro TSUKUDA*3, Yoshiyuki NAGASE*3, Hiroshi KATSURA*4, Kazuki SUMIDA*5

*1 AI Promotion Project Department, Technical Development Group
*2 Mechanical Engineering Research Laboratory, Technical Development Group
*3 Research & Development Laboratory, Iron & Steel Business
*4 Process Control Development, Kakogawa Works, Iron & Steel Business
*5 Steelmaking Department, Kakogawa Works, Iron & Steel Business

To promote the transfer to younger workers through operation support, a technique has been developed to present, in a probability distribution, the deviation risk for molten steel temperature in the converter furnace, molten steel treatment, and continuous casting steps involved in processing. This technique constructs a probability distribution by converting and transferring massive amounts of recorded data concerning past performance into information corresponding to the current operational state. It is based on a physical model, weighing the information in accordance with the degree of similarity. Its advantages are that calculable factors are separated from uncertain factors in a deterministic manner, the time change of the uncertain factors is taken into account on the basis of thermal influence, and Just-In-Time modeling is applied, which enables the systematic calculation of the probability distribution even for different conditions of such factors as steel types and facilities. This technique has been applied to an actual steelmaking process, which has reduced the deviation of casting temperature from the target value to less than half of the conventional one.

Introduction

The number of skilled operators is decreasing at production work sites such as steelworks, and it is urgent to transfer their skills to younger operators. There is an increasing need for an operation support system effective not only in maintaining work standards and documenting explicit knowledge, but also in making tacit knowledge into explicit knowledge to be inherited.

Meanwhile, the prevalence and progress of ICT have enabled the collection and utilization of large amounts of data, a task that is conventionally inconceivable; and various systems have been developed on the basis of large-scale operational data in the past, such as Just-In-Time (JIT) modeling.[1), 2)]

It is against this backdrop that Kobe Steel has been focusing on the development of operational support systems applying JIT modeling technology.[3),4)] These systems are not limited to the mere listing of actual data and visualization of trends, but have the following features; (A) selecting and emphasizing cases with high similarity from past data, (B) converting the data into virtual experience information corresponding to the on-going operational state on the basis of physical models, (C) presenting the images in the heads of experts as visual information to complement the experience of younger operators, and (D) supporting their appropriate decisions and actions.

This paper focuses on the complex logistics of transferring molten steel in ladles among converter furnaces and continuous casting machines in the Kakogawa Works of Kobe Steel and describes a method for predicting the probability distribution of molten steel temperature and a system for presenting such information to operators to support accurate temperature management.

1. Background and purpose of this technical development

After being blown at a converter furnace, molten steel is transferred to a ladle and transported to molten steel processing equipment (e.g., RH furnace). After the completion of molten steel treatment, the ladle is transported to continuous casting equipment, and molten steel is poured from the bottom of the ladle into a tundish (**Fig. 1**). At this time, too high a molten steel temperature increases the risks of, among others, breakout, cracking and segregation during casting. On the other hand, too low a molten steel temperature may result in the clogging of immersion nozzles and/or a failed ladle opening. For the purpose of avoiding those risks, the temperature of molten steel is kept higher than the target value and, when it is too high, the casting speed is lowered to cope with this. Such measures, however, can adversely affect heating cost and productivity. Therefore, keeping the temperature of molten steel in a tundish within a more appropriate range is indispensable for realizing stable operation.

In the Kakogawa Works, multiple apparatuses for molten steel treatment and continuous casting are arranged in a plurality of steel plants in order to produce various types of steel materials, intertwining the logistics of molten steel in a

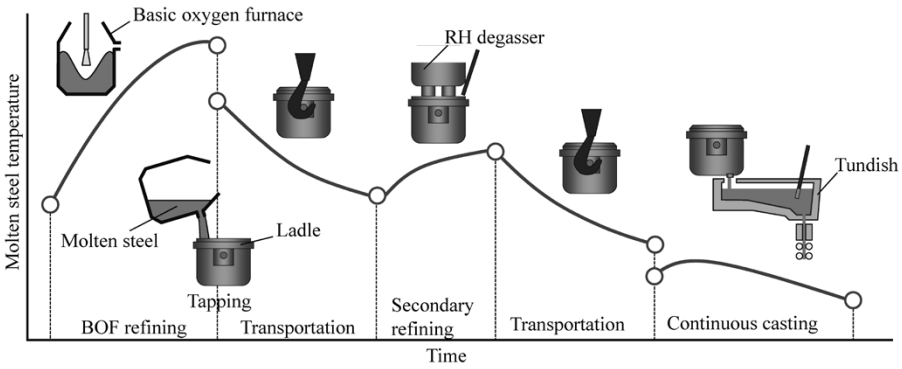

Fig. 1 Outline of steelmaking process and change of molten steel temperature

complicated manner. Hence, it is very difficult to manage, without interruption, the molten steel in a tundish within the specified temperature range in accordance with the operation schedule, which changes from time to time.

In such circumstances, the continuous casting operators, for example, input the correction values for the target temperature of the next molten steel to be transferred from the molten steel processing step even before it is subjected to the molten steel treatment. At this time, adjustments are made so that the molten steel temperature (and eventually the casting temperature) after the transfer falls within a predetermined range, taking into account the casting temperature management range and operation schedule information.

Hence, efforts have been made to predict the molten steel temperature during ladle transportation and in tundish on the basis of theories using various data.[5), 6)] It is not possible, however, to measure the refractory temperatures of the ladle and tundish, making it difficult to accurately predict the molten steel temperature. With the temperature being unpredictable, it would be beneficial for the operators to be provided with information as to whether there is a high risk that the actual temperature will deviate to the higher side of its predicted value, or whether there is a high risk that it will deviate to the lower side. In fact, interviews with skilled operators have revealed that they imagine in their heads something like probability distributions of molten steel temperature to recognize the risk of deviation from the predicted temperature.

Therefore, an attempt has been made to support accurate decision making by the operators by presenting the variation of molten steel temperature as a probability distribution in accordance with the operating conditions, rather than predicting the molten steel temperature at only one point. Although there are other studies on temperature distribution,[7)] the present technological development is characterized by JIT modeling that allows flexibility in handling different steel types and processes and by the consideration of the difference in the thermal influence factor.

2. Skilled operator's view

When predicting the deviation risk of molten steel temperature, skilled operators do not necessarily recall all the past cases equally. They retrieve examples close (highly similar) to the on-going operating conditions from their memories, make corrections for the difference between the past conditions and the on-going operating conditions, and replace (transfer) them with on-going conditions before their recognition. In other words, they recognize each past case by converting it into virtual experience information corresponding to the on-going operating condition. At that time, the skilled operators separate factors with clear cause-and-effect relationships (behaviors regarded as criteria for modeling in a deterministic way) from uncertain factors (variability that can be considered statistically) to interpret the temperature change.

As an example, in a past case where the operating conditions were similar to those of the on-going charge, it is assumed that the molten steel temperature was 10°C below the target value when the transport time after molten steel treatment was 20 minutes. If the transport time for the on-going charge is 30 minutes, there will be two ways of interpretation; one is that the molten steel temperature will drop as much as the 10-minute increase of the transport time, and the other is that, since the temperature was 10°C lower than the target value for the transport time of 20 minutes, the transport time of 30 minutes will cause a more significant deviation. The former corresponds to factors with physically clear causal relationships; the latter, to uncertain factors.

Skilled operators predict the change in time series (reference line) of molten steel temperature from

the former point of view and replace the variation of similar past cases (deviation from the reference line) with the on-going conditions from the latter viewpoint. Then, they stochastically grasp the temperature deviation risk by weighting the past cases on the basis of their similarity with the on-going operational state.

3. Outline of procedure for predicting probability distribution of variation in molten steel temperature

3.1 Basic concept

In accordance with the skilled operators' view described in the previous section, the probability distribution of variation in molten steel temperature is calculated by the following steps (A) to (E). For simplicity of explanation, this and the following sections describe the example of molten-steel temperature distribution calculation during ladle transportation from the converter furnace to the molten steel treatment.

(A) Calculating the variation of molten steel temperature (the deviation from the reference line) in past charges. Here, the deviation from the upper limit line of the temperature based on the theoretical model is defined as a variation.

(B) Mapping the temperature variation of each past charge for the predicted time of the on-going charge in consideration of the thermal influence factor.

(C) Transcribing the variation after mapping on the basis of the upper limit line of the on-going charge.

(D) Weighing the value of each temperature variation after transcription in accordance with the degree of similarity between each past charge and the on-going charge.

(E) Constructing a weighted histogram and a probability distribution therefrom by normalizing the area to be 1 so as to grasp the temperature variation risk.

Of the above, (A) to (C) are views based on the theory of physical phenomena, while (D) and (E) are stochastic and statistical views. The deterministic part consists of a view based on physical phenomenology, and the probabilistic part is constructed with a statistical model.

3.2 Specific calculation procedure

The specific procedure to calculate the probability distribution of variation in molten steel temperature will be explained with reference to **Fig. 2**.

[Step (A)] First, in the i^{th} past charge (i = 1 to N), the molten steel temperature $T_i(t)$ at time t is expressed by the sum of the reference line (upper limit line of temperature drop calculated from physical model[5]), $f_i(t)$, and error factor $\Delta_i(t)$ (Equation (1)):

$$T_i(t)=f_i(t)+\Delta_i(t) \quad \cdots\cdots (1)$$

Then, the error $\Delta_i(t_i)$ at the time, t_i, of temperature measurement is expressed by Equation (2):

$$\Delta_i(t_i)=T_i(t_i)-f_i(t_i) \quad \cdots\cdots (2)$$

[Step (B)] The error $\Delta_i(t_i)$ is time-mapped and converted into a value $\Delta_i(t_0)$ corresponding to the predicted time t_0 of the on-going charge.

[Step (C)] The error $\Delta_i(t_0)$ is added to the molten steel temperature reference line $f_0(t)$ of the on-going charge calculated by the physical model, thereby obtaining a point, $T_{0i}(t_0)$, constituting the temperature variation of the on-going charge at the predicted time t_0.

$$T_{0i}(t_0)=f_0(t_0)+\Delta_i(t_0) \quad \cdots\cdots (3)$$

[Step (D)] For each past charge, $T_{0i}(t_0)$ is calculated. Following the rule of thumb that the deviation from the reference line is similar if the operating conditions are similar, the similarity between the on-going charge and each past charge is made to

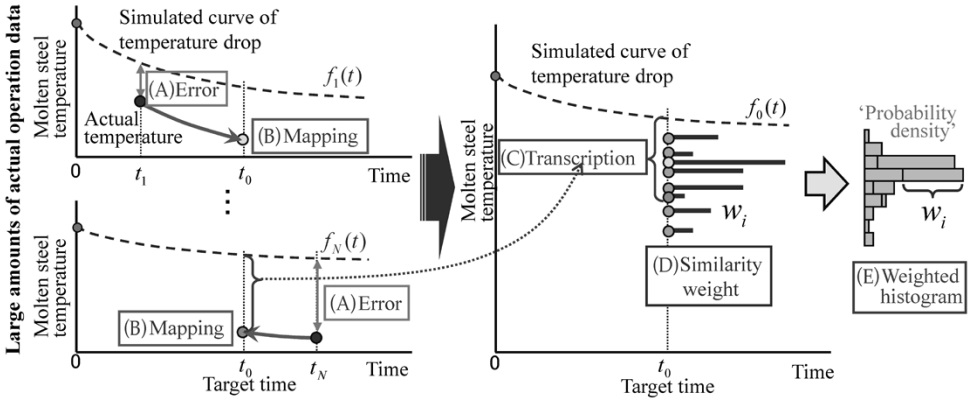

Fig. 2 Outline of calculation method for probability distribution of molten steel temperature

correspond to each temperature, $T_{0i}(t_0)$.
[Step (E)] A histogram weighted by similarity is constructed, and the one whose area is normalized to be 1 is presented to the operators.

4. Construction method of probability distribution considering factors of molten steel temperature variation

The main subject in the series of procedures described in the previous section is how to map the value of the error $\Delta_i(t_i)$ to calculate the value of $\Delta_i(t_0)$ in Step (B). In other words, the subject is how to determine the change in the value of the error $\Delta_i(t_i)$ in the time axis direction. The following describes an example of calculating the temperature variation during ladle transportation.

4.1 Variation factor during ladle transportation

In the ladle transportation from the converter furnace to the molten steel processing equipment, the three factors affecting the temperature variation are summarized as follows (**Fig. 3**).

(a) Variation of initial molten steel temperature
(b) Variation of initial refractory temperature
(c) Variation of heat transfer coefficient

Factor (a) is attributable to an error of temperature measurement at the time (t=0) when the steel is discharged from the converter. This is a view stating, "The initial value of molten steel temperature in the i^{th} past charge was measured as $T_{Mi}(0)$, while the true value deviates by $T_{Mi}(0)+\Delta_{Mi}$, due to the influence of measurement error. As a result, deviation by $\Delta_i(t_i)$ from the reference line occurred at time t_i."

Factor (b) is caused by an error in refractory temperature (accumulated heat of ladle refractory) at the time of converter furnace tapping. This is a view stating, "The initial value of the ladle refractory temperature in the i^{th} past charge was recognized to be $T_{Ri}(0)$. However, in reality, there was an error, Δ_{Ri}, and, as a result, a deviation by $\Delta_i(t_i)$ from the reference line occurred at time t_i."

Factor (c) is due to an error in heat transfer from molten steel to ladle refractory during the ladle transport. This is a view stating, "For the heat transfer coefficient h_i in the i^{th} past charge, there actually was an error Δ_{Hi}, which caused the deviation from the reference line by $\Delta_i(t_i)$ at time t_i."

4.2 Time variation of error due to each variation factor

In order to grasp the influence of the error caused by each variation factor, (a), (b), and (c), mentioned in the previous section, a simulation was performed with a highly accurate calculation model[5] based on a theory. As shown in **Fig. 4**, if caused by the initial molten steel temperature variation ((a)), the value of $\Delta_i(t_i)$ is almost constant irrespective of time. On the other hand, if caused by the initial refractory temperature variation ((b)), the value of $\Delta_i(t_i)$ increases with time. Moreover, if caused by the heat transfer coefficient variation ((c)), $\Delta_i(t_i)$) increases with time and then converges to 0.

As described above, although $\Delta_i(t_i)$ can be mapped for an arbitrary time by simulation, there are two problems.

One problem is the calculation cost. Although the ICT has advanced remarkably, it is difficult to execute high accuracy calculation on tens of thousands or more of past data in real time. Without a measured value for the refractory temperature, how to calculate is also an issue.

Another problem is that it is unknown which variation factor is predominant. The mapping direction depends on the variation factor, and it is not known what causes the actual error. Consequently, it cannot be determined which direction to map.

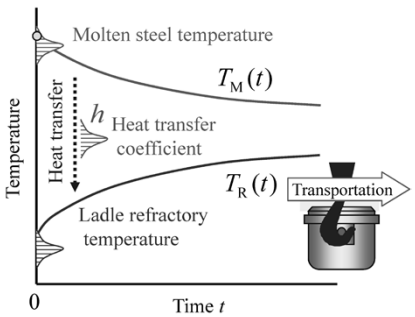

Fig. 3 Factors of temperature variability in ladle transportation

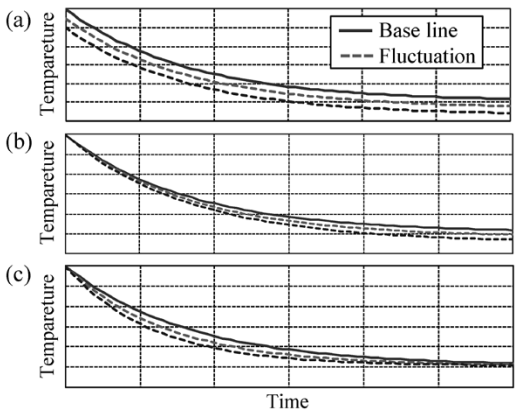

Fig. 4 Variation with time of temperature in each variability factor

4.3 Formulation based on simplified physical model

The dominant equation of two-body heat transfer is used for the calculation of a state without variation. The dominant equations of molten steel temperature $T_M(t)$, heat transfer $Q(t)$, refractory temperature $T_R(t)$ are as follows, respectively:

$$\rho_M c_M v_M \frac{dT_M(t)}{dt} = -Q(t) \quad \cdots\cdots (4)$$

$$Q(t) = A \cdot h \cdot (T_M(t) - T_R(t)) \quad \cdots\cdots (5)$$

$$\rho_R c_R v_R \frac{dT_R(t)}{dt} = Q(t) \quad \cdots\cdots (6)$$

wherein ρ_M, c_M, and v_M are the density, specific heat, and volume, respectively, of molten steel,

ρ_R, c_R, and v_R are the density, specific heat and volume, respectively, of ladle refractory,

A: contact area between molten steel and refractory, and

h : heat transfer coefficient.

Further, the replacements,

$$\alpha = \rho_R c_R v_R / (\rho_R c_R v_R + \rho_M c_M v_M),$$
$$\beta = (\rho_R c_R v_R + \rho_M c_M v_M) / (\rho_R c_R v_R \cdot \rho_M c_M v_M)$$

result in the well-known basic equation,

$$T_M(t) = -\alpha \cdot (T_M(0) - T_R(0)) \cdot (1 - e^{-\beta h t}) + T_M(0) \quad \cdots\cdots (7)$$

Equation (7) is an expression without a variation factor and corresponds to the temperature reference line. The equations expressing the changes in molten steel temperature due to initial molten steel temperature variation, Δ_M , initial refractory temperature variation, Δ_R, and heat transfer coefficient variation, Δ_H, are as follows, respectively.

$$T_M(t,\Delta_M) = -\alpha \cdot (T_M(0) + \Delta_M - T_R(0)) \cdot (1 - e^{-\beta h t}) + T_M(0) + \Delta_M \quad \cdots\cdots (8)$$

$$T_M(t,\Delta_R) = -\alpha \cdot (T_M(0) - T_R(0) - \Delta_R) \cdot (1 - e^{-\beta h t}) + T_M(0) \quad \cdots\cdots (9)$$

$$T_M(t,\Delta_H) = -\alpha \cdot (T_M(0) - T_R(0)) \cdot (1 - e^{-\beta (h + \Delta_H) t}) + T_M(0) \quad \cdots\cdots (10)$$

4.3.1 Influence of variation in initial molten steel temperature

By taking the difference between the reference lines expressed by Equation (7) and Equation (8), the time variation $\Delta(t, \Delta_M)$ of the variation of the initial molten steel temperature is formulated.

$$\Delta(t,\Delta_M) = T_M(t,\Delta_M) - T_M(t) = \Delta_M \cdot \{-\alpha(1 - e^{-\beta h t}) + 1\} \quad \cdots\cdots (11)$$

From Equation (7),

$$\alpha \cdot (1 - e^{-\beta h t}) = (T_M(0) - T_M(t)) / (T_M(0) - T_R(0)) \quad \cdots\cdots (12)$$

So, substituting Equation (12) for Equation (11) and rearranging lead to:

$$\Delta(t,\Delta_M) = \Delta_M \cdot (T_M(t) - T_R(0)) / (T_M(0) - T_R(0)) \quad \cdots\cdots (13)$$

Since the initial temperature of the refractory is much lower than the molten steel temperature, it can be approximated as follows:

$$(T_M(t) - T_R(0)) / (T_M(0) - T_R(0)) \approx 1$$

Therefore, the influence of initial molten steel temperature variation can be approximated as constant.

$$\Delta(t,\Delta_M) \approx \Delta_M = const. \quad \cdots\cdots (14)$$

4.3.2 Influence of initial refractory temperature variation

Similarly, taking the difference between Equation (7) and Equation (9) and rearranging it by substituting Equation (12), the time change $\Delta(t, \Delta_R)$ of the variation in the initial refractory temperature is given by Equation (15).

$$\Delta(t,\Delta_R) = T_M(t,\Delta_R) - T_M(t) = \Delta_R \cdot (T_M(0) - T_M(t)) / (T_M(0) - T_R(0)) \quad \cdots (15)$$

The ratio of the variation $\Delta(t_i, \Delta_R)$ with respect to the reference line at the temperature measurement time t_i in the i^{th} past charge to the variation $\Delta(t, \Delta_R)$ at a given time t is;

$$\Delta(t,\Delta_R) / \Delta(t_i,\Delta_R) = (T_M(0) - T_M(t)) / (T_M(0) - T_M(t_i)) \quad \cdots (16)$$

Therefore,

$$\Delta(t,\Delta_R) = \Delta(t_i,\Delta_R) \cdot (T_M(0) - T_M(t)) / (T_M(0) - T_M(t_i)) \quad \cdots (17)$$

Consequently, the influence of the variation of initial refractory temperature on the variation of molten steel temperature becomes analogous in the temperature axis direction.

4.3.3 Influence of variation in heat transfer coefficient

Equation (10) is same as Equation (7) whose t is replaced with $((h+\Delta_H)/h \cdot t$. In other words, assuming that τ_i is the time when the measured temperature value $T_M(t,\Delta_H)$ at time t_i and the temperature reference line $T_M(t)$ of Equation (7) have the same value, then $((h+\Delta_H)/h) \cdot t_i = \tau_i$, and consequently $(h+\Delta_H)/h = \tau_i / t_i$. Therefore, the variation of temperature with respect to the reference line at a given time t is given by:

$$\Delta(t,\Delta_H) = T_M(t,\Delta_H) - T_M(t) = T_M((\tau_i / t_i) \cdot t) - T_M(t) \quad \cdots (18)$$

As can be seen from Equation (18), the influence of the heat transfer coefficient variation on the molten steel temperature becomes analogous to the time axis direction.

As described above, the mapping can be done at any time with a relatively simple calculation formula for any of the variation factors, if $f_i(t)$ calculated with the temperature reference line physical model[5] of the past charge and measured temperature values are given.

4.4 View on variation factor ratio

When actual data is mapped at the transport time t_0, the distribution shape of temperature varies depending on the ratio of the variation factor, that is, the mapping method using the ratio of Equation (14), or (17), or (18) (**Fig. 5**). From the relationship between the transport time and the degree of temperature drop, the transport time and the variation factors are considered to have no relationship. Therefore, in the past recorded data, the mapping at the time t_0 of the data group with short transport time and the mapping at time t_0 of data group with long transport time are considered to have consistent distribution shapes if the mapping method is appropriate. Hence, among the factor ratios η_M, η_R and η_H when

$$\Delta_i(t_0)=\eta_M\cdot\Delta_i(t_0,\Delta_M)+\eta_R\cdot\Delta_i(t_0,\Delta_R)+\eta_H\cdot\Delta_i(t_0,\Delta_H) \quad \cdots \quad (19)$$

in Equation (3), the value of η_M was varied in the range of 0.0 to 1.0 to obtain the optimum point where the distribution shape after mapping of the two data groups most closely matched. In the range of actual operation time, the distribution shapes were similar, and hence $\eta_R=\eta_H=(1-\eta_M)/2$.

The evaluation of different data groups showed that η_M became optimum within the range of 0.30 to 0.36 and hence $\eta_M=\eta_R=\eta_H=1/3$.

4.5 Weighting based on similarity

Data items of the i^{th} past charge and the on-going charge are assumed to be

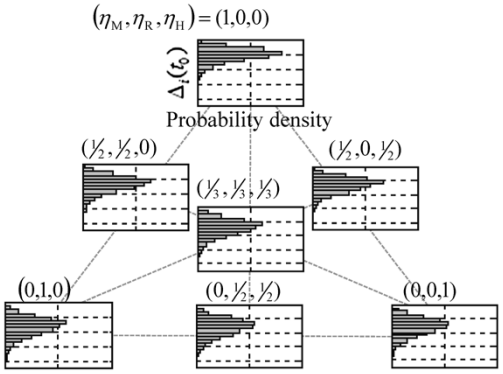

Fig. 5 Difference in temperature distributions after mapping by ratio of variability factors

$X_i=[x_{i1}\ x_{i2}\ \cdots\ x_{iL}]$ and $X_0=[x_{01}\ x_{o2}\ \cdots\ x_{0L}]$, respectively, to determine the weighted Euclidean distance d_i for evaluating their proximity.

$$d_i=\sqrt{\sum_{j=1}^{L}q_j(x_{ij}-x_{oj})^2} \quad \cdots\cdots\cdots\cdots\cdots\cdots\cdots\cdots \quad (20)$$

wherein $q_i>0$: weighting factor.

The similarity, $w_i=\exp(-\lambda d_i)$, calculated from the distance d_i is taken as a weight and corresponded to the temperature $T_{0i}(t_0)$ of Equation (3) to construct a weighted histogram (λ is the adjustment parameter), of which area is normalized to be 1 as a probability distribution to be presented to the operators.

5. Results of actual application

This technique was put into practical use in June 2011 in the steel-making process of the Kakogawa Works. **Fig. 6** shows the calculation results for molten steel temperature distribution and the temperature measured in a tundish. Here, the examples were chosen where the temperature distribution shape and its time change were characteristic. As shown in (a)-(d), it is confirmed that differences in temperature variation corresponding to each operating condition can be appropriately predicted.

Moreover, by evaluating the difference between the target value of molten steel temperature and the actual temperature in the tundish, the present system has been confirmed to reduce the deviation from the target value to less than half (about 41%) of the conventional value.

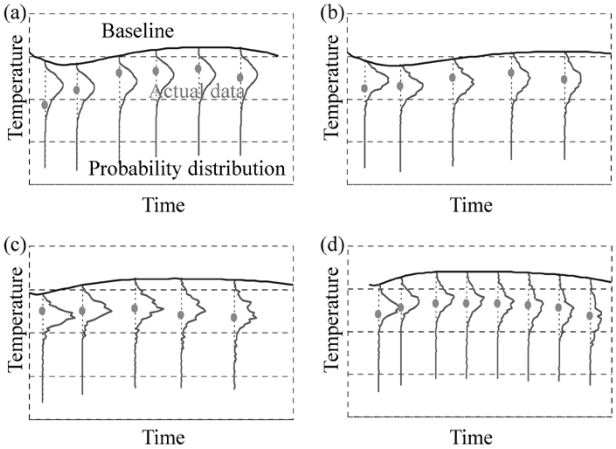

Fig. 6 Comparison between shapes of predicted distribution of molten steel temperature and measurement data in tundish

Conclusions

A method capable of uniformly predicting the multi-step probability distribution was developed by mapping the variation from the temperature reference line based on the physical model considering the thermal influence factor and constructing a weighted histogram in accordance with the similarity between the two.

By weighting in accordance with the similarity with the on-going charge during actual operation against the massive amount of past data accumulated by utilizing ICT, and by converting this to virtual experience information to be presented to the operators, it has become possible to supplement their experience and support them in making appropriate decisions and taking actions.

References

1) H. Shigemori. *JFE TECHNICAL REPORT*. 2015, No.35, pp.8-13.
2) Y. Kadoya et al. *Transactions of the Society of Instrument and Control Engineer*. 2014, Vol.50, No.7, pp.528-535.
3) Kobe Steel, Ltd. *Output value prediction method, the apparatus and method of the program*. JP5363238, 2013-9-13.
4) N. Tomochika et al. *Current Advances in Materials and Processes* 2017, Vol.30, No.2, p.782.
5) T. Nakaoka et al. *Current Advances in Materials and Processes* 2009, Vol.22, No.1, p.83.
6) T. Okura et al. *Current Advances in Materials and Processes* 2011, Vol.24, No.1, p.29.
7) S. Sonoda et al. *Current Advances in Materials and Processes 2011*, Vol.24, No.1, p.33.

Development of Macro Simulation Model to Support Multi-product, Mixed Flow Production of Aluminum Rolling

Toyohiro UMEDA*1, Akihisa HORIO*2, Satoru YOSHINO*2, Katsumasa UEDA*2

*1 Production Systems Research Laboratory, Technical Development Group
*2 Manufacturing Department, Moka Plant, Aluminum & Copper Business

The manufacturing processes for the sheets, plates, and strips of steel, aluminum, and copper that are Kobe Steel's main material products are characterized by the mixed production of a great variety of products. Hence, for the sake of productivity and quality, a plurality of workpieces processed by an identical type of method are aggregated together as one lot on the basis of the operating conditions specific to each apparatus. A simulation model has been developed to support production planning and to help in considering operational rules as well as the capital investment policy involved in such processes. The model has a hierarchical queue structure to flexibly express various lot-making operations. The model further incorporates a mechanism for estimating the time it takes before the minimum number of workpieces required to organize a lot become available in order to reduce the unwanted stagnation of jobs in the process. The effectiveness of the proposed model has been demonstrated by numerical experiments, while its accuracy and applicability in the macro evaluation of material flow have been verified using actual plant data on aluminum rolling.

Introduction

Recently, in material processing plants that manufacture, among others, ferrous and non-ferrous rolled products, an increasing variety of products are being produced in variable quantities, inevitably making the production flow more and more complicated. Furthermore, strong requirements for reducing lead-time and work-in-process (WIP) are making it difficult to properly control the production flow through an entire plant by the mere experience and intuition of experts. Hence, there is a strong desire for a system that supports determinations and decisions for advanced production management on the basis of objective data and evaluation by theoretical modelling.

Approaches to systematization include a scheduling system that calculates the detailed work sequence of apparatuses to support daily to weekly planning. Also included is a simulation for computing the macroscopic production flow in a plant to devise the operational guidelines for the resources in the plant for production planning on a monthly to yearly basis. These all play important roles in modelling production processes,[1)-3)] and some are reported to have been applied to job-shop type processes, in which the process steps vary depending on the products.[4)-6)]

Meanwhile, for a simulation that is usable in real operational investigations of the production steps in material processing, which requires the reduction of setup time and cost as well as stable quality in its complexity, a modelling of "lot aggregation and sequencing" is essential so that similar types of jobs (various processes involved in manufacturing final products from raw materials) are performed continuously under process-specific conditions.

For the problems of lot aggregation and sequencing in situations involving changeover time between lots, several approaches based on optimum solution searching have been reported.[7)-11)] However, the scale of the material manufacturing process (several tens of steps) and the number of workpieces (several thousand/month) covered by this paper require enormous calculation time, making it difficult to adapt these approaches in daily practice.

Hence, this paper proposes a simulation model for executing lot aggregation efficiently with practical accuracy for the material manufacturing process in multi-product, mixed-flow job shops involving lot aggregation at each step. The present model is based on a queue structure, which has a two-layer hierarchy with a first layer for aggregating lots and a second layer for rearranging the aggregated lots under predetermined conditions. In addition, this model is combined with a function of forecasting the arrival of workpieces to each apparatus with the renewal of the simulation time, thus, to forecast the time when each lot of a preset size is completed, so as to suppress the unwanted stagnation time of jobs associated with lot organization. As a result, it has become possible to convert the huge amount of production data into information on realistic production flows of the entire process. This has enabled forecasting the production and logistics situations on a monthly to yearly basis in the large-scale material manufacturing process.

This paper outlines these characteristic functions and introduces the verification results confirming the validity of the proposed model, giving the test data and verification examples along with the actual data of an aluminum rolling plant.

1. Lot organization in material manufacturing process

In a material manufacturing plant that produces a wide variety of products, there are very many types of jobs involved, and the production is carried out via job-shop-type production lines, in which each line varies depending on the job specifications. At each step, an operation is generally performed with "aggregated lots," in which a plurality of workpieces with identical processing specifications are grouped and processed together in order to improve productivity and to reduce the cost by decreasing the time and number of changeovers. Examples of lot aggregation are given below:

- In a heat-treatment shop that uses batch furnaces, workpieces with an identical annealing temperature are processed together in one furnace to reduce fuel consumption and to improve productivity.
- In a rolling shop that produces sheets of ferrous and non-ferrous metals, workpieces requiring rolls with an identical surface roughness are processed as continuously as possible to reduce the changeover of the rolls.
- In a surface-treatment shop, workpieces that require an identical type of paint or identical chemicals are processed together as much as possible, since the changeover takes an extremely long time.

Normally, there is a certain degree of freedom in the number of workpieces constituting a lot. The lot size and setup time in between lots, determined within that degree of freedom, affect not only the productivity of each apparatus but also the productivity of the entire plant, as well as the WIP, lead time, and cost, etc. In the material manufacturing process of multi-product, mixed-flow type, in which the job sequences are complicated, it is difficult to forecast the intermediate WIP and the production lead time while considering the aforementioned lot aggregation. Hence, a simulation model that can flexibly express lot organization in accordance with apparatus characteristics is required for conducting various investigations.

2. Characteristics of simulation model

2.1 Queue structure for lot organization

The basic structure of the model is a queue type and is characterized by a hierarchical structure[12), 13)] to perform lot organization in an efficient, fine-tuned manner (**Fig. 1**). In other words, a queue corresponding to the conditions of lot aggregation

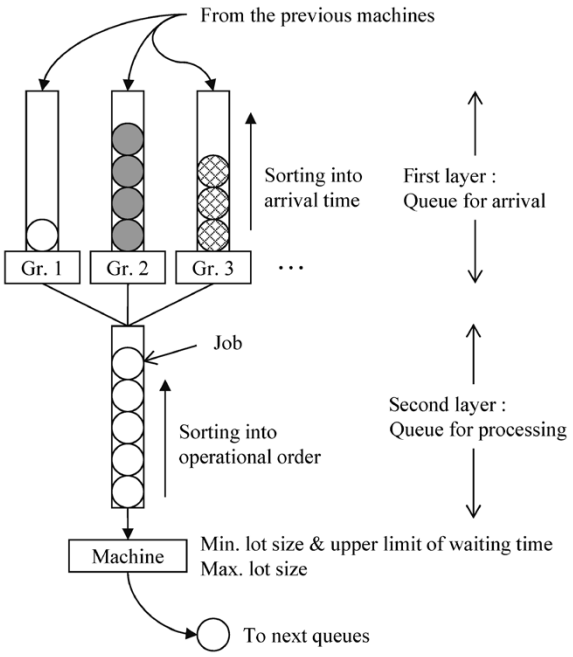

Fig. 1 Hierarchical queue structure for lot formation

for each apparatus is placed at the first layer and workpieces are stored there in the order of arrival. Since the types of lot aggregation conditions always change, this queueing model automatically generates queues in accordance with the specific attributes of each job. For each queue, calculation is conducted for the number of workpieces, aggregated in accordance with the progress of simulation, and for their waiting time so as to determine whether they are processable as a lot.

Meanwhile, each apparatus searches the arrival queues when it is ready to process the next lot, selects one queue where lots are available to be processed and extracts a predetermined number of lots from the top as the lots to be processed next. The extracted workpieces are sorted in processing order under the conditions set for each apparatus, stored in the processing reservation queue in the second layer in front of the apparatus, and are processed for the job one by one. In this way, the hierarchically structured queues enable efficient searching of the lots to be processed next and the rearranging of the workpieces.

2.2 Parameters used for lot organization

As the parameters of the simulation, which is equivalent to the lot organization guideline, the following values can be set for each apparatus:

- Minimum number of workpieces: The minimum unit that can be processed as one lot. It is often set as an operational guideline for the sake of production efficiency, cost, or workability.
- Maximum number of workpieces: The maximum

unit that can be processed as one lot. It is usually determined by the apparatus specifications and operational restrictions.

- Maximum lot-waiting time: Until the minimum number of workpieces are available, the workpieces that have arrived are in a waiting state. The maximum time this state can continue is the maximum lot-waiting time. To prevent long-term stagnation, any stagnation longer than this time period allows organization as a lot even if the lot consists of fewer than the minimum number of workpieces.
- Setup time: The time it takes for the changeover between lots. In determining the next lot to be processed, productivity can be increased by preferentially selecting one with a short setup time.

2.3 Function for forecasting lot completion time

In the case where there are only a few workpieces with identical lot aggregation conditions and it is difficult to fill the minimum number, it is easier for implementation in the system to keep the workpieces stagnated until the above maximum lot-waiting time expires and then to process them as an incomplete lot. In real operations, however, when it is anticipated that a lot will not become available after waiting the maximum length of time, the incomplete lot is processed without waiting until the expiration of the maximum time to suppress stagnation loss.

Hence, as shown in **Fig. 2**, the present model incorporates a mechanism for forecasting the earliest starting time of each lot from the estimated arrival time of the workpiece at the queue, thereby enabling the same determinations as those for actual operation.[13] The outline is as follows:

(1) Not only each workpiece that has arrived and is waiting for its next step is stored in the queue, but also all the unfinished workpieces to be processed later are stored in the queue as workpieces scheduled to arrive.

(2) For each scheduled-to-arrive workpiece in the queue, its estimated arrival time is calculated and set on the basis of the work completion time at the corresponding apparatus and the lead time between standard steps, as shown in Equation (1).

$$\overline{T}^{S}_{j,n}(t)=\max\{\overline{T}^{S}_{j,n-1}(t)+L_{j,n},\ e_{j,n}(t)\} \quad \cdots\cdots\cdots\cdots\cdots\cdots \quad (1)$$

Wherein

$\overline{T}^{S}_{j,n}(t)$: The estimated arrival time or arrival time at the n^{th} process step of the workpiece j at simulation time t.

$L_{j,n}$: Standard lead time between the $(n\text{-}1)^{th}$ and n^{th} steps of workpiece j. This lead time includes the standard processing time and waiting time.

$e_{j,n}(t)$: The time when the apparatus that is to process the n^{th} step of workpiece j completes its last task at the simulation time t.

(3) The completion time for the minimum lot size is estimated on the basis of the estimated arrival time of each workpiece. More specifically, the arrival time or the expected time for the workpiece to be in the arrival queue is sorted in order starting with the earliest, and the time at which the last workpiece constituting the minimum lot size arrives is set as the estimated completion time of the lot. This time is re-calculated sequentially with the renewal of the simulation time.

(4) If there is no workpiece that can arrive by the expected lot completion time and there are workpieces waiting longer than the maximum lot waiting time in the queue, they are regarded as processable as a lot even if the lot is smaller than the minimum lot size. In Fig. 2, Workpieces ① and ② have already arrived, and Workpieces ③, ④, and ⑤ are scheduled to arrive. At this simulation time, it is determined that 5 workpieces, the minimum lot unit, will not be available within the maximum waiting time of Workpiece ①. Workpiece ③, however, may arrive before the maximum waiting time of Workpiece ① expires; hence the simulation time can be advanced until the arrival of Workpiece ③ so as to have Workpieces ①, ②, and ③ organized and processed as an incomplete lot.

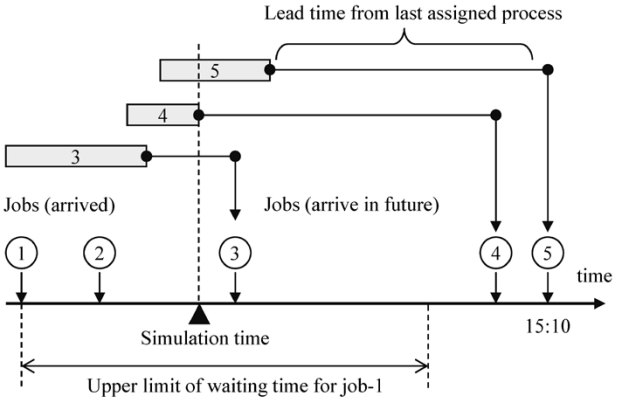

Min. lot size	5
Lot size within upper limit of waiting time	3
Estimated time of lot completion	9/10 15:10

Fig. 2 Forecast of lot completion time

3. Verification of proposed model

3.1 Effect of forecasting lot completion time

In order to confirm the validity of the forecast function of lot completion time, or the estimation of lot completion time (ELC), the estimated time before the minimum lot unit becomes available, a simple example of a job-shop process consisting of 5 steps, 10 items, and 1,000 jobs, in which each step has 3 to 5 lot types, was prepared to compare the differences in simulation results obtained with and without ELC.[14] The results are shown in **Fig. 3**. From this figure, the following characteristics and effects of this function are confirmed.

- For a given maximum lot waiting time, the lead time is shortened when ELC is turned on. This is probably because workpieces are processed without waiting until the completion of the maximum time if a minimum-sized lot does not become available.
- When the maximum lot waiting time is short, the lead time shortening effect is small. This is probably because the processing is often performed without waiting until the minimum lot size even when ELC is OFF, making any difference between them unlikely to occur.
- The number of setup times tends to increase when ELC is ON.
- When the maximum lot waiting time is extremely short or extremely long, the difference in the number of setup times is small. As described above, when the maximum lot waiting time is short, small lots are likely to be processed regardless of whether ELC is ON or OFF, making a difference between them unlikely to occur.

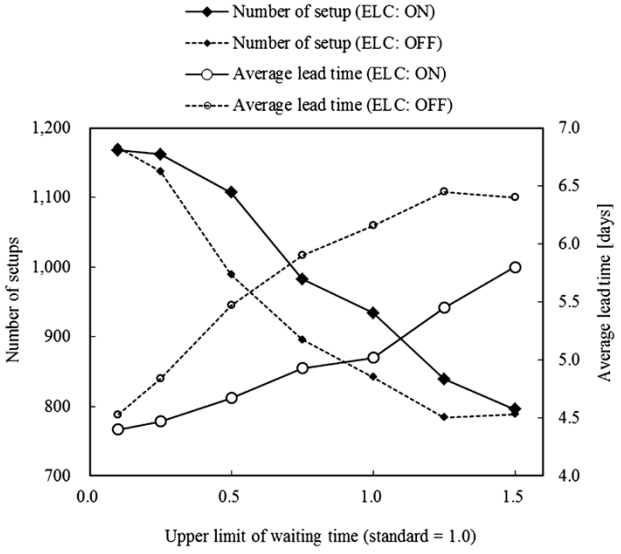

Fig. 3 Difference in number of setups and lead time based on predicted lot completion time

In addition, it is considered that, when the maximum lot waiting time is long, a lot that has not become available even after the waiting period can be processed early as having the same size.

Next, the above experimental results were compared on the two axes of the number of setups and the lead time. The results are shown in **Fig. 4**. It is confirmed that there is a trade-off relationship between the two regardless of whether ELC is ON or OFF, and when ELC is ON, it is shown that the trade-off is relaxed. This indicates that, when ELC is ON, the production can be accomplished with a smaller number of setups for a given lead time, or with a shorter lead time for a given number of setups.

3.2 Verification in realistic scale process

3.2.1 Target process

Next, the production process at Kobe Steel's aluminum rolling plant was set up in the present simulator to perform an experiment verifying the lot organization guideline, assuming actual utilization in the plant. **Fig. 5** outlines the aluminum rolling process. A slab produced in the melting & casting step is processed through several to dozens of steps including hot rolling, cold rolling, heat treatment (in batch/continuous furnaces), straightening, surface treatment, and cutting before being shipped as a plate or a coiled product. The simulation targeted the steps of hot rolling and thereafter, in which the number of apparatuses is assumed to be approximately 70 and the number of workpieces charged per day to be approximately 100. In addition, the conditions for lot organization were set for each main apparatus (**Table 1**). It should be noted that there were several lot attributes for apparatuses with a smaller number of attributes and several dozens for apparatuses with a greater

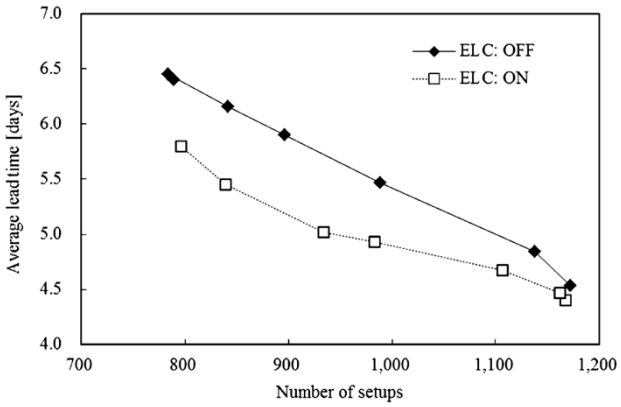

Fig. 4 Relationship between number of setups and lead time

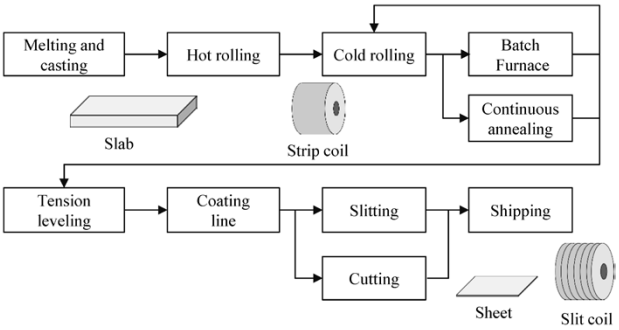

Fig. 5 Example of manufacturing process in aluminum rolling mill

Table 1 Example of lot organizing conditions

Facility	Collecting attributes	Lot size* (min., max.)	Max. lot wait [days]
Cold rolling	Roll surface type	(3, 100)	7
Batch furnace	Treatment temperature	(5, 15)	7
Continuous annealing	Treatment temperature	(5, 62)	7
Coating line	Paint type	(13, 44)	30

*Lot size is the ratio to when maximum lot size of cold rolling = 100

number of attributes (an indentical attribute allows organization into one lot).

3.2.2 Verification of lot organization guideline and productivity index

As a guideline of lot organization, a 3-month-long simulation was performed by changing the minimum lot size (minimum number of workpieces) exemplified in Table 1 to examine representative productivity indices.

First, the settings of minimum lot size were changed for the main apparatuses in the production process to examine the changes in the resulting lot sizes organized by the simulator. An example of the continuous annealing furnace is shown in **Fig. 6**, and an example of the surface treatment apparatus is shown in **Fig. 7**. In either example, increasing the set value for the minimum lot size increases the average size of the lot organized in the simulator, and the amount of the increase gradually decreases. This is probably because when the minimum lot size becomes larger, workpieces whose waiting time exceeds the maximum lot waiting time occur before the minimum lot size is reached, resulting in an increase in the number of lots smaller than the minimum lot size. It should be noted that the dotted line in the figure shows, for reference, the average lot size manually calculated from the actual data.

The minimum lot size was set to approximately 20% at maximum for the continuous annealing furnace and to approximately 70% for the surface treatment apparatus in the hope of simulating a lot size close to that of actual operations.

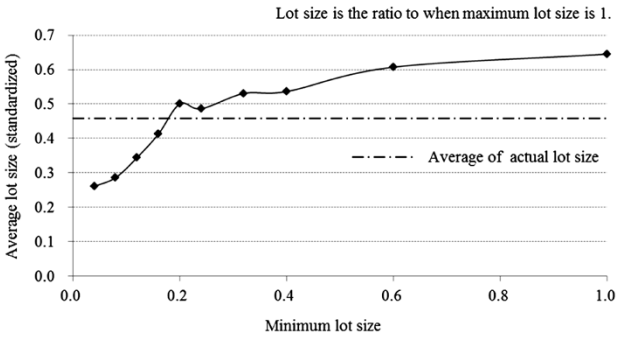

Fig. 6 Relationship between minimum lot size setting and average lot size of simulation results in continuous annealing line

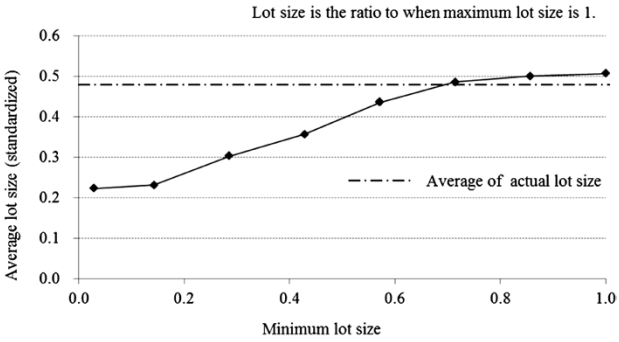

Fig. 7 Relationship between minimum lot size setting and average lot size of simulation results in surface coating line

Next, the main apparatuses with high loads were selected (about 1/3 of the whole), and the minimum lot size was changed with a constant ratio to the maximum lot size to study the total number of setups and the average lead time from the hot rolling to shipping. The results are shown in **Fig. 8** and **Fig. 9**, respectively. It is shown that, as the minimum lot size increases, the number of setups decreases, but the decrement becomes smaller. On the other hand, the lead time increases almost linearly, raising concern that making the minimum lot size too great may increase the disadvantage of increased lead time rather than the advantage of a decreased number of setups. The number of setups affects the production cost and work load, while the lead time affects WIP inventory and the ability to respond to the deadline. For this reason, it is important to utilize the guideline of the minimum lot size on the basis of the allowable level of setups and target lead time.

3.2.3 Accuracy verification based on macro logistics performance

A prerequisite for using the simulator to forecast the future logistics situation in order to utilize it for various operation investigations is to adjust the parameters of the simulator so that the logistics situation at a certain time can be reproduced with

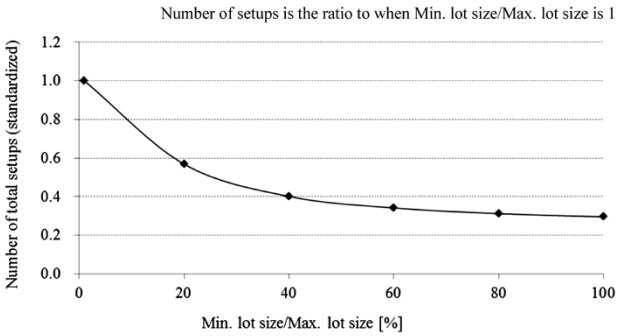

Fig. 8 Relationship between minimum lot size and number of total setups

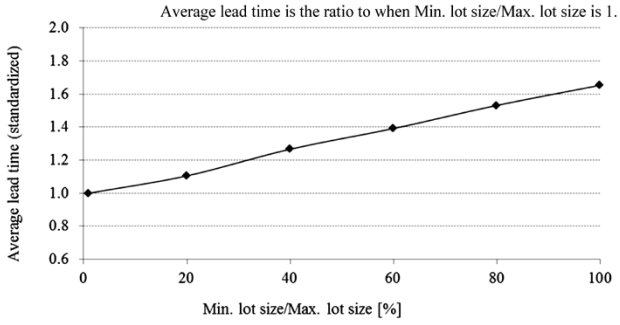

Fig. 9 Relationship between minimum lot size and average lead time

reference to a certain period in the past. This allows the setting of the base for future forecasts. Hence, a certain period in the past (half a year) was chosen, and the processing time, setup time, operation rate, item composition, yield, etc., were set as the actual base for the period in addition to the minimum lot size verified in the previous section. Thereupon, a comparison was made between simulation results and the actual values, in which the simulation was based on a virtually prepared charge plan. The results include the amount of intermediate WIP in the plant obtained in this way, as well as the amount of daily transportation among storage locations.

In the evaluation of a logistics system, maximum values count as well as average values. **Table 2** shows the results of comparing the average value and the maximum value of the amount of intermediate WIP for a typical storage location and the amount of transportation taking place between them. As shown in this table, the average values and the maximum values of the simulation results differ by 5% or less from the actual results. Given that the actual maximum values are 125% to 150% of the average, these results are well within the practically acceptable range for evaluating macro logistics. In particular, the maximum values agree well, which is the key point in considering the enhancement of the storage location and the transportation capacity, confirming that the present simulator can be an effective tool for the future verification of logistics

Table 2 Comparison of amount of work in process and transportation amount between actual values and simulation results

		Work in process		Transportation amount	
		Total	Cold rolling	ShopA →ShopB	ShopC →ShopD
Max.	Actual	125	125	155	150
	Sim.	117	122	148	143
Ave.	Actual	100	100	100	100
	Sim.	96	102	99	102

Each value is the ratio to when actual average is 100.

resources.

4. Example of simulator application

The simulation model proposed this time is intended to be applied in studying the operational policy in a plant where lots are organized uniquely at each step in the production and to investigating investment in apparatus and logistics resources. The following describes application examples.

4.1 Formulation of guideline for lot organization in accordance with load

From the results described in Section 3, it was found that the minimum lot size set for each apparatus strongly affects the changeover setups (which relates to the production cost) and lead time (which relates to the ability to respond to deadlines). Hence, the simulation model is expected to be utilized as a source of guidelines for minimum lot size, obtained from the number and time period of setups acceptable for a plant and the target lead time to achieve the production plan. For example, when the order-receiving schedule changes significantly, the guideline of lot organization may also change greatly as the productivity required for each apparatus changes. To cope with this, the present simulator imposes a restriction on the setup time of the bottle neck apparatus acceptable for each apparatus to achieve the productivity required for, e.g., the order-receiving schedule, and provide the guideline for minimum lot size to realize said setup time. Moreover, the simulation results allow the estimation of lead time for such a case. These provide the basis for providing a planning guideline for each apparatus in a coordinated manner and for calculating the production period for each item.

4.2 Consideration of necessary WIP amount and storage capacity at each location

In general, it is necessary to increase the amount of WIP held in front of an apparatus in

order to increase the lot size for the apparatus of the intermediate process and perform the operation with less setup time.[15] The present simulator analyzes the relationship between the minimum lot size and the setup time or the WIP amount, as shown in Fig. 8 and Fig. 9, so as to grasp the amount of WIP to be kept for the setup time allowable for production management. For this reason, this simulation model can be utilized in supporting decision making in formulating WIP holding plans when preparing monthly or periodic production plans and in the study of the minimum lot size guideline considering the capacity of storage locations. Especially in the case where products, ferrous and non-ferrous, are large in size and manufactured in large quantities, it is difficult to secure storage locations within a plant, and planning based on such a viewpoint becomes important.

4.3 Consideration of charge cycle for each item

In a material processing plant, there is also a process characteristic in the fact that, further back in the upper-stream steps, the differences in the degree of freedom for apparatus selection and in production conditions become smaller within an identical item (“Item,” as used here, generally refers to an order for identical applications and characteristics of products”). Hence, how to set the charging intervals for each item at the plant is also an important decision item in production management. **Fig.10** shows an example of the simulation results for the WIP transition at a certain storage location when the rolling interval for an item is changed in the hot rolling process. Here, two different comparisons are made for the case where the hot rolling interval of an item is N days, and one where the interval for the same has been doubled to 2N days.

As shown in Fig.10, the longer the charge intervals of an item in the hot rolling, the greater the WIP fluctuation becomes, with a higher peak value. It should be noted that, although not shown in these figures, the longer the charge interval, the fewer the setups. This is because a longer charge interval allows an item to be charged in a greater volume during a given period of time, increasing the tendency of large lots to be supplied to specific apparatuses and storage locations.

A typical situation is considered where the capacity of a storage location is not large enough, as with the case in the previous section. It is assumed that the capacity of a storage location is 650 items and the charge interval is N days. In this case, the WIP can be temporarily stored in a different location

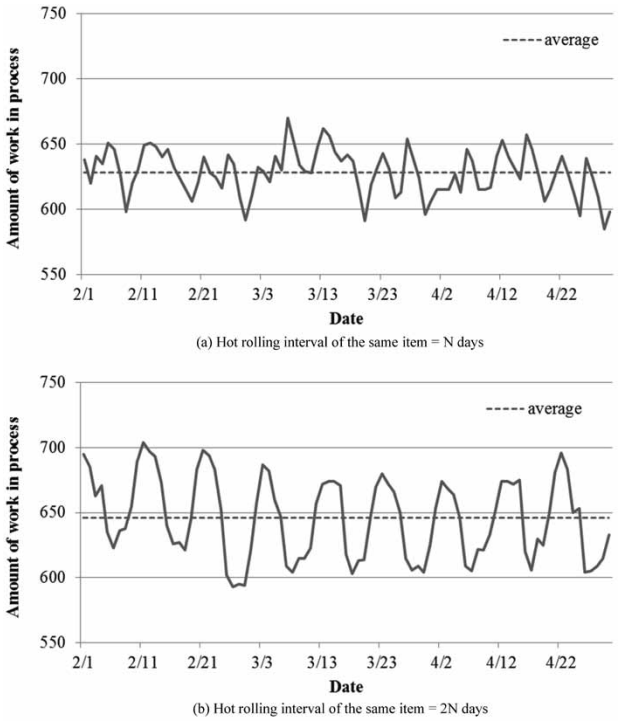

Fig.10 Hot rolling interval and work in process

(e.g., in a rented warehouse outside the plant) only for a few days in a period of three months until it is refreshed. If the charge interval is doubled to 2N days, it must be refreshed within about half that time period. In addition, a larger amount results in a substantial cost increase. In such a case, it is necessary to compare the cost increase due to the increase in the setup and the cost increase due to the WIP movement to the external warehouse to determine the charge interval. Although it is necessary to calculate the specific cost separately, the application of the simulation results of logistics to the decision making in production management enables an advanced decision which would be difficult to reach with experience and intuition alone.

4.4 Capacity evaluation of transportation resources

In the production steps of material processing, multiple apparatuses often share one storage location. Hence, the present simulator allows the arbitrary setting of the correspondence between the apparatuses and the storage locations. This has made it possible to evaluate not only the amount of WIP for each storage location but also the number of WIP items moving among storage locations in chronological order. Transportation means, such as track, forklift, crane, or dolly, are determined by mutual relationships among the storage locations, and it is possible to estimate the capacity required for these means of transportation. Hence, the present simulator can be applied to decision

making concerning investment to correct inadequate transportation capacity and to negotiations with the parties that outsource transport services.

5. Challenges for platformization

Kobe Steel intends to continuously utilize the developed simulator as a simulation platform for the making of various decisions in actual plants. However, practical applications are difficult only with the simulation model introduced this time, and further enhancement of functions as described below is considered to be necessary.

- For utilization in online decision making based on the present time, it is necessary to adjust the initial state of the simulator to the present state of the plant. To that end, it is necessary to establish an environment where the actual data of the plant (WIP status, start/completion time for each apparatus) and finalized process plan can be acquired in real time.
- The apparatuses and operations in the plant are continuously improved, and it is essential to periodically adjust the capabilities and setup conditions of the apparatuses. Since there are a vast number of apparatuses and setup conditions, a mechanism is necessary for automatically calculating these conditions from the accumulated actual data and registering them in a master.
- When the production plan changes drastically, the conditions based on past achievement may fail to produce the planned amount in a predetermined period. Under such circumstances, it is necessary to change the production procedure within a technically allowable extent to distribute the apparatus load. This area requires an expert's decision, and there is a need for an interactive mechanism.
- It is also an important role of simulation to derive conditions for obtaining intended results. Such cases reveal the importance of a visualization tool for determining which conditions should be modified by searching for simulation results, as well as a tool for analyzing the result data.

Conclusions

This paper has described a simulation model that can quantitatively evaluate the influence of the lot organization conditions on the flow of production on the basis of the product and process data while focusing on the operation with lot organization, which is the operational guideline for material manufacturing processes of a multi-product, mixed-flow type. In constructing the model, a method of generating a queue for each lot group at each step was adopted to efficiently and precisely reproduce the process-specific lot operation at each step. In addition, it was made possible to adjust the stagnation time for lot aggregation at each apparatus by providing the maximum time that a workpiece can wait in the queue until a lot with a predetermined size becomes available. Furthermore, a mechanism was incorporated to suppress unwanted stagnation time, which occurs when the lot does not become available within the maximum waiting time, by forecasting the time when the workpieces, including the ones in not-yet-started steps, will arrive at the queue.

A case study has verified that the maximum waiting time until a lot with a predetermined size becomes available and the minimum lot size can be parameters for adjusting the trade-off between the number of changeover setups and the production lead time. Also, a function to forecast the arrival time at each queue was introduced, and thereby the trade-off between the number of setups and the production lead time was confirmed to have been relaxed, as compared with a case where this function was not used. In addition, a comparison of the execution results based on a product and its process data at an aluminum rolling plant and actual logistics data has confirmed the accuracy feasible in the practical use in macro logistics verifications.

The future plan is to acquire knowledge concerning the parameter setting related to lot formation, which provides guidelines that have not necessarily been clarified in actual process management, although it is necessary to adjust the minimum lot size and maximum lot waiting time, etc., in accordance with the production environment with the aim of enabling more accurate calculation of the production flow in the actual factory. A challenge for the more distant future is to develop a technology to automatically adjust many parameters related to the lot organization and setup conditions in accordance with the changes in operation so that the present system is continuously utilized in supporting daily planning and operation review.

References

1) K. Nakano. *Transactions of the Institute of Systems, Control and Information Engineers*. 1997, Vol.41, No.3, pp.106-111.
2) N. Ueno. *Operations Research*. 1993, Vol.38, No.11, pp.571-577.
3) H. Inoue et. al. *Journal of the Society of Instrument and Control Engineers*. 1994, Vol.33, No.7, pp.547-553.
4) M. Arakawa et. al. *Journal of Japan Industrial Management Association*. 2001, Vol.51, No.6, p.603-612.

5) M. Arakawa et. al. *Transactions of the Institute of Systems, Control and Information Engineers*. 2003, Vol.16, No.9, pp.451-460.
6) T. Imoto et. al. *Transactions of the Society of Instrument and Control Engineer*. 2013, Vol.49, No.11, pp.1057-1063.
7) K. Morikawa et. al. *Transactions of the Japan Society of Mechanical Engineers (C)*. 1995, Vol.61, No.589, pp.354-360.
8) T. Fukayama et. al. *The transactions of the Institute of Electrical Engineers of Japan. C*. 2006, Vol.126, No.6, pp.771-779.
9) H. Meyr. *European Journal of Operational Research*. 2002, Vol.139, No.2, pp.277-292.
10) T. Kaihara et. al. *Proceedings of Manufacturing Systems Division Conference 2012, The Japan Society of Mechanical Engineers.* 2012, Vol.61, No.62, pp.61-62.
11) A. Kuriyama et. al. *Journal of Japan Society for Production Management*. 2009, Vol.15, No.2, pp.23-38.
12) T. Umeda et. al. *R&D Kobe Steel Engineering Reports*. 2006, Vol.56, No.1, pp.2-7.
13) A. Horio et. al. *Proceedings of the 61st Annual Conference of the Institute of Systems, Control and Information Engineers*. 2017, Vol.131-4.
14) T. Umeda et. al. *Proceedings of Scheduling Symposium 2014. 2014*, pp.155-160.
15) A. Horio et. al. *Proceedings of the 59th Annual Conference of the Institute of Systems, Control and Information Engineers*. 2015, Vol.141-3.

Applications of ICT to Robot Welding System

Takeshi KOIKE*1, Yoshihide INOUE*2, Atsushi FUKUNAGA*1
*1 Welding System Department, Technical Center, Welding Business
*2 Technical Center, Welding Business

In recent years there has been a rise in expectations for the improvement of the productivity of robot welding systems using information and communication technology (ICT). To meet these customer needs, Kobe Steel has developed a 3D-CAD link system that retrieves the data of workpieces from the design department and automatically detects welding lines to create a robot program. This has eliminated the need for customers to teach robots and has greatly improved their productivity. The company also provides a production monitoring software, called AP-SUPPORT™. This software has the capability of automatically collecting production data for the welding robot system and outputting reports on production results, thus contributing to the improvement of productivity at customers' sites.

Introduction

With the advancement of information and communication technology (ICT), the Industrie 4.0 and Internet of Things (IoT), advocated by Germany and the U.S., respectively, are changing production fields drastically. ICT has begun to be widely used for the machines and equipment used in welding processes, which require productivity improvement.

Especially in recent years, there has been a strong demand to improve the productivity of high-mix, low-volume products with complicated shapes, in which higher production efficiency is required as a whole system by closely combining the design section with production sites.

This paper explains the functions of the welding robot system based on the ICT of Kobe Steel and the approach of improving productivity using them.

1. Significance and challenges of welding systems in product lifecycle management (PLM)

Product lifecycle management (hereinafter referred to as "PLM") is the process of uniformly managing product-related information throughout the product lifecycle, including product design, production, maintenance, disposal, and recycling, on the basis of ICT for the purpose of maximizing revenue. A system has been proposed for PLM, in which 3-dimensional CAD (hereinafter referred to as "3D-CAD") is introduced as a designing tool to convert product data into digital data such that the data is uniformly managed from the birth to the disposal of each product (**Fig. 1**).

Productivity improvement using 3D-CAD data is also covered by i-Construction, i-Bridge, and i-Shipping promoted by the Ministry of Land, Infrastructure, Transport and Tourism, Japan[1] and is believed to play an important role in the vertical integration of PLM. In the field of architecture, building information modeling (BIM) has been proposed to realize workflows including procurement, design, and production.

For the vertical integration of production by PLM, an automatic linkage between design information and production command is indispensable. It is also essential to collect information from the machines at the production work site and to feed it back to production scheduling, higher-level designing, procurement, and planning.

However, for the production of steel frames for ships, construction machinery, high-rise buildings, etc., which involves the welding of thick steel plates, it is not easy to generate the operating commands for welding robots from 3D-CAD data. The welding of thick steel plates involves determining the welding layer pattern, welding conditions, and torch electrode manipulation, which requires the know-how of welding itself, robot operation, the positioning of welding targets, etc.[2] Moreover, in addition to the welding current, voltage, and operation status of the welding robot system, the operation records must include the amount of spatter and/or fume and the conditions at the time of abnormal stopping of the robot.

A Kobe Steel welding robot system solving the problem of vertical integration of production includes a CAD link system for generating robot

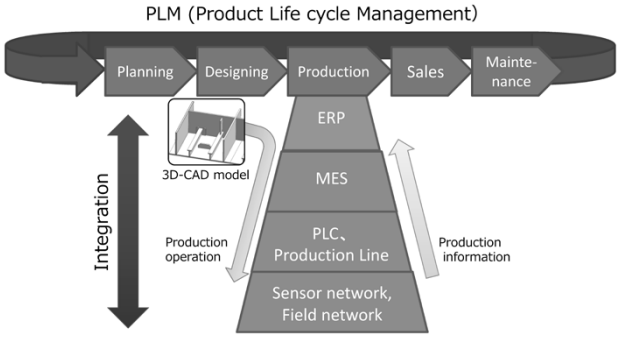

Fig. 1 Vertical integration of production and PLM mainly based on 3D-CAD

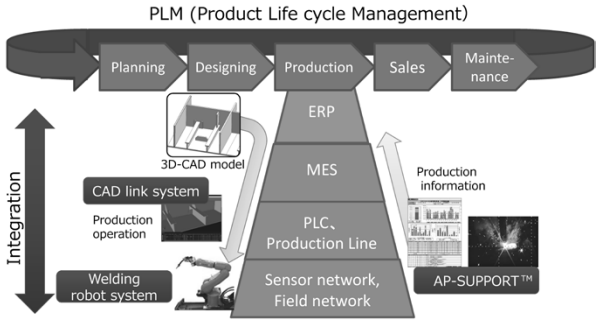

Fig. 2 Significance of welding robot system in PLM

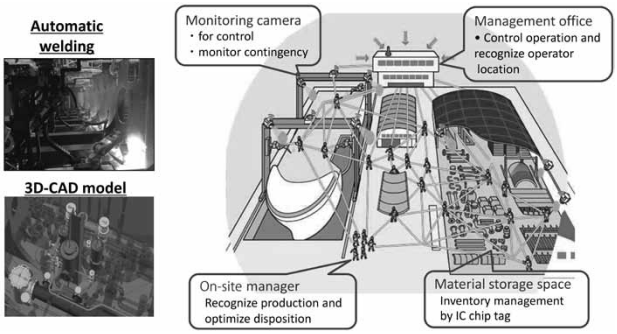

Fig. 3 Productivity improvement of shipbuilding using ICT[4)]

operation commands from 3D-CAD data, and the AP-SUPPORT™ Note 1) that records and reports the operational status of each robot (**Fig. 2**). It also comprises a camera function that can record video pictures in conjunction with the AP-SUPPORT™.

2. 3D-CAD link system

In Japan, the aged population is increasing rapidly, and there has been a remarkable decline in the work force. Against that backdrop, for the sake of its own survival, the shipbuilding industry, which requires a strategic shift to high-mix, low-volume production,[3)] is also promoting automation and labor saving in its production processes. In 2016 the Ministry of Land, Infrastructure, Transport, and Tourism launched a project called "i-Shipping" to improve marine productivity (**Fig. 3**[4)]).[5)] This project promotes the 3D-CAD and automatic welding machines for use in improving shipbuilding productivity. Hence, Kobe Steel has developed a CAD link system for the assembly process of shipbuilding.

2.1 Outline of CAD link system for shipbuilding

The CAD link system provided by Kobe Steel for shipbuilding retrieves 3-D model files prepared by the designing department and performs the coordinate matching of the data. The coordinates system of CAD can be different from that of a robot actually performing welding, depending on the part of the ship. Therefore, in order to detect welding coordinates correctly, it is necessary to match both coordinate systems and this conversion is carried out in the system. Next, welding information is automatically extracted, and the information is edited as necessary to prepare teaching programs. Finally, each program is sent to the corresponding robot to complete the preparation for welding (**Fig. 4**).

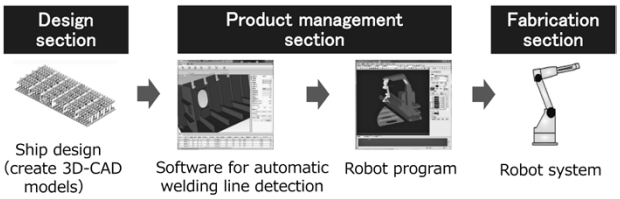

Fig. 4 Automatic generation of robot program from 3D-CAD model

2.2 Generating robot programs from design data, and welding

The present system automatically identifies each member on the basis of the coordinates and dimensions of the corresponding shape data of the three-dimensional model and detects only the joints to be welded in the assembly process (**Fig. 5**). It also automatically ignores joints where the robot and workpiece interfere and any joints located outside the motion range of the robot. The CAD link system contains the information on welded portions and welding conditions. Therefore, the customers simply prepare geometric information as CAD data, and no additional information is required for the welding. The robot operating commands (robot program) and welding conditions necessary for executing welding are automatically prepared on the basis of the combination of the members for the corresponding joint and the thicknesses of the lower plate and the vertical plate. Recommended data are provided in advance so as to maximize the performance of the welding robot and welding wires, eliminating the need for instructions concerning welding conditions including instructions for leg length and boxing.

The body of the welding robot is mounted on a lightweight robot carrier designed for transportation, is suspended from a crane, and moves among blocks (**Fig. 6**). The robot carrier has an automatic positioning function and is equipped with the machinery necessary for welding, such as a welding wire feeder. For welding, the robot carrier is lowered to a welding position by an operator and located by the automatic positioner, before

Note 1) AP-SUPPORT is a trademark of Kobe Steel.

the robot operating commands are generated from the 3D-CAD data by the CAD link system and transmitted to the robot to perform welding (**Fig. 7**).

2.3 Application in other fields

The robot welding system for shipbuilding assembly, which comprises a CAD link system that automatically generates optimum welding conditions and robot motions from the 3D-CAD design data, can run multiple robots by itself, greatly contributing to the improvement of productivity at the welding stage. Efforts will continue to further expand the automatic welding technology originating from 3D-CAD to other fields such as steel frames and bridges.

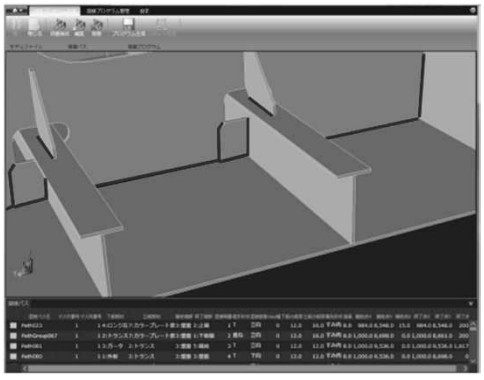

Fig. 5 Automatic detection of welding line from 3D-CAD model

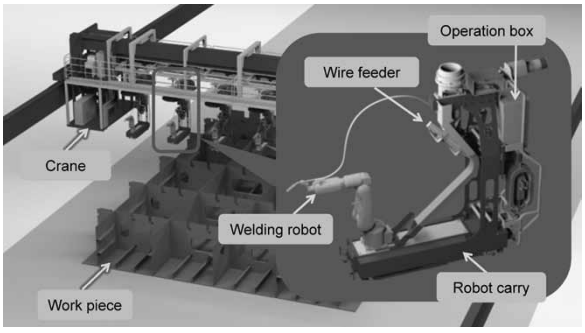

Fig. 6 Assembly welding robot system for shipbuilding

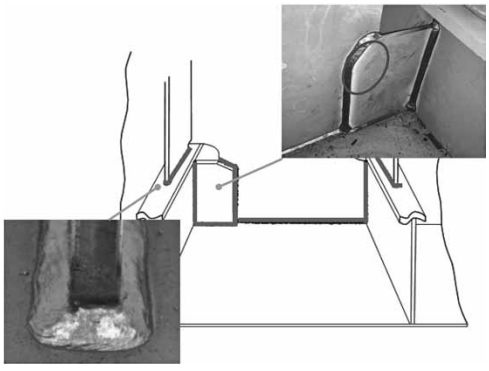

Fig. 7 Welding results of workpieces assembly for shipbuilding

3. Operation management of welding robot system

Realizing stable production by the welding robot system leads to increased production efficiency and facilitated production planning. In the welding of thick steel plates, a significant assembly error may occur due to the large size of the welding objects. Also, there are many factors that inhibit stable operation, such as a temporary stop (a pause due to a mild anomaly) and welding failures, since the welding goes on for a long period of time. When a problem occurs, the accurate understanding of the situations and abundant experience/knowledge are necessary for investigating the cause, and if they are lacking, it takes much time to solve the problem.

Kobe Steel provides software, AP-SUPPORT™, to support stable production. In the company's latest effort, network cameras are installed, and trials are carried out to investigate causes that could not be fully understood from the data alone.

This section describes the outline of AP-SUPPORT™, examples of its application, and the production-monitoring camera system using the network cameras.

3.1 Outline of AP-SUPPORT™

AP-SUPPORT™ is software that runs on personal computers connected with the robot controller via the Ethernet (**Fig. 8**). A large amount of data such as production information and welding information is collected, and the graphs of output and welding data for the production reports are displayed (**Fig. 9**). This has enabled supporting analysis of troubles such as temporary stops and welding failure, as well as the management of production indices such as production volume, takt time, and arc rate, leading to the efficient implementation of production improvement.[6)-9)]

The main data collected by AP-SUPPORT™ is shown in **Table 1**.

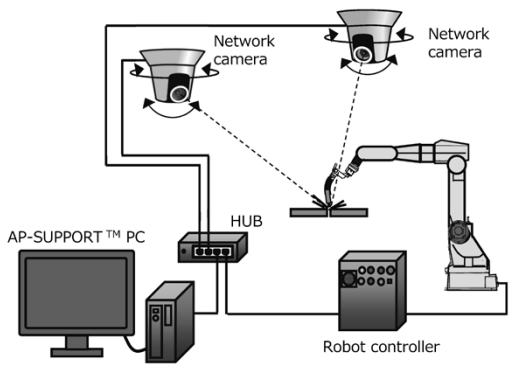

Fig. 8 System configuration

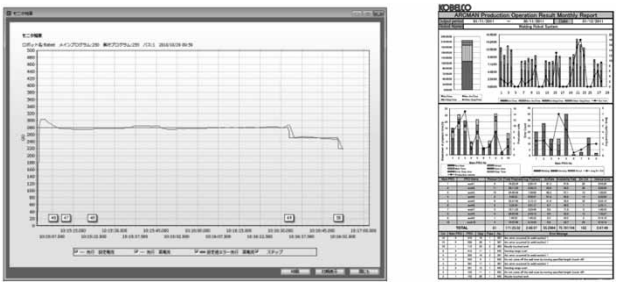

Fig. 9 Function overview of AP-SUPPORT™

Table 1 Production data collected by AP-SUPPORT™

Production information	Welding information
Work data(Program/ Step/Pass)	Welding current
Production start time/ end time	Arc voltage
Welding start time/ end time	Welding speed
Sensing start time/ end time	Weaving width
Sensing retry start time/ end time	Wire feed rate
Welding retry start time/ end time	Wire feed torque
Error stop start time/ end time	Arc tracking adjustment
Wait timer start time/ end time	
Port in out signal ON time / OFF time	
Deviation of the sensing position	
Error type	
Robot position when error occored	
Log of teaching pendant	

3.2 Example of production improvement

Analyzing the data collected by AP-SUPPORT™ allows the determination of the cause of temporary stops and addressing it. **Table 2** shows the results of ranking the locations where touch sensor errors occur frequently and the results of examining the method for dealing with problems based on the situations where errors occur. The cycling of data collection, analysis and correction have yielded an operating ratio improved by 10% or higher in many cases.

It is also possible to check the trend of the amount of sensing correction in order to determine the difference between the actual workpiece and the previously taught program. This can be used for the management of workpiece assembly accuracy (Table 2, **Table 3**). For example, a great variation in the amount of sensing correction indicates poor assembling accuracy in the previous process step. Moreover, when the correction amount is stable and small, the sensing operation itself can be reduced to shorten the takt time.

3.3 Production monitoring camera system

The production monitoring camera system connects a camera mounted on each welding robot system to the robot controller via a personal computer to constantly take photographs of the robot at work (Fig. 8). The positional information is acquired from the robot controller, and this information is used to control the camera direction, advantageously ensuring that the image captures the position of the robot tip (**Fig.10**).

Table 2 Results of analyzing touch sensing deviation

Ranking	1	2	3	4	5	6	7	8	9	10
Program	88	77	89	80	77	85	78	80	90	88
Step	13	6	8	7	11	10	8	5	8	10
Type of sensing	Start	3-D	3-D	3-D	Start	3-D	3-D	3-D	3-D	3-D
Ave deviation[mm]	7.74	7.12	6.81	5.49	5.28	5.1	4.31	4.15	4.04	4.02
Max deviation[mm]	22.16	11.72	27.06	11.28	10.31	12.1	8.67	9.82	21.56	22.44
Min deviation[mm]	5.11	1.01	1.66	1.05	1.12	0.77	1.48	0.15	0.78	0.14
Standard deviation[mm]	1.77	2.06	3.64	1.81	2.13	2.31	1.44	1.96	2.86	3.13

Table 3 Examples of analysis report of robot errors

Error information		Error Messege	Error occurance situation	Improving point (how to avoid the error)
Eror No.	365	Nozzle touched the work.	(Situation)In the switch back welding program、error occurred after changing the tandem welding to single welding. Nozzle of R torch touched the work. (Caused for)Accuracy error between real work and teaching data at the swich back point.	・Correcting the teaching point
Program No.	100			
Step No.	25			
Weld Pass No.	1			
Occurred in	Welding			
Frequency	21%			
Error No.	367	Arc error occurred (in weld section)	(Situation)Error occurred right before the L torch's arc off point. When robot was executing the timer wait operation, L torch touched the work. (Caused for)Accuracy error between real work and teaching data.	・Correcting the teaching point ・Insert "Nozzle touch avoid function"command to the program.
Program No.	101			
Step No.	15			
Weld Pass No.	2			
Occurred in	Welding			
Frequency	15%			
Eror No.	445	Sensing range over (touch off)	(Situaion)3 seconds after tandem welding(both RL) starts, L torch touched to work. (Caused for) Accuracy error between real work and teaching data.	・Correcting the teaching point ・Insert "Nozzle touch avoid function"command to the program.
Program No.	111			
Step No.	23			
Weld Pass No.	1			
Occurred in	Sensing			
Frequency	10%			
Error No.	367	Arc error occurred (in weld section)	(Situaion)2-3 seconds after tandem welding(both RL) starts. L-torch 2times, R-torch 4 times. (Caused for)contact tip erro from burn-back.wire feed error cause from contact tip	・Check and change the weld start point ・Check the wire feed root (torch cable, conduit cable)
Program No.	105			
Step No.	11			
Weld Pass No.	4			
Occurred in	Welding			
Frequency	8%			

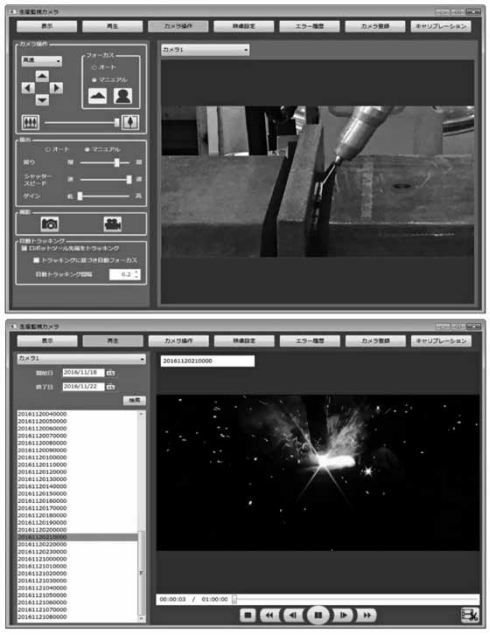

Fig.10 Image captured by production monitoring camera

The camera system also has a function to display currently captured images and to retrieve and display images taken in the past. Furthermore, the cameras are controlled from the PC, making it possible to change the camera direction, zooming, and focusing.

The introduction of this camera system has enabled the recording, together with the imaging, of temporary stops, which hitherto have been known only as sensing errors, and determining the cause of temporary stops in more detail, such as workpiece error, slag and other insulation objects, bent wire, etc. The system can also capture the changes in the amounts of spatter and fume and is expected to be utilized for, among other tasks, the evaluating the stability of welding.

Conclusions

This paper has introduced the function of a welding robot system utilizing ICT. In Japan, the number of welders is envisaged as decreasing with the aging of society and declining birth rates, and the need for improving the productivity of welding robot systems is expected to become even stronger. We will continue to focus on development in the field of welding automation and quality improvement so as to contribute to the improvement of our customers' productivity.

References

1) Welding Technology Editorial Office. *Welding technology, January 2018*. Sanpo Publications Inc, pp.42-45.
2) K. Sadahiro et al. *R&D Kobe Steel Engineering Reports*. 2018, Vol.67, No.1, pp.61-65.
3) Sumitomo Mitsui Banking Corporation. Prospects for shipbuilding market conditions and direction of strategies of Japanese shipbuilding and marine equipment manufacturers. 2017, p.8, http://www.smbc.co.jp/hojin/report/investigationlecture/resources/pdf/3_00_CRSDReport023.pdf, (referred on 2018-03.23).
4) Ministry of Land, Infrastructure, Transport and Tourism, Japan. i-Shipping & j-Ocean. p.3, http://www.mlit.go.jp/common/001173453.pdf, (referred on 2018-03.23).
5) Ministry of Land, Infrastructure, Transport and Tourism. Overview of i-Shipping. http://www.mlit.go.jp/common/001150897.pdf, (referred on 2018-03.23).
6) M. Nagata et al. *Welding Technology*. 2010, Vol.58, No. 12, pp.56-61.
7) A. Fukunaga. *Welding Technology*, 2011-3, Vol.51, pp.1-6.
8) A. Fukunaga. Boudayori Technical Guide, 2012-8, Vol.470, pp.4-5.
9) M. Nagata et al. Welding Guidebook 7. Japan Welding Society. Welding method workshop.2012, p.223.

Development of Image Sensing Technology for Automatic Welding (Image Recognition by Deep Learning)

Tsuyoshi ASHIDA*1, Akira OKAMOTO*2, Keita OZAKI*2, Masatoshi HIDA*2, Dr. Takayoshi YAMASHITA*3

*1 AI Promotion Project Department, Technical Development Group
*2 Production Systems Research Laboratory, Technical Development Group
*3 Department of Computer Science, College of Engineering, Chubu University

A system has been developed for automatic MAG welding with ceramic backing. This system comprises a camera to capture the images of the molten pool for recognizing feature points to control the torch. A regression-based deep convolutional neural network (DCNN), which outputs continuous values from image inputs, was used to recognize feature points such as arc center and the leading end of the molten pool. This has enabled the accurate recognition of the distance from the arc center to the leading end of the molten pool, as well as the width of the molten pool, with an average error of 0.44 mm or less. The formation of a proper back bead has been confirmed in a welding experiment on a test piece with a tapered gap (from 3 to 10 mm).

Introduction

In the field of production, automatic welding technology using robots has become indispensable in recent years to improve productivity to strengthen cost competitiveness and to compensate for the shortage of welders due to the aging of skilled welding technicians. However, there are many welding tasks that are difficult to automate due to the restrictions of apparatus and skills; these tasks still rely on skilled welding technicians. MAG penetration welding with ceramic backing material is one such task.

MAG welding is a type of gas shield arc-welding method and involves high electric current density to allow a large electric current to pass through thin wires. This makes it possible to deeply melt the welded portion to increase the strength. The ceramic backing material, if used, shields the back side and holds the weld bead, which results in the formation of a proper back bead to stably ensure high strength of the welded portion. To form a proper back bead is referred to as "To form a penetration bead." This requires controlling welding while watching the status of the molten pool and the arc, which can only be dealt with by skilled welding technicians and has not hitherto been automated.

Recently, in the field of general image recognition, a technique called "deep learning" has enabled the recognition of humans and objects, as well as the estimation of their positions, with high accuracy. This deep learning technology was applied to MAG penetration welding with ceramic backing material for automation, as described in this paper.

1. MAG penetration welding with ceramic backing material

This paper focuses on butt welding with a V groove that has a gap varying from 3 to 10 mm, to which a ceramic backing plate is attached (**Fig. 1**). During the welding of the first layer, the state of the molten pool changes, depending on—among other factors—fluctuations in the gap width and in the groove angle, and the mounting condition of the backing material. Hence, the existing robots of playback systems encounter arc interruptions and/or joint penetration failures, and they often are unable to yield proper back beads. In order to form a sound back bead, it is necessary to properly maintain the formation of the molten pool and the state of the arc. To this end, parameters such as the electric current, voltage, wire feed rate, and torch/electrode manipulation must be sensed and controlled in real time. In this development, the following control policy has been laid down for stable welding:

(1) The torch speed is controlled so as to keep the arc near the leading end of the molten pool.
(2) Left-right control is performed to hold the torch in the center of the gap width to prevent the weld line from deviating.
(3) When the gap width exceeds a certain value, weaving is initiated in accordance with the gap width.

In order to realize the above control, the coordinates of the leading end of the molten pool, arc center, etc., (feature points) were extracted from

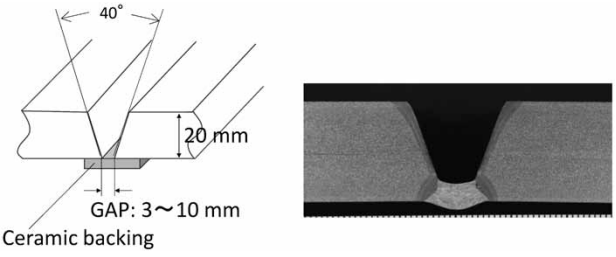

Fig. 1 MAG penetration welding with ceramic backing material

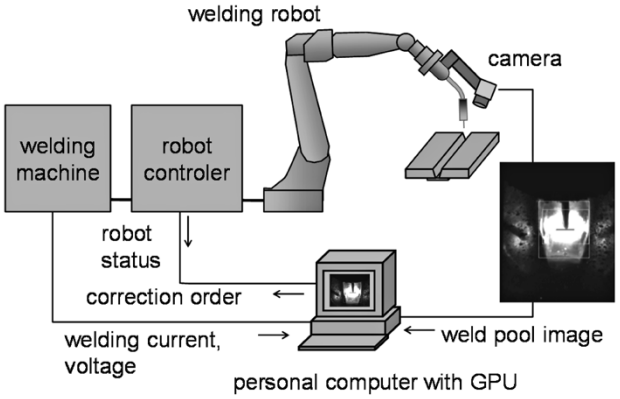

Fig. 2 System Configuration

the camera images capturing the state of welding.

2. Overall system configuration

The overall configuration of the system is shown in **Fig. 2**. The camera is disposed so as to capture the arc and molten pool from a position diagonally forward of the torch. The images are imported into a PC at the rate of 50 fps, and the feature points of the image are calculated every 20 ms. The image feature quantity, however, varies randomly for each image; hence, the past 20 images are averaged to calculate the average feature quantity of the images to determine the amount of control correction (for the speed command, torch left-right command, and weaving width command). The amount of control correction is sent to the robot controller every 200 ms for the welding motion of the robot. Since the calculation of the image feature quantity is based on the average image feature quantity of the last 20 images captured every 20 ms, the amount of control correction for every 200 ms comes to a moving average value of 400 ms.

3. Feature point detection of molten pool based on deep learning

The conventional approach to extracting the leading end of the molten pool, and other features, by image processing generally involved human engagement in combining image feature quantities such as edge and labeling to construct the extraction logic. The shapes and appearances, however, change with alterations in the gap width and welding conditions, even for joints having an identical shape; and each time, human engagement has been necessary to make additional modifications to the image processing logic. Hence a decision has been made to use the regression-based Deep Convolutional Neural Network (hereinafter referred to as "DCNN") in extracting feature points such as the positions of the leading end of the molten pool and of the arc center.[1), 2)] The DCNN has been used for the estimation of coordinates for, e.g., facial organ detection and human posture estimation and has achieved high recognition accuracy.

3.1 Regression-based DCNN

The process flow is shown in **Fig. 3**. The network consists of a grayscale-image entry, four each of convolution layers, batch normalization layers and pooling layers, followed by three fully-connected layers. As shown in **Fig. 4**, the final fully-connected layer outputs values with a total of 10 points, including the coordinate values of the arc center, wire tip, left & right end points of the molten pool (indicated as "edge of pool lead (X,Y)" in the figure), and left & right ends of the molten pool (indicated as "edge of pool (X)", etc., in the figure). In the convolution layer, convolution calculation is carried out with the weight for a filter size of N × N to generate the convoluted value, u. The size of

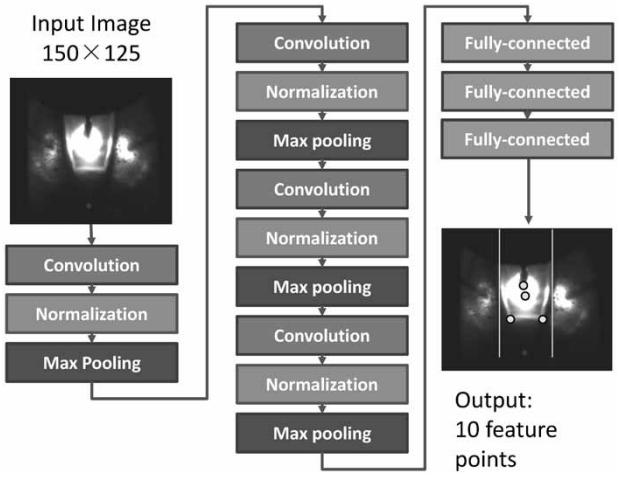

Fig. 3 Regression-based Deep Convolutional Neural Network

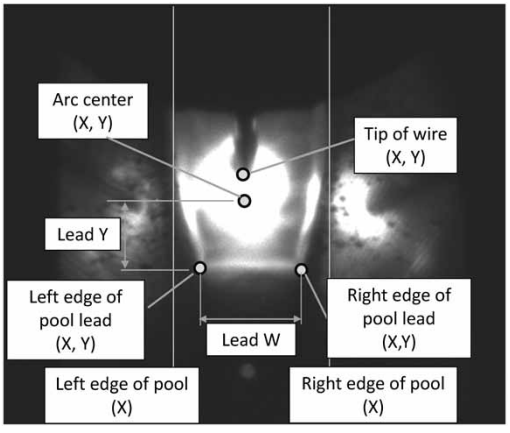

Fig. 4 Feature points of molten pool

the filter used this time is 3 × 3. Next, an activation function is applied to the value, u.

A sigmoid function, hyperbolic tangent function, or a rectified linear unit (ReLU) is generally used for the activation function. The present system employs the ReLU for the activation function. The ReLU is a function that returns 0 when the input value of u is negative and returns the value of u as-is when it is positive. In the convolution layer and the batch normalization layer which follows the activation function, normalization is performed so that each element of the feature map of a mini batch unit, entered upon learning, has an average of 0 and distribution of 1.[3] This reduces the influence of the spots with high brightness values, in particular the arc light, so that the output values can be obtained taking into account the molten pool and welding target plates with relatively low brightness values. In the pooling layer, processing is performed to shrink the feature map that has passed through the batch normalization layer. The pooling techniques include an average value pooling and a maximum value pooling. The present development adopts the maximum value pooling of 2 × 2 size, which is commonly used for general object recognition. In the fully-connected layer, the input feature map is transformed to one dimension to generate the input value to the next fully-connected layer. In the fully-connected layers, a technique for suppressing overlearning, called dropout,[4] is adopted, in which the probability of dropout is set to $p = 0.5$. The ten output values of this fully-connected layer correspond to the ten feature points to be forecasted.

3.2 Learning data and data expansion

Learning data was inputted for the molten pool image of welding, taken in advance, while focusing on the coordinate values, visually determined, of the arc center, wire tip, left & right end points of the molten pool, and left & right ends of the molten pool (these coordinate values are hereinafter referred to as "feature points"). These learning data were inputted from 2,400 images of welding performed 12 times under various conditions.

In deep learning, high forecasting accuracy can be obtained for learning data; however, the forecast accuracy may decline for non-learning test data. One of the factors that cause this decline in accuracy is the difference in appearance between learning data and test data. For example, there may be a case where the misalignment of the camera or the setting position of the recognition target causes a difference between the learning data and test data in the position of the recognition target in an image. There may be another case where the difference in the distance between the camera and the recognition target causes a difference in the size of the recognition target in an image.

In order to suppress the decline of forecast accuracy due to this factor, there is a method of collecting a sufficient amount of data with different appearance and adding it to the learning data. However, this requires a number of experiments and human designation of the positions of feature points for all the images captured. Hence, data expansion was performed to increase the accuracy of recognition based on limited learning data.[5] The data expansion is a technique of providing learning data with the image changes, such as parallel shift, horizontal/vertical inversion, and scaling, and adding the changes to the learning data. This time, the data expansion was carried out by randomly adding a mirror surface inversion to the horizontal direction, parallel shifts by 5, 10, 15, 20 pixels in 8 directions of every 45° angle, and scaling from 0.8 to 1.2 times in each longitudinal/lateral direction at an increment of 0.1. On the basis of the above, learning was carried out on 12,000 data, including the original 2,400 learning data and 9,600 expanded data.

4. Evaluation experiment

In order to verify the validity of the present system, the errors in the values forecasted by the regression-based DCNN were evaluated while carrying out welding experiments.

4.1 Error evaluation of forecast values

In order to evaluate the errors of the values forecasted by the regression-based DCNN, a comparison was made with feature points extracted by the conventional image processing technique. As shown in **Fig. 5**, on the basis of the conventional image processing technique, the left & right lower edges, which constitute the contour of the molten pool, were detected and fitted into curves to identify their intersections with the leading edge, the intersections referred to as the left & right end points (indicated as "edge of pool lead") of the molten pool.

For test data, apart from learning data, the distance, Lead Y, from the arc center to the leading end of the molten pool, and the distance, Lead W, between the left & right ends of the molten pool (**Fig. 6**) were calculated to compare the techniques. These, Lead Y and Lead W, are important values used to control welding.

Fig. 7 compares the average errors, with respect to the coordinates visually selected from the images

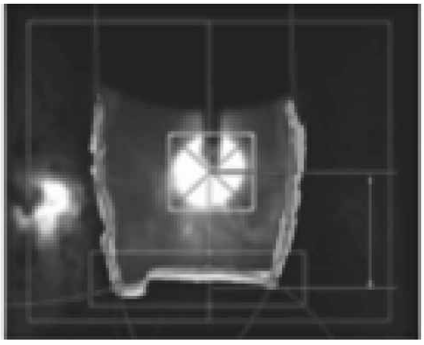

Fig. 5 Edge detection by curve fitting

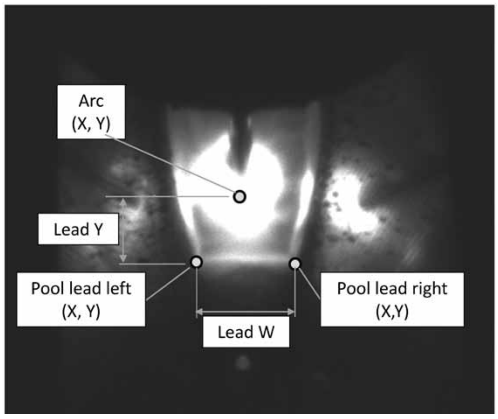

Fig. 6 Feature points Lead Y and Lead W

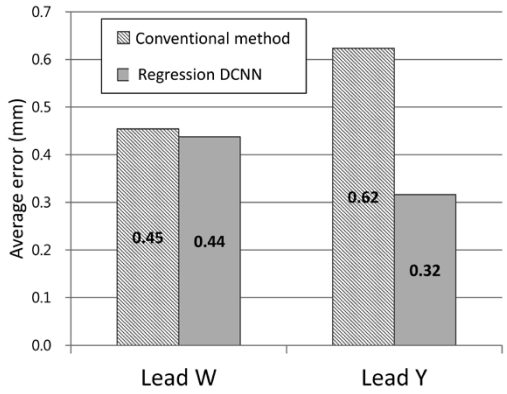

Fig. 7 Average error in coordinates of feature points

of the molten pool, between the coordinates of the feature points extracted by regression-based DCNN, as well as with those extracted by conventional image processing. For Lead W, the same level of errors was confirmed between the conventional image processing and regression-based DCNN, while, for Lead Y, an improvement of 0.3 mm was confirmed in comparison with the conventional image processing. This improvement is attributable to the fact that the conventional image processing erroneously recognizes spatter as the leading end of the molten pool, while regression-based DCNN was able to accurately recognize the leading end of the molten pool.

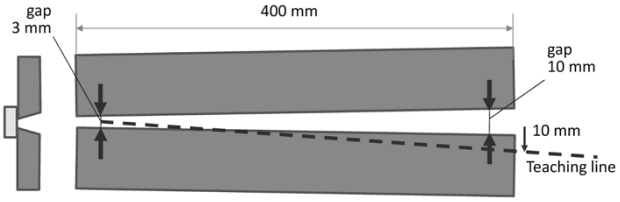

Fig. 8 Test piece

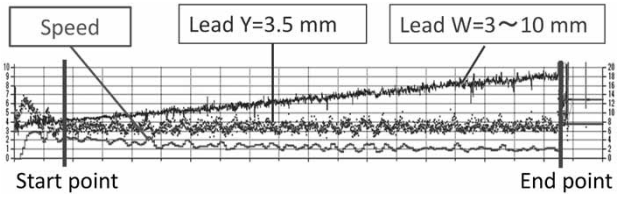

Fig. 9 Changes of control parameters

Movie

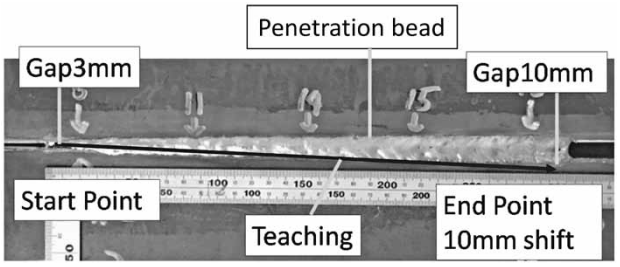

Fig.10 Experimental result (appearance of back bead)

4.2 Welding experiment

To verify the validity of the present system, a welding experiment was conducted, in which a test piece with a tapered gap having a varying groove width (3→10 mm) was disposed at an offset of 10 mm to the right with respect to the final teaching point of welding. The welding was carried out using flux-cored wire (FCW) under the conditions of electric current 200 A, voltage 25 V, and CO_2 gas. The shape of the test piece is shown in **Fig. 8**, and the system configuration is shown in Fig. 2. The images of the state of welding were captured by the camera attached to the torch tip, while the feature points were extracted by PC processing to calculate Lead W and Lead Y, and these values were used as the basis for determining the control variables such as welding speed. **Fig. 9** shows the change in the welding speed, Lead W, and Lead Y from welding start to finish, and **Fig.10** shows the back bead. As shown in Fig. 8, the distance, Lead Y, from the arc center to the leading end of the molten pool is kept at a constant value. The distance, Lead W, between the left & right end points of the molten pool has the same value as the gap width of the workpiece, showing that this gradually increasing width is recognized successfully. As the gap width increases, the pooling of molten metal slows down and the welding speed must be slowed down accordingly.

It is shown also that the welding speed is gradually slowed down to keep Lead Y constant. Fig.10 verifies that a proper back bead is formed regardless of whether there is a misalignment to the right or left, or a gap fluctuation.

Conclusions

An elemental technology for automation was developed for "MAG penetration welding with ceramic backing material." Automatic welding was conducted to control the torch on the basis of the state recognition achieved by deep learning of the molten pool images captured by a camera. As a result, it has been confirmed that a proper back bead can be formed, although still in a limited environment. In the future, we will expand the target joints for deep learning and improve the versatility of molten pool recognition.

References

1) T. Ashida et al. *Preprints of the National Meeting of JWS*, Vol.101. 2017, pp.450-451.
2) T. Yamashita et al. "Facial Point Detection Using Convolutional Neural Network Transferred from a Heterogeneous Task," *International Conference on Image Processing*. 2015.
3) S. Ioeff et al. "Batch normalization: Accelerating deep network training by reducing internal covariate shift," *ICML*.
4) T. Okatani. Deep learning. KODANSHA LTD. 2015, p.30.
5) T. Okatani. Deep learning. KODANSHA LTD. 2015, p.35.